Studies of Microstructural Properties of Iron Doped Glass Nanocomposite System

Thesis submitted by

Ajit Mondal

Doctor of Philosophy (Engineering)

Department of Mechanical Engineering
Faculty Council of Engineering & Technology
Jadavpur University
Kolkata, India

2025

Index No. 89/19/E

1. **Title of the Thesis:** Studies of Microstructural Properties of Iron Doped Glass Nanocomposite System.

2. **Name, Designation, and Institution of the Supervisors:**

Prof. (Dr.) Debasish Roy
Mechanical Engineering Department
Jadavpur University

Dr. Amit Mallik
Assistant Professor
Department of Chemistry
Acharya Jagadish Chandra Bose College

3. **List of Publications:**

Journals:

(a) A. Mondal, P. Biswas, M. K. Mondal, S. Karmakar, D. Roy, S. Bhattacharya and A. Mallik, Influence of Fe on crystallization behaviour and electrical conductivity of V_2O_5 MoO_3·CdO·ZnO glass nanocomposite, Chemistry Select, 8 (2023) e202205010 (1-9). https://doi.org/10.1002/slct.202205010.

(b) A. Mondal, A. Dey, S. Bhattacharya, D. Roy, A. Mallik, Investigation of the relationship between morphology-electrical transport phenomena in iron-doped quaternary glass nanocomposite, Next Materials, 4 (2024) 100201(1-12). https://doi.org/10.1016/j.nxmate.2024.100201.

(c) A. Mondal, A. Dey, P. Halder, A. Chamuah, S. Bhattacharya, D. Roy, A. Mallik, Relaxation process of Fe-doped V_2O_5·MoO_3·CdO·ZnO glassy nanocomposites, Sci. and Cult. 90 (7–8): 280-282 (2024), DOI: https://doi.org/10.36094/sc.v89.2024.

Book Chapter:

(a) A. Mondal, D. Roy, A. K Bar, and S. Bhattacharya, Mechanical Properties of Some Li-Doped Glassy Systems, Lithium Ion Glassy Electrolytes, Properties, Fundamentals, and Applications, ISBN 978-981-19-3269-4 (eBook), pp. 103-118, First Online: 02 October 2022, https://doi.org/10.1007/978-981-19-3269-4.

4. **List of Patents:** None

5. **List of Presentations in National/Internation/Conferences/Workshops:**

(a) A. Mondal, A. Sengupta, A. Mallik, D. Roy, G. K. Panda and S. Bhattacharya, Investigation of ac and dc connectivity conductivity of Fe-V_2O_5-CdO-ZnO glass nanocomposites, International Conference on Advanced Materials, Amal Jyothi College of Engineering, Kerala, December, 2021.

(b) A. Mondal, A. Dey, P. Halder, A. Chamuah, S. Bhattacharya, D. Roy, A. Mallik, Relaxation process of Fe-doped V_2O_5·MoO_3·CdO·ZnO glassy nanocomposites, International Conference on Natural Sciences and Engineering for Sustainable Development, Kazi Nazrul University, Asansol, West Bengal, March, 2024.

Statement of Originality

I **Ajit Mondal** registered on **31st May 2019** do hereby declare that this thesis entitled **"Studies of Microstructural Properties of Iron Doped Glass Nanocomposite System"** contains literature survey and original research work done by the undersigned candidate as part of Doctoral studies.

All information in this thesis have been obtained and presented in accordance with existing academic rules and ethical conduct. I declare that, as required by these rules and conduct, I have fully cited and referred all materials and results that are not original to this work.

I also declare that I have checked this thesis as per the "Policy on Anti Plagiarism, Jadavpur University, 2019", and the level of similarity as checked by iThenticate software is 2%.

Ajit Mondal

Ajit Mondal
Registration No. 1021911005
Date of Registration: 31/05/2019

Debasish Roy

PROFESSOR
MECHANICAL ENGINEERING DEPTT.
JADAVPUR UNIVERSITY
KOLKATA-700 032

……

Prof. (Dr.) Debasish Roy
Department of Mechanical Engineering
Jadavpur University

Dr. Amit Mallik
Assistant Professor
Department of Chemistry
Acharya Jagadish Chandra Bose College
1/1B, A.J.C Bose Road
Kolkata-700020

.....

Dr. Amit Mallik
Assistant Professor
Department of Chemistry
Acharya Jagadish Chandra Bose College

Certificate from the supervisor

This is to certify that the thesis entitled **"Studies of Microstructural Properties of Iron Doped Glass Nanocomposite System"** submitted by Shri Ajit Mondal, who got his name registered on **31st May 2019** for the award of Ph. D. (Engineering) degree of Jadavpur University is absolutely based upon his own work under the supervision of Prof. (Dr.) Debasish Roy, Mechanical Engineering Department, Jadavpur University and Dr. Amit Mallik, Assistant Professor, Department of Chemistry, Acharya Jagadish Chandra Bose College, and that neither his thesis nor any part of the thesis has been submitted for any degree /diploma or any other academic award anywhere before.

PROFESSOR
MECHANICAL ENGINEERING DEPTT.
JADAVPUR UNIVERSITY
KOLKATA-700 032

……

Prof. (Dr.) Debasish Roy
Department of Mechanical Engineering
Jadavpur University

Dr. Amit Mallik
Assistant Professor
Department of Chemistry
Acharya Jagadish Chandra Bose College
1/1B, A.J.C Bose Road
Kolkata-700020

.....

Dr. Amit Mallik
Assistant Professor
Department of Chemistry
Acharya Jagadish Chandra Bose College

Acknowledgement

I wish to express my profound sense of gratitude to my supervisors, **Prof. (Dr.) Debasish Roy**, Mechanical Engineering Department, Jadavpur University, and **Dr. Amit Mallik,** Assistant Professor, Department of Chemistry, Acharya Jagadish Chandra Bose College, India, for their encouraging guidance and supervision, valuable suggestions and critical comments without which the present research work could not have been carried out.

I am extremely thankful to **Dr. Sanjib Bhattacharya**, Composite Materials Research Laboratory, UGC-HRDC (Physics), University of North Bengal, District: Darjeeling-734013, West Bengal, India, for his encouraging words and support during my research work.

I would like to thank my Research Advisory Committee (RAC) Members, **Prof. (Dr.) Arunabha Chanda**, Department of Mechanical Engineering, Jadavpur University, and **Prof. (Dr.) Sandip Sarkar**, Department of Mechanical Engineering, Jadavpur University for their constant support.

I am particularly thankful to **Dr. Prosanta Biswas,** Research Associate, Department of Materials Science & Engineering, Indian Institute of Technology Delhi, Hauz Khas, New Delhi -110016, India for his continuous support.

I am particularly thankful to **Mr. Rahul Bhandari**, Research Scholar of Metallurgical and Materials Engineering Department, National Institute of Technology, Durgapur for his continuous support.

I express my gratitude to **Prof. (Dr.) Suresh Neelakantan**, Department of Materials Science and Engineering, IIT Delhi, India for extending the facility of SEM and FESEM-EDX analysis.

I am very much thankful to my wife, **Mrs. Arpita Dey**, Asst. Professor, Department of Mechanical Engineering, Ideal Institute of Engineering, Kalyani- 741235, West Bengal, India for her help as well as physical and mental support.

Lastly, I would like to thank all my family members and well-wishers, especially my parents, Mrs. Biswarupa Mondal and Mr. Narayan Chandra Mondal, my brother Mr. Sujit Kumar Mondal, my sister Mrs. Anju Majumder (Mondal), my niece Miss Snigdha

(Tuntuni) Mondal and Miss Asmita Majumder, and my sister-in-law Mrs. Rumki Mondal. Without their love, support, understanding, encouragement, and sacrifice, I would not be able to successfully reach the end of this journey.

Finally, I express gratitude to God, the Almighty, for His showers of blessings throughout my research work to complete the research successfully.

.....

Date: 10.03.2025 (**AJIT MONDAL)**

Place: Jadavpur University, Kolkata (Registration No. 1021911005)

CONTENTS

List of Figures

Page No.

List of Tables

Page No.

List of Abbreviation and Symbols

MMC	Metal Matrix Composite
SPH	Small polaron hopping
GPa	Giga Pascal
MPa	Mega Pascal
N	Newton
m	Meter
S	Second
Kg	Kilogram
°K	Degree Kelvin
°C	Degree Celsius
h	hour
DP	Dual Phase
MP	Multi-Phase
HT	Heat treatment
Al	Aluminium
Mg	Magnesium
Si	Silicon
Ti	Titanium
W	Tungsten
Mo	Molybdenum
Cu	Copper
Pb	Lead
Al_2O_3	Aluminium Oxide Or Alumina
SiC	Silicon Carbide
SiO_2	Silicon Oxide
TiO_2	Titanium Oxide
B_4C	Boron Carbide
ZrO_2	Zirconium Oxide
QMT	Quantum-mechanical tunneling model
NSPT	Non-overlapping small polaron tunneling model
OLPT	Overlapping large polaron tunneling model
AH	Atomic hopping model
CBH	Correlated barrier hopping model
HV	Vickers Hardness
CTE	Coefficient of Thermal Expansion
α-Al	Primary Al
Li	Lithium
q_x	Heat Flux in the X-Direction
B	Boron
Sr	Strontium
Y	Yttrium

Bi	Bismuth
P	Phosphorous
Sb	Antimony
Ce	Cerium
B	Boron
Na	Sodium
Ni	Nickel
Mn	Manganese
Zr	Zirconium
Ca	Calcium
Sc	Scandium
V	Vanadium
Nd	Neodymium
G	Shear modulus
E	Elastic modulus
Y	Yield Strength
ρ	Density
E	Young's Modulus
μ	Coefficient of Friction
ICP	Inductively Coupled Plasma
MS	Mass Spectrometry
DSC	Differential Scanning Calorimetry
F_r	Frictional Force
EDS	Energy Dispersive X-Ray Spectroscopy
XRD	X-Ray Diffraction
DOF	Degrees of Freedom
λ	Wavelength
n	Hardening Exponent
σ	Nominal Stress
ε	Strain
TMO	Transition metal oxide
TMI	Transition metal ion
XRD	X-ray diffraction
FT-IR	Fourier transform infrared spectroscopy
DSC	Differential scanning calorimeter
FE-SEM	Field emission-scanning electron microscopy
CV	Cyclic voltammogram
ISE	Indentation size effect
RISE	Reverse indentation size effect

ABSTRACT

The effect of varying iron content on the crystallization behavior, electrical conductivity mechanism, and mechanical properties of glass nanocomposite based on the system $xFe\cdot(1-x)\cdot(0.3V_2O_5\cdot0.2MoO_3\cdot0.4CdO\cdot0.1ZnO)$ (x = 0.0, 0.05, 0.1, 0.2, 0.3, and 0.4) was investigated by differential scanning calorimetry (DSC), Fourier transform infrared (FTIR), X-ray diffraction (XRD), and field emission-scanning electron microscopy (FESEM). Different crystal phases and average sizes of the developed nanocrystallites in the as-prepared samples have been obtained from the XRD diffraction data. FESEM micrographs confirm the formation of plate-like and dendrite nano crystallites throughout the glass matrix. Energy-dispersive X-ray spectroscopy (EDX) mapping analysis shows the weight percentage of each constituent element. The density and molar volume data of as prepared samples show the inverse relation due to the formation of non-bridging oxygens. The DC activation energy (E_σ)as well as activation energy (E_H) for the hopping frequency of as-prepared samples gradually decreased with increasing Fe content whereas AC and DC conductivity gradually increased. AC conductivity scaling data has explored that the common electrical relaxation mechanism is temperature-independent as well as composition-dependent. Vickers Microhardness measurement of all samples has been performed by using an indentation load (0.049 N to 0.980 N) at room temperature as well as different heat treatment conditions. The experimental microhardness results have been analyzed using Meyer's law, the elastic/plastic deformation model, the proportional specimen resistance model, the Hays–Kendall approach, and the indentation-induced cracking (IIC) model.

CHAPTER-1

Introduction

Contents

Chapter-1

1.1 Background

Recently, nanoglass semiconductor materials have intrigued researchers' attention owing to their outstanding electrical, structural, and optical properties [1-4]. A particular interest has been shown in oxide-based glassy systems, coupled with transition metal ions such as V, Fe, Mo, and W, doped on them due to their different oxidation states [5-6].

Many applications of these transition metal oxides (TMO) glass nanocomposites have drawn increased attention, like electro-optical devices, and optical and resistive switching devices [7-11]. In addition, due to its high mechanical properties, transparent glass-ceramics are greatly accepted materials for the protective cover of the new generation mobile phones [12, 13]. Various researchers have taken different compositions of chemical reagents to make glass nanocomposite and their properties. Various transition metal oxide (TMO) doped glass nanocomposites like CuO [14,15], V_2O_5 [7, 16], and Fe_2O_3 [17] are widely studied for the electrical conduction mechanism and also polaron hopping frequency. Parmar et al. [18] observed that the morphology and the physical properties of the glassy system consist of bismuth-silicate with the effects of Fe_2O_3. The effects of Fe_2O_3 make a substantial decline in density and molar volume. Differential thermal calorimetric (DCS) analysis revealed that the glass transitions in an extensive domain of the glass formation zone decrease with an increase in Fe_2O_3. Aquino-Meneses et al. [19] observed that by introducing varying concentrations of CdO and V_2O_5 in the $CdO{\cdot}V_2O_5$ binary system, the conversion of crystalline to amorphous phase can be detected. XRD analysis results confirm the presence of the different kinds of crystal phases [19]. Desoky [20] studied the physico-mechanical behavior of the V_2O_5–BaO–B_2O_3 glass system and they observed that this glass system is amorphous. Ghosh and Chaudhuri [21] reported that the heat-treated V_2O_5-Bi_2O_3 glass samples showed an amorphous nature up to 200^{o}C. At 255^{o}C heat treatment conditions, a crystalline phase was formed and changed the conductivity. Different nanoparticles (ZnO, $Ag_2Mo_2O_7$, Ag_2MoO_4, and $Ag_6Mo_{10}O_{33}$) dispersed in $ZnO{\cdot}AgNO_3{\cdot}MoO_3$glass nanocomposites system [22]. The Mo–O octahedral units were symmetric stretching, which is confirmed by FTIR spectra. The bond strength of Mo-O became feebler due to the enhancement of ZnO content in the composition [22]. The structure of the nano glass series of $V_2O_5{\cdot}SrO{\cdot}B_2O_3$ elaborated through FTIR spectroscopy [23]. Laila et al. [24] studied the density of a$V_2O_5{\cdot}PbO{\cdot}ZnO$glassy system and its structural compactness. Density can be improved in some ways like increasing in total molecular mass and decreasing

the molar volume. It has been also observed that the molecular mass gets decreased when V_2O_5 is interchanged by ZnO, this in turn decreases the density of the glassy system [24]. Researchers [25] studied the bismuth borate glassy system by adding Fe_2O_3 to it. They found that the thermal stability is enhanced but the density and molar volume is reduced. Due to the network-modifying behavior of V_2O_5, all glass sample densities were reduced in a linear manner with rising V_2O_5 content. With the inclusion of, V_2O_5 molar volume of the samples also increased in the system, introduced by Sindhu et al. [23].

Different researchers have explored the electrical conductivity (both AC and DC) of glassy nanocomposites due to their semiconducting behavior as well as technological uses in modern civilization [26-30]. AC conductivity measurement has been widely used in [31–35] semiconducting nano-glassy composite systems to know the mechanism of conduction (electrical). The existence of defect states is also known in their study. The charge transfer mechanism of TMO doped glass is a vital part of the temperature dependence of conductivity. [2, 36]. The iron phosphate glasses show the semiconductor nature of electronic conductivity due to the two different oxidation states of iron [37-38]. Polaron hopping between Fe^{2+} and Fe^{3+} is primarily accountable for the conductivity in iron-containing glass nanocomposite and also conductivity depends on the iron oxide content [39]. The transition metal ions, vanadium, and molybdenum have more than one oxidation state respectively V^{4+}, V^{5+} and Mo^{+6}, Mo^{+7} in vanadate and molybdate glassy system, the electron conduction arises through small-polaron hopping (SPH) which is thermally activated between lower to higher oxidation state at higher temperature [3, 40-41]. Desoky [20] reported the effect of DC electrical conduction on high temperature in the glassy system in terms of SPH theory by Mott's model. Activation energies for DC conductivity are also calculated. Ghosh and Chaudhuri [21] explained the direct current conductivity of V_2O_5-Bi_2O_3 semiconducting glasses taking 80, 90, and 95 mol% V_2O_5 in the ranges of 80-480 K temperatures. The DC electrical conduction glass nanocomposites in the system $V_2O_5 \cdot B_2O_3 \cdot SrO$ had been explained through the theory of SPH by Mott [6]. A wide range of semiconducting nano-glassy composite [31-32] systems have been measured for AC conductivity to understand the mechanism of electrical conduction as well as defects. Several models are introduced to illuminate the mechanism process of AC conduction, including the QMT model [42-43], the NSPT model [43], the OLPT [44], the AH model [43-44], and the CBH model [23, 45].

Besides physical, structural, and electrical properties, the micromechanical hardness of a nano-glassy material has been the subject of scientific investigation in the past several years

by several research communities [46-49]. Microhardness properties of a nano glassy material can be improved through proper characterization of the micro-structure of nanocomposites [47-48]. Several researchers have explained the microhardness of nanocomposites to be a crucial role in determining the indentation size effect of nanocomposites (ISE) [48-50]. Ozturk et al, have shown in their study the H_v increases with ascending applied load. In their system, the yield strength, young's modulus, along with fracture toughness have been enhanced by increasing the microhardness with Ru doping [51]. Paykani et al. have experimented on the micro Vickers indentation effect of heat-treated $(Fe_{0.9}{\cdot}Ni_{0.1})77Mo_5P_9{\cdot}C_{7.5}B_{1.5}$, and $Fe_{40}{\cdot}Co_8{\cdot}Cr_{15}{\cdot}Mo_{13}{\cdot}Y_2{\cdot}C_{16}{\cdot}B_6$ bulk metallic glasses system [52]. Tian et al. reported the crystallization behavior, structural characteristics, and mechanical properties of $CaO{\cdot}Ta_2O_5{\cdot}Al_2O_3$ glass-ceramics [53].

Among several mechanical experiment techniques, indentation hardness tests have supplied more reliable information on the material's mechanical properties for practical applications and also for academic research over standard mechanical testing [48-49, 54-55]. Microhardness studies in nanocomposite materials have seen limited research in the last few years, and are less commonly described in the literature. Nowadays, the mechanical properties of nanocomposites are crucial due to their exceptional chemical and physical attributes, making them highly useful in real-world scenarios [56]. The reverse indentation size effect (RISE) describes how microhardness grows with rising functional load in contrast to the indentation size effect (ISE), which still needs to be studied [48-49].

Several areas of glass nanocomposites have remained unexplored in the last few years and are less commonly described in the literature.

- What is the combined effect of TMO-based glass nanocomposites on the microstructural point of view?
- Several investigations have been made on the structural and conductivity of the glasses containing various kinds of transition metal ions, but few studies are surface out on the effect of iron in the transitional metal oxide-based glassy nanocomposite system.
- How the transition metal ion (Fe) concentration is associated with electrical conductivity (AC as well as DC) and how does it change with the change in temperature along with composition?
- What is the role of Fe concentration on the mechanical properties of transitional metal oxide-based glass systems and how does it vary with heat treatment temperature?

The prime aim of the current investigation is to examine the effect of iron (TMI) in the present glass system of $V_2O_5 \cdot MoO_3 \cdot CdO \cdot ZnO$. In this glass system, cadmium oxide and vanadium oxide played a crucial role as network modifiers and also network formers. In order to make a sample appropriate for a broad domain of applications of this glass system, ZnO is used as a supplementary network forming/network modification material. It has been studied in various compositions and is characterized by various methods like Fourier transform infrared spectroscopy (FT-IR), Differential scanning calorimeter (DSC), X-ray diffraction (XRD), Field emission-scanning electron microscopy (FE-SEM), and Vicker's hardness (H_v) measurement.

1.2 Objectives

Based on the existing literature survey on the present research topic, and after a thorough analysis of the gaps present in this domain of research, the following objectives have been identified as the topics of investigation for the present dissertation:

1. To develop a novel glassy nanocomposite system based on transition metal oxides (V_2O_5, MoO_3, CdO, and ZnO) with Fe ion doping by applying the melt quenching method.
2. To investigate the density and molar volume measurement of the present glass nanocomposite system.
3. To characterize by various techniques i.e. X-ray diffraction (XRD), Fourier transform infrared spectroscopy (FT-IR), Differential scanning calorimeter (DSC), and field emission-scanning electron microscopy (FE-SEM).
4. To investigate electrical properties of prepared glass nanocomposite by examining the AC and DC electrical conduction measured by LCR meter and also calculate various activation energies of the prepared samples to reveal the electrical conduction mechanism.
5. To explore the consequences of iron imposed on microhardness nature of this new glassy system at as-prepared conditions along with different heat treatment durations.
6. The experimental Vickers micro-hardness values are to be enumerated and analysed by utilising several models to describe the usual indentation size effect (ISE) and unusual reverse indentation size effect (RISE) in crystalline solids at as-prepared conditions along with different heat treatment durations.

1.3 Thesis Layout

This thesis incorporates nine chapters and references. Chapter 1 involves a general scenario and inspirations to choose this area to pursue the present work. The objectives and layout of the present thesis are also discussed. Chapter 2 presents an introduction to the glass, glass nanocomposites. This chapter also concentrates on the explanation of various routes for the synthesis of glass and glass-nanocomposite. Different existing literature related to the field of glass-nanocomposites, $V_2O_5 \cdot MoO_3 \cdot CdO \cdot ZnO$ based glass-nanocomposites composites, iron-doped glass nanocomposites with a discussion of the synthesis process, structural analysis, electrical as well as mechanical behavior has been discussed. Chapter 3 focuses on the experimental procedure of the present study in detail, including the raw materials, method of sample preparation, and characterization techniques. Microstructural, physical, electrical, and mechanical properties are discussed in detail in characterization techniques. Results and discussion of the present thesis are presented in Chapter 4. Chapter 4 is divided into three sections such as 4.1 microstructural evaluation, 4.2 electrical properties 4.3, and mechanical properties of $Fe \cdot V_2O_5 \cdot MoO_3 \cdot CdO \cdot ZnO$ Glass Nanocomposite System. Section 4.1 incorporates the effects of density and molar volume on the Fe-doped $V_2O_5 \cdot MoO_3 \cdot CdO \cdot ZnO$ based glassy system. Structural characterization techniques like FTIR, XRD, and FESEM have been discussed in detail. Differential scanning calorimetry (DSC) analysis of the developed $Fe \cdot V_2O_5 \cdot MoO_3 \cdot CdO \cdot ZnO$ glass system is also mentioned in this section. Section 4.2 has elaborated on the electrical conduction mechanism (Both AC and DC conductivity) of the existing system. Almond West formalism and AC conductivity scaling studies have been also reported in section 4.2 for analyzing the AC conductivity. In section 4.3 of chapter 4, the mechanical properties of the present glass system have been discussed. Microhardness analysis of the system at as prepared as well as various heat treatment conditions also discussed in this section. The influences of Fe concentration on mechanical properties like young's modulus, shear modulus, and yield strength are also presented in this section. We have studied the ISE and RISE behavior of the present glass system by applying a variety of theoretical models of microhardness prepared as well as handled under different heat treatment conditions. Chapter 5 furnishes the major conclusions collected from the present investigation. Scope for the future studies of the developed glass nano-composites has been also discussed at the end of this chapter.

CHAPTER-2

Literature Review

Contents

Chapter-2

2.1 Introduction

This chapter illustrates various aspects such as the theoretical background of glass, glass-nanocomposites, and applications of the glass-nanocomposites materials. Different nano-glassy systems with various compositions will be elaborated. The chapter also concentrates on the effect of various chemical reagents (V_2O_5, MoO_3, CdO, and ZnO) on the glassy nanocomposite system. Past research of transition metal ions doped or based glassy systems will be added. Past research based on microstructural analysis, and electrical and mechanical properties of glass-nanocomposite will be discussed. An overview of Fe-based glass nanocomposites related to existing research will also be presented.

2.2 Glass

"GLASS" forms as a vertebra along with many other materials in the path of the advancement of human civilization. It has numerous uses from the mirror proceeding towards window glass and then finding its use in advanced solid electrolytes.

GLASS resembles a cooled liquid and has similar mechanical properties as that of a solid [57-58]. Generally, the glass is prepared through quenching method and this melting is done of its components elements [59-63]. The term glassy refers to amorphous solids that show T_g (glass transition temperature). In the method of melt quenching, the cooling process should be fast enough so that the disordered liquid atoms get frozen, and thus not allowing them to be crystallized at the glass transition temperature. Glass forming ability is defined as the addition of a material to be in glass form on quenching.

Glass also shows low tensile strength, less hardness, etc which restricts its usage. The drawbacks of glass are overcome by the amalgamation process where metal nanoparticles are used in its matrix giving rise to nanocomposite materials [64-65]. The formed nanocomposite materials account for unique properties like electrical, optical, thermal, and mechanical, and find their application in nanotechnology [66-71]. For a specific application, the desired specific properties of the nanocomposites rely on the shape, amount, and the size of the nanoparticles which is incorporated [72-73].

2.3 Glass-Nanocomposites

In a hybrid material, there are usually two or more phases, each of which has a certain proportion. Two types of phases can be distinguished based on their structure: matrix and

reinforcement. The phase covering more extent and is continuous is termed a “Matrix” and that covering a small extent and is discrete or dispersed is termed “Reinforcement”. The components of the phases are segregated by a proper interface. The stresses are transferred to the other phases by the matrix. It also protects the environment. The dispersed phase helps in the enhancement of the matrix properties. In addition to having unique physical and chemical behavior, the phases work together to produce results that differ from the component phases. Further, the composites can be categorized into two types that are type A and type B. Type A is differentiated on the type of matrix, and type B is differentiated by the type of reinforcement geometry [74].

A nanocomposite material has at least one dispersed phase in the range of 1 to 100 nm. By unifying or generating NC (nanocomposite) in situ, companies can transform composite materials into NC ranging in size from 1 to 100 nm. That’s why NC may be divided into PMNC, CMNC, MMNC, PNC, FNC, and LNC. There is no change in the crystalline or amorphous state of the dispersed nanophase. The nanophase interacts heavily at the interface, whereas conventional composites do not exhibit this phenomenon [74].

GNC is the special quality of nanocomposite. GNC is defined as a hybrid one as two or more phases where the material is composed of glass. It resembles PMNC, CMNC, or MMNC. There is a greater reliance on the glass matrix characteristic of GNC in terms of its properties [74]. For the ease of perception of the mechanical, and electrical properties and the microstructural analysis the following aspects need to be identified.

(a) Generally, XRD, FTIR, and FESEM tests are used for microstructural analysis of glass nanocomposites.

(b) Micro-hardness measurement is very important for mechanical properties.

(c) Electrical properties such as electrical conduction mechanism, AC and DC conductivity, etc.

2.4 Different Routes for Synthesis of glass and glass-nanocomposite

Traditional glasses are generally in the inorganic and non-metallic category but in recent days organic glasses play the front role and these types of glasses require various techniques of preparation. Metallic glasses have also played roles in recent days and evolved as days passed. In contrast to the amorphous phase, the crystal form is more stable thermodynamically, which indicates the amorphous phase has more free energy. As such, the production of amorphous materials can be viewed as an addition to the crystalline polymorph

with surplus free energy. Additionally, there are other methods of preparing glass, such as physical vapor deposition, thermal evaporation, sputtering, glow discharges, chemical vapor deposition, sol-gel methods, etc [75-79].

2.4.1 Melt quenching Route

The molten mass is cooled to discontinue the growth of the crystal. Various methods are present for the making of glassy materials utilizing this technique. Five methods out of all are generally used for the preparation of non-crystalline materials on commercial or academic grounds. For the preparation of glassy solids, quenching rates play an important role [75].

Mainly oxide glasses are produced with the help of this process. Most of the materials require rapid quenching so that it converts into glass. For glassy phase formation, the rate of cooling is not the same it varies from material to material. Chemical reagents in a certain ratio are properly mixed, melted and then it is quenched at ambient temperature quickly. To prevent crystallization, the melting rate must be maintained fast enough to avoid crystallization [76].

2.4.2 Gel Desiccation

In this technique, amorphous materials are produced by a sol-gel process. This technique is utilized for those systems that face difficulty in transforming into glass by the melt quenching method [77]. It is also very useful to those systems that produce melts in the form of viscosity that is near the melting point or has a high melting point. The first component used in the formation of amorphous material is aqueous solution or organic materials. In both methods, the volatile components from the multi-component “gel” (being noncrystalline and homogeneous) are eliminated through heating. In this process, fundamental densification takes place, culminating in the formation of an amorphous solid by sintering or fusing.

2.4.3 Thermal Evaporation

For generating thin films, the thermal evaporation method is widely used [78]. Materials in grains or powder form are vaporized in a high vacuum environment. At a lesser temperature, a substrate is kept at an appropriate distance. In this method electron beam is used to heat the evaporating material or it is heated resistively. The motility of the atom attending the surface is congealed because of the lesser temperature of the substrate which leads to the creation of thin film. Thermal evaporation produces thin films of amorphous semiconductors.

With the help of this technique, thin uniform glass layers are formed and the desired thickness of the layers can be achieved. There are some disadvantages of this method is also present and among them, the important one is the individual constituent shows differential evaporation. Components having a lesser melting point or higher vapor pressure evaporate and create compositional homogeneity in the film by evacuating the source. The application of this kind of glass is to make smart windows, display devices, etc [79].

2.4.4 Sputtering

In this process, energetic ions are bombarded from a less-pressure plasma. This results in material erosion. The erosion takes place either atom by atom or by forming a cluster which is subsequently deposited as a film on the glass. This approach is typically regarded as preferable to evaporation for preparing multi-component systems. In various components, the sputtering rates do not vary to a great extent. Thus, the stoichiometry of the initial material of the sputtered films is retained. Other gases than argon can be used in sputtering, causing chemical reactions with the target, and originate in "reactive sputtering". This results in an increased rate of sputtering and selected additives are incorporated into the film [80-81].

2.4.5 Other Techniques

Various methods are available for the preparation of amorphous materials such as "Chemical Route", “Glow-discharge decomposition”, “chemical vapor deposition”, electrolytic deposition, irradiation, shockwave transformation, etc. In "Chemical Route" appropriate precursor chemicals are used and it is heat treatment is performed under various ambient conditions [82]. Huber et al. [82] utilized a pressure injection technique for the production of arrays of nanowires of metals such as ln, Sn, and Al as well as semiconductors such as Se, Te, Ga, Sb, and Bi_2Te_3 in the anodic alumina membranes that is in the channel.“Glow-discharge decomposition” technique just as sputtering depends on the preparation of plasma in an atmosphere of low pressure.

Chemical vapor deposition is a superior technique for making an amorphous system. The substrate is heated by an applied radio frequency field in this method, which relies on thermal energy for the decomposition process. Generally, a temperature of about 1000K is mostly utilized.

2.5 Glass-Nanocomposites: Overview

The appropriate composition of chemical reagent-grade ingredients of a glass nanocomposite is the crucial part, which directly affects its thermal, optical, mechanical, and electrical properties. Various researchers have taken different compositions of chemical reagents to make glass nanocomposite and their properties.

Ojha et al [83] studied the electrical (AC and DC conductivity) properties of Cu·S·Te glass nanocomposite system. Where Cu content varied from 0 to 0.3 in the composition of the ternary system. DC conductivity analysis was illustrated in both low temperature and high temperature applying Mott's, and Greaves's models respectively. Frequency, as well as temperature-dependent AC conductivity data, were also explained through CBH and NSPT models.

Hassanien and Akl [84] prepared the Cd·S·Se based non-crystalline bulk glasses through mechanical milling technique, where Se content was varied. On increasing the Se content, properties like volumetric mass density, molar mass, molar volume, field strength, excess volume, field strength, atomic density, and compactness values were also increased.

Bo et al. [85] investigated the low softening point-based Li_2O-Al_2O_3-SiO_2 glass-ceramic system, that could be sintered below 900^0C. Results showed that the incorporation of CaO enhances the densification, microstructure, and properties of the system [85]. Arvind et al. [86] showed the properties including thermal as well as mechanical of Li_2O-SiO_2-Al_2O_3-K_2O-B_2O_3-P_2O_5 glass-composites, which were developed by melt quenching methods. It was found that 3 h dwell time at 800^0C, the sample achieved good crystallinity. The properties such as optical, thermal, structural properties as well as mechanical properties of $Li_2O{\cdot}Na_2O{\cdot}K_2O{\cdot}ZnO{\cdot}B_2O_3$ and its effect on the system has been shown by Subhashini et al. [87]. An increase in Fe^{3+} content was observed to produce a small molar volume expansion, resulting in a rise in the number of ions available per unit volume, finally leading to the expansion of molar volume [87]. A slight increase in oxygen packing density (OPD) was observed with increasing Fe_2O_3 content, showing more compact packing of the oxide network. [87]. Mhareb et al developed $Li_2O{\cdot}B_2O_3{\cdot}MgO{\cdot}Nd_2O_3$ based glass systems by the melt quenching method. The glass system was showed an amorphous nature and confirmed by XRD analysis. Density, molar volume, refractive index, and ion concentration were reported to strongly depend on the concentration of Nd^{3+} [88].

2.6 Influence of V_2O_5, MoO_3, CdO, and ZnO on Glass Properties

Various researchers discussed the different compositions of V_2O_5, MoO_3, CdO, and ZnO chemical reagents to make glass nanocomposite system and their properties. Here, in this section effect of these chemical reagents on glass nanocomposites is also reported. V_2O_5 is a material that acts as a semiconductor. The compound having it as a base shows certain characteristics such as high electrical conductivity, thermal stability, etc. As compared to other transition-metal oxide glasses, it has a high glass formation range. There are several uses for this type of device, including optical switching devices, memory switching, and electrical thresholds [32]. There are many studies in which the colloquial structure of V_2O_5 glass was used. In this study, as colloquial structural units, the complicated structure of VO_4, VO_5, and VO_6 polyhedral were previously recommended [89-91].

The transition metal ions, vanadium, and molybdenum have more than one oxidation state respectively V^{4+}, V^{5+} and Mo^{+6}, Mo^{+7} in vanadate and molybdate glassy system, the electron conduction arises through thermally activated small-polaron hopping (SPH) between lower to higher oxidation state at higher temperature [40-41]. The incorporation of ZnO leads to improved chemical durability and also decreases the glass transition temperature [92]. The Cd^{2+} presence in the glassy system indicates the alteration of the physical and structural properties, resulting in the development of magnificent optical materials for various technological gadgets [93]. Report [94] exhibits that the activation energy as well as conductivity of the glasses that contain oxide that forms glass, MoO_3 is highly affected by modifier oxide.

The characteristics of network formers and network modifiers were reported to influence the structure of the vandate glassy system [95]. ZnO is the most important well-known semiconductor material and also acts as a piezoelectric material. ZnO semiconductor materials may be synthesized by doping other elements to increase the band gap or defect structure [97].

CdO is one of the useful semiconductor metal oxides. Various applications of CdOis are found in numerous scientific as well as industrial fields. The most recognizable properties after its kind are catalytic, electrical, and optical [98]. The nanocrystal of CdO is produced with the help of a single source precursor method. This is done at mild reaction conditions. Further, it is performed by a solvothermal route between CdO and element iodine. The nanocrystal of

CdO was characterized with the aid of XRD, FTIR, UV-vis, and cyclic voltammogram (CV) [98].

2.7 Review of V_2O_5·MoO_3·CdO·ZnO based Glass-Nanocomposites

Here, in this section past research of V_2O_5·MoO_3·CdO·ZnO-based glass-nanocomposites have been discussed. In his study [20], Desoky studied glass nanocomposites in the system 60 V_2O_5·(40 - *x*)B_2O_3·*x*BaO with values of x are 15, 20, 25, 30, and 40 mol%. This study leads to conclusions about their physical properties and the role of transport (density, hopping distance of hopping, radius of polaron, and DC activation energy). Sindhu et al. [23] prepared the glass nanocomposite systems V_2O_5·SrO·B_2O_3 and V_2O_5·B_2O_3·SrO by melt quenching method where x ranging from 0 to 20 mol%. They discussed the said glassy system's physical, morphology, optical, and electrical properties. Das et al. [99] reported the morphology, optical, and electrical properties of some V_2O_5·Nd_2O_3 semiconducting glass nanocomposites. Crystallite sizes and nano phases in the glassy system were verified by XRD and TEM analysis. Structural changes in part, relaxation in conductivity, and level of ionic conductivity of ZnO·$AgNO_3$· MoO_3 glass nanocomposites system were investigated by Kundu et al [22]. Bhattacharya et al. [100] investigated the temperature and frequency-dependent conductivity of a TMO-based V_2O_5-MoO_3–0.95ZnO semiconducting nano-glassy system. They interpreted the results of DC conductivity, as well as the AC conductivity of the samples. Applying the slow cooling method, Biswas et al [101] synthesized the MoO_3·SeO_2·ZnO-based bulk nano glassy composite materials. Physical as well as microstructural properties of as-prepared nano-glassy samples were measured with varying MoO_3 content (0.05 -0.3) in the system. Using XRD, FTIR, and UV–Vis spectra exploration, the structural part of these samples was characterized. Electrical conduction mechanisms (Both DC and AC conductivity) of the system were also investigated.

2.8 Iron-Doped Glass Systems: Insights and Challenges

Transition metal ions (TMI) like iron, vanadium, and tungsten-doped glass nanocomposites have shown especially interest due to electrical conduction [20, 28-29, 94, 102-103]. TMI-doped glass nanocomposites have shown semiconducting behaviour because they contain more than one valence state [104-105]. According to the report of various researchers [9-21], from low to high valence the hopping of electrons occurs due to the transition of $Fe^{2+}$and Fe^{3+}conduction. The phenomena of this transfer of charge in such glasses are traditionally called ‘‘small polaron hopping’’ (SPH) [106, 21]. The electrical conductivity

of nano glasses was reported to strongly depend on the distance between the iron ions [104-105, 107]. Various researchers have reported the effect of the iron doped in the nano glassy composites. R. Mohammadigharehbagh et al. [108] deposited the nano-crystal thin films of Fe-doped ZnO which on the Si and glass surfaces, using a thermionic vacuum arc (TVA). They examined the structural, optical, and electrical behaviours of this nano-crystal thin film. Different nanocrystallites were found in the film surface, which was reflected in the FESEM and analysis and they also reported the band gap was 3.15 eV.

Neupane et al [109] prepared the Fe-doped ZnO nanocrystal layers, where Fe varied from 0 to 20% applying a microwave technique. The layers were coated on Si solar cells using the spin coater. The results also showed that the Si solar cells have been improved for commercial applications in terms of their performance and quantum efficiency [5]. In Fe-doped ZnO coatings with a 15% Fe content, the crystallite size decreased and the coating became amorphous [109].

Sahai et al. [110] investigated the morphology, optical, and also vibrational properties of nanostructures of iron-doped ZnO. Due to the concentration dopant, prepared iron-doped nanostructures exhibited various morphologies such as nano particles, nanorods, nanocones, and nanoflakes. Somacescu et al. [111] reported the iron-doped $ZnO{\cdot}TiO_2$ thin films, which were applied in the field of the gas sensor. The iron-doped $ZnO{\cdot}TiO_2$ material was prepared by hydrothermal route.$ZnO{\cdot}TiO_2$ revealed a wurtzite-like structure. 25 nm average pore diameter was found in the nanomaterials. Xu et al [112] reported the switching phenomena of iron-doped ZnO thin films were enhanced. Fe-doped ZnO (Fe-ZnO) absorption was found to enhance the photocatalytic activity [113]. Fe^{3+} has been applied as a dopant material, to enhance the optical properties of ZnO as a semiconductor material, which was shown by Karmakar et al [114]. Inamdar et al. doped Fe in ZnO semiconductor. It is seen in their investigation that in the crystal networks, Fe^{3+} alters the Zn^{2+} state. These intern effects involve optical along with electrical characteristics of thin film which is deposited [115].

Studies have also shown that variation seen in the properties especially electrical of $Bi_2O_3{\cdot}Fe_2O_3{\cdot}P_2O_5$ glasses is independent of the presence of Bi_2O_3. The chief conduction is due to minute polaron that is hopping within the sites of Fe^{2+} and Fe^{3+}. Henceforth, the concentration of polaron dedicatedly keeps a check on the electrical conductivity in the glass of this type which in turn relies on the content of Fe_2O_3 and the ratio of $Fe(II)/Fe_{tot}$ [116].

2.9 Recent Studies Techniques to Analyse Microstructure of glass-nanocomposite

Researchers reported the microstructural effect of nanoglass composite materials. The microstructure of glass-nanocomposite has been investigated through XRD, FTIR, and also FESEM analysis. Parmar et al. [18] observed that the microstructure as well as the physical properties of the glass system consists of bismuth-silicate with the effects of Fe_2O_3. The role of Fe_2O_3 make a significant decline in density and molar volume. DCS analysis unfolded the fact that with the Fe_2O_3 content, the glass transition decreases in a broad domain of the glass formation zone. This is required essentially for the alteration of the microstructure as well as the other physical properties.

Aquino-Meneses et al. [19] observed that by introducing varying concentrations of CdO and V_2O_5 in the $CdO{\cdot}V_2O_5$ binary system, the conversion of crystalline to amorphous phase can be detected. Experimental studies make a view that the phases change with the varying concentrations of V_2O_5 and CdO. It is observed that the amorphous phase is due to the higher amount of molar concentration of CdO whereas higher gratitude molar concentration of V_2O_5 led to crystalline phase formation. XRD and Raman methods of spectroscopy reveal this kind of various phases in such glassy composites [19].

Desoky [20] reported and confirmed that the $V_2O_5{\cdot}BaO{\cdot}B_2O_3$ glass system showed amorphous in nature and was checked by XRD patterns. Ghosh and Chaudhuri [21] reported that the annealed $V_2O_5{\cdot}Bi_2O_3$ glass samples showed an amorphous nature up to 200^{o}C. Different nanoparticles (ZnO, $Ag_2Mo_2O_7$, Ag_2MoO_4, and $Ag_6Mo_{10}O_{33}$) dispersed in $ZnO{\cdot}AgNO_3{\cdot}MoO_3$glass nanocomposites system [22]. The Mo–O octahedral units were symmetric stretching, which is confirmed by FTIR spectra. The bond strength of Mo-O became feebler due to the increment of ZnO content in the composition [22]. The structure of the nano glass series of $V_2O_5{\cdot}SrO{\cdot}B_2O_3$ elaborated through FTIR spectroscopy. Here, three groups of combinations are analysed. 1200–1600 cm^{-1}, 800-1200 $cm^{-1,}$ and 700 cm^{-1} peaks were observed on account of the existence of the B-O-B band [23].

The result of FTIR analysis revealed that the wide peak close to 440–460 cm^{-1} peak found due to a distinct Zn-O stretching bond. At 865 cm^{-1} peak, bridging bonds Mo–O–Mo vibration were noticed. The stretching-type vibrations of MoO_6 octahedral groups were also observed at close to 912–917 cm^{-1} absorption peaks [101].

Machida and Eckert [117] explained the system $AgI{\cdot}Ag_2O{\cdot}MoO_3$, where the local structure of species of molybdenum was demonstrated. It was detected that in the glass containing an equal proportion of Ag_2O and MoO_3, molybdenum was found to form tetrahedral monomeric ortho-molybdate ions, MoO_4^{2-}. As a result of the NMR and vibrational spectroscopy tests, the MoO_4 tetrahedra and MoO_6 octahedra in this unit had the same structure as the chain ions found in crystalline $Na_2Mo_2O_7$.

2.10 Recent Studies on Electrical Properties of glass-nanocomposite

Various TMO-doped glass nanocomposites like CuO [14-15], V_2O_5 [7, 16], and Fe_2O_3 [13] are widely studied for the electrical conduction mechanism and also polaron hopping frequency.

A. Ghosh [17] investigated electrical conduction in bismuth-containing glasses. Electrical conduction in such nanocomposite glasses was reported to be due to the small polarons hopping between the TM ions.

Kuwata et al. [118] investigated the molybdate glasses with doped AgI where the progressive activation energy change is noticed and this would be ascribed to the transition between order and disorder in the crystal of α-AgI. The occurrence of ionic conductivity is because of the mobile ions and the motion can be described as cooperative liquid-like. The non-Arrhenius behavior is due to the network-like structure of glass in $AgI{\cdot}Ag_2O{\cdot}MoO_3$ glasses which is rapidly quenched.

Polaron hopping between two different oxidation states of iron i. e. Fe^{2+} and Fe^{3+} are primarily accountable for the conductivity in iron-containing glass nanocomposite and also conductivity depends on the iron oxide content [39]. In the polaron model, a conduction electron confined at one state in the system leads to the lattice alteration and it also stabilizes the localized electron [2, 36, 39]. The electron transitions from one state to another state through a hoping mechanism due to the thermal motion. A small polaron formed which indicates the presence of strong electron-phonon interaction [39].

Phosphate glasses with binary iron show a polaronic conduction mechanism and they are electronically conducting glasses [1, 2, 102]. The two valence states of iron were seen in this type of glass. Here the conduction (electrical) takes place with the aid of polaron hopping in the order of Fe (II) and then Fe (III). Small polarons are defects of the network of glass structurally because of the electron that messes with its surroundings and causes the movement

of its neighboring atoms that are in equilibrium states in the process of hopping. Therefore, charge carriers are small polarons. These are entrapped due to self-induced lattice distortions which transit is mainly of hopping that is phonon-aided [1, 2, 102].

In $Bi_2O_3 \cdot Fe_2O_3 \cdot P_2O_5$ glasses where Bi_2O_3 proportion tends to increase from 0 to 18.9 mol%, it is seen the dc conductivity increases at first and then shows a decreased order and the activation energy also decreases. The above whole phenomenon has a relation with a deduction of Fe_2O_3 concentration that is from 39.4 to 23.5 mol%. The nature or performance of this kind of conductivity strongly implies that it is determined by the concentration of Fe_2O_3 [116].

Desoky [20] reported the effect of DC electrical conduction on high temperature in the $V_2O_5 \cdot B_2O_3 \cdot BaO$ glassy system in terms of SPH theory by Mott's model. Activation energies for DC conductivity are also calculated. The hopping distance has been evaluated, which is estimated as 3.479–3.831 Å. With the increasing BaO content, decreasing hopping distance in the glass system.

Ghosh et al. [21] explained the dc conductivity of $V_2O_5 \cdot Bi_2O_3$semiconducting glasses taking 80, 90, and 95 mol% V_2O_5 in the temperature ranges from 80 to 480 K. Results showed dc conductivity of V_2O_5-Bi_2O_3 glass samples is maximum from $V_2O_5 \cdot TeO_2$ and $V_2O_5 \cdot P_2O_5$ glass nanocomposites. The nature of hopping is also estimated through polaronic conduction.

In the $V_2O_5 \cdot SrO \cdot B_2O_3$ glass system, DC conductivity showed in increasing order, and activation energy showed in decreasing order with the incorporation of V_2O_5. The nature of the electrical conduction process of all series of $V_2O_5 \cdot SrO \cdot B_2O_3$glass systems changed from ionic to polaronic. This is due to changes in materials' conductivity as well as activation energy [23].

A wide range of semiconducting nano-glassy composite [31-35] systems have been measured for AC conductivity to understand the mechanism of electrical conduction as well as defects. Several models were proposed to illuminate the AC conduction mechanism, including the QMT [42, 43], NSPT [43], OLPT [22], AH [43, 44], and the CBH model [45].

In the $V_2O_5 \cdot MoO_3 \cdot 0.95ZnO$ glass nanocomposites system, the free energy of polaron transition and AC activation energy were estimated [100]. The activation energy for the hopping frequency of the glassy system was also reckoned. DC conductivity of the glass samples showed a non-linear thermally activated nature, which was verified by the Vogel-Tammann-Fulcher model [100]. In the said system, the result of conductivity data showed that the NSPT model was best suited, when V_2O_5 content varied from 0.3 to 0.7. In contrast, to

define the AC conduction mechanism, the linked with CBH model was found most appropriate model for 0.9 and 0.93 V_2O_5 content glass samples [100].

2.11 Recent Studies on Mechanical Properties of glass-nanocomposite

Nowadays, the mechanical behavior of nanocomposites is crucial due to their exceptional chemical and physical attributes, making them highly useful in realistic scenarios [56]. Glasses and glass nanocomposite materials have shown more attention in research owing to their exceptional application in the field of solid-state ionic devices like electrochemical capacitors, gas sensors, fuel cells, analog devices, electrochromic displays, etc [119- 121]. In addition, due to its high mechanical properties, transparent glass-ceramics are greatly accepted materials for the protective cover of the new generation mobile phones [12-13]. A considerable number of studies have shown that mechanical properties are significantly influenced by factors such as composition, crystallinity, additives, residual stress, nucleating agents, crystal size, morphologies, and also durations of heat treatment [122–132].

2.11.1 Density and Molar Volume

Laila et al. [24] studied the density of a glassy system and its structural compactness. Density can be improved in some ways like increasing in total molecular mass and decreasing the molar volume. It has been also observed that the molecular mass gets decreased when V_2O_5 is interchanged by ZnO, this in turn decreases the density of the glassy system [24]. In the zinc vandate glassy system, the tunnelling was studied and there it was found that these compounds as such are lacking the conventional servitude of temperature and frequency [24]. Researchers [25] studied the bismuth borate glassy system by adding Fe_2O_3 to it. They found that the thermal stability is enhanced but the density and molar volume is reduced. Due to the network-modifying behavior of V_2O_5, the density of all the glass reduced linearly with increasing V_2O_5 content. With the inclusion of, V_2O_5 molar volume of the samples also increased in the systems $V_2O_5{\cdot}SrO{\cdot}B_2O_3$ and $V_2O_5{\cdot}B_2O_3{\cdot}SrO$ introduced by Sindhu et al [23].

2.11.2 Hardness Measurement

Hardness is a parameter that identifies the mechanical properties of a surface region of a solid [133]. The term "hardness" refers to a material's capacity to tolerate both permanent and plastic deformation during an indentation test. Hardness (Hv) is formulated in the term of a F/A ratio where F is represented as the applied load on the glass surface and A area of the surface expressed in micrometers square. A is the true area that is in the connection between

the pyramid and the material calculated at the height indentation load [134-137]. The surface area (A) can be determined by the subsequent formula:

$$A = \frac{d^2}{2\sin(\frac{136^\circ}{2})} \quad (2.1)$$

$$A \approx \frac{d^2}{1854.4} \quad (2.2)$$

During the past years, several research communities have been involved in scientific research on the micro-mechanical hardness of a nano-glassy material [46-47]. The parameters of microhardness measurement give valuable information about the composition of the materials. Apart from this, microhardness study also helps to measure the material's yield strength, young's modulus, and fracture toughness. There are various techniques like Brinell, Rockwell, Knoop, and Vickers microhardness to carry out the microhardness measurements. Several researchers claim that the Vickers microhardness method is the most practical way to assess microhardness [134, 138-141].

2.11.3 Vickers Micro-hardness

The Vickers microhardness of a nanoglassy material can be enhanced by accurately characterizing the microstructure of nanocomposites [47-48]. In Vicker's hardness (H_v) test, an indenter which is made up of diamond and generally resembles a pyramid having a square base is used for penetration against the specimen by using a specified force P. The apex angle (θ) of the indenter pyramid is 136º.

The value of H_V Can be calculated by the following formula:

$$H_V = \frac{F}{A} \approx 1854.4\frac{F}{d^2} \quad (2.3)$$

Where

H_v = Vicker's hardness number

F = applied load

d = diagonal length (mm) of the indent

A = true contact area.

According to various researchers, the ability of microhardness properties of nanocomposites can be perfectly used for the characterization of the indentation size effect (ISE) of said materials [48-50]. Ozturk et al, have shown in their study the H_v increases with raise in the load applied. In their system, the yield strength, young's modulus, and fracture toughness of the materials have been enhanced by increasing the microhardness with Ru doping [51]. Tian et al. reported the crystallization behavior, structural characteristics, and mechanical behaviour of $CaO{\cdot}Ta_2O_5{\cdot}Al_2O_3$ glass-ceramics [53].

2.11.4 Indentation Size Effect (ISE)

Among several mechanical experiment techniques, indentation hardness tests have supplied more reliable information on the materials' mechanical properties for practical applications and also for academic research over standard mechanical testing [48-49, 54-55].

The microhardness of materials is significantly affected by the applied force during indentation testing, a phenomenon referred to as the ISE. The ISE behaviour of a material is perceivable when the microhardness value diminishes with a raise in the applied test load [135, 142]. Various researchers reported that the ISE behaviour of a material depends on several factors during indentation, including dislocation loops [143], strain gradient [144], plastic deformation [145], elastic recovery [146], load hardening [146], etc. Numerous models, such as Meyer's law, proportional sample resistance (PSR), elastic/plastic deformation (EPD) models, and the Hays–Kendall(HK) approach, which links the applied indentation test load (P) to the diagonal length of the indentation (d), are documented in the literature to demonstrate the ISE behavior of materials [147–149]. The phenomenon of reverse ISE differs from ISE in that the value of microhardness rises as the functional test load increases [48-49].

2.11.4.1 Meyer’s law

The first recognized model to explain how applied stress affects the microhardness behavior of nano-glassy samples (ISE/RISE) is Meyer's law [48, 146, 150]. It is expressed as

$$P = Ad^n \qquad (2.4)$$

Where,

P = applied load

A = microhardness constant

d = diagonal length of the measured sample

n = Meyer number (or index).

A key factor in determining the ISE and reverse ISE behavior of glassy materials is the Meyer index value (n) [46, 48, 146, 150]. Three varied scales of n have been considered for the position of decision-making authority. The value of n is less than 2 indicating the usual ISE attitude [46, 48, 146, 150]. In this case, the value of microhardness is reduced when the applied load is increased. Again when the value of n is greater than 2 just the reverse of ISE (RISE) takes place. Now the value of microhardness is increased with the further rise of functional load. The last case i.e. when n=2 (Kick's law) depicts the value of microhardness as independent of the applied load. That is given by Kick's law [48, 146, 150].

$$P = A_0 d^2 \qquad (2.5)$$

Where A_0 is the indenter's geometric conversion factor.

2.11.4.2 Elastic/plastic deformation (EPD) approach

The EPD model is the majorly utilised method for comprehending the ISE and reversing the ISE behavior of glassy materials [124, 151]. The model mainly gives attention to the recovery generally elastic in nature that is formed in the surrounding locality of the indentation impression along with the formation of new bands which is plastically deformed. The size for the indentation which is dependent on load is as follows:

$$P = A_1 (d_p+d_e)^2 \qquad (2.6)$$

In this equation, A_1 is represented as a load-independent constant, d_p is the correctional term for plastic deformation and d_e is the correctional term for elastic deformation [124]. The constant values are determined from the straight lines which are best fitted in the $P^{1/2}$versus dp plot. It is regarded as general RISE nature when the elastic deformation value was less than 5 μm or negative. In addition, it may be positive in the case of regular ISE behavior. [48, 124].

The microhardness from the EPD model can be found using the formula (Eq. No. 2.7) in the manner described below.

$$H_{EPD} = 1854.4A_2 \qquad (2.7)$$

2.11.4.3 Proportional Specimen Resistance (PSR) Model:

Several researchers have used the PSR model to calculate load-dependent and load-independent microhardness at the saturation zone [150, 152-154]. This model [46, 133] states that the size of the indentation and the applied load have the following relationship.

$$P = Ad + Bd^2 \qquad (2.8)$$

Here A and B are the load dependence and load independent of the microhardness. The energy dispersion linked to sample crack regions is implied by parameter A. The values of A and B are extracted from the best linearly fitting in Eq. 2.8 and the indenter orientation and inherent structural elements are what determine the aforementioned values. The sample's surface energy, or A, might be either positive or negative. However, B's values are always positive. [152, 155]. The A value relies on the sample dislocation movement [152, 155].

According to this model, the Vicker's microhardness value can be evaluated by Eq. 2.9.

$$(H_V)_{PSR} = 1854.4B \qquad (2.9)$$

2.11.4.4 Hays Kendall (HK) approach

The HK point of view can be taken as a more acceptable approach to see the common features of mechanical behavior and load-independent microhardness parameters of a sample [145]. In this model when the materials are subjected to a minimum test load, both the phenomenon namely plastic and elastic are observed [145]. The load dependence hardness in this model can be written as [145]:

$$P - W = A_3\, d^2 \qquad (2.10)$$

Here W is the lowest load to start the deformation especially plastic in nature into the materials. A_3 is termed a load-independent constant. W and A_3 are determined from the best-fitted straight line of plots of the applied loads (P) against the square of the diagonal length (d^2). The indenter penetration is stationary up to a particular limit of the applied test load and above that the size of the indentation starts to rise abruptly [145]. This increase implies a more significant influence of elastic deformation over plastic deformation of the material. The effective load applied can be calculated by the following formula [145]:

$$P_{eff} = P\text{-}W \qquad (2.11)$$

The analogous values of $(H_V)_{HK}$ can be calculated by the relation as follows [145]:

$$(H_V)_{HK} = 1854.4\, A_3 \qquad (2.12)$$

2.11.4.5 Indentation-induced cracking (IIC) model

The IIC model, which came inti existence by Li and Bradt, provides a comprehensive framework for the analysis of the mechanical properties of materials, particularly those showing reverse ISE behavior [155-159]. Understanding load-dependent and load-independent microhardness of the nano-glassy samples under investigation is made much easier with the help of this model. In the IIC model, the Vickers microhardness (H_{VIIC}) is given by [155, 159]:

$$H_{IIC} = \lambda_1 K_1 (P/d^2) + K_2 (P^{5/3}/d^3) \qquad (2.13)$$

Where d is the diagonal length of the indentation, and λ_1, K_1, and K_2 are constants. K_2 is dependent on the applied test load P, while K_1 is a geometrical conversion factor dependent on the indenter's geometry [160-161].

For materials in a perfect plastic condition (λ_1=1 and $K_2(P^{5/3}/d^3)$ =0), the microhardness expression simplifies to $H_{IIC}=K_1(P/d^2)$. For perfect brittle materials (λ=0), it simplifies to $H_{IIC}=K_2(P^{5/3}/d^3)$.

To generalize, the IIC model can be rewritten as [48, 159]:

$$H_{IIC}=K(P^{5/3}/d^3)^m \qquad (2.14)$$

Where K and m are load-independent constants. The parameter m is crucial in determining the material's behavior: m > 0.6 indicates normal ISE behavior, while m<0.6 indicates RISE behavior [48, 50].

2.12 Conclusion

This chapter explored the various perspectives, including the theoretical background of glass, glass-nanocomposites, and their applications. Particularly the importance of transition metal oxide-based nanocomposites is discussed in the view of existing research works. Moreover, a thorough literature survey has identified the research gap in the development of nano-glassy composites and their structural effects.

CHAPTER-3

Experimental Procedure

Contents

Chapter-3

3.1 Introduction

This chapter is mainly concentrated on various chemical reagents which are used in the preparation of present nano-glassy composite samples. Synthesis of glass nanocomposite has been discussed in detail in this chapter.

For structural and physical characterization of a present nano glassy system, various methods like XRD, FT-IR, FESEM, and also density and molar volume measurements have been applied. In this chapter, these measurement techniques have been properly explained in detail. In all glassy systems, density is a crucial property employed to verify its internal structure. Generally, the high density of a glassy system indicates that the particles are closed-packed in the structure of glass nanocomposites. Due to variations in the composition of the glassy system, changes in the molar volume of that system and results show that alter the glass's structures [23-25, 162].

XRD study assists in determining the various crystallite phases carried out in a glass nanocomposite system. Values of the crystallite size, the average crystallite size, micro strain, and average dislocation density have been calculated [18-21]. Another significant structural characterization method is FT-IR analysis [23, 101, 117], which is generally used to get some practical information about a glassy system related to material quality, unidentified material identification, amount of various chemical components in a mixture, etc. FE-SEM is used to analyze the morphology of glasses and glassy nanocomposites.

To measure the electrical properties of a glassy system, AC and DC electrical conductivity data analysis is most important. Generally, AC conductivity data have been investigated through various models or techniques such as Power law [163], Almond West formalism [164], etc.

Vickers microhardness analysis is considered a prime technique for determining the mechanical properties of a glassy system.

3.2 Materials Used

In this present investigation, analytical grade reagent chemicals of Fe, V_2O_5, MoO_3, CdO, and ZnO (99% purity) were employed for the preparation of glassy samples. These

reagents were chosen to produce generic glass compositions with different ratios of network modifiers as well as network formers. Specifically, CdO plays a great role as a network modifier. V_2O_5 controlled the network former of these glassy systems. Additionally, ZnO played an important secondary role as a network former/ network modifier. The influences of these chemical reagents on glass nanocomposites have been discussed in the literature review chapter (Section 2.6) in detail.

3.3 Sample Preparation: Synthesis of glass nanocomposite

The glass nanocomposite forming compositions studied are presented by a general compositional formula:

$$xFe - (1\text{-}x)\ (0.3V_2O_5 - 0.2MoO_3 - 0.4CdO - 0.1ZnO)$$

Where, x varies among 0.0, 0.05, 0.1, 0.2, 0.3, 0.4, and 0.5. The glass nanocomposites were synthesized by the melt quenching technique. Using analytical-grade reagents, batches of glass were prepared based on their molecular weights. Various reagent-grade ingredients (in grams), including Fe (Sigma Aldrich), V_2O_5 (Loba Chemie), MoO_3 (Sigma Aldrich), CdO (Sigma Aldrich), and ZnO (Loba Chemie) (99% purity), were weighed on a precision electrical balance, the DHONA 200D (Fig. 3.1a) and homogeneously mixed in an agate mortar. We mixed mixtures (approximately 8.0 grams) in a crucible and melted them in an electric-heated furnace between 800-850^oC (Fig. 3.1b). Following an equilibration period of 30 minutes, the molten mass was quenched between two alumina plates at room temperature. In the present study, glassy flakes of 1mm thickness were obtained that were partially transparent.

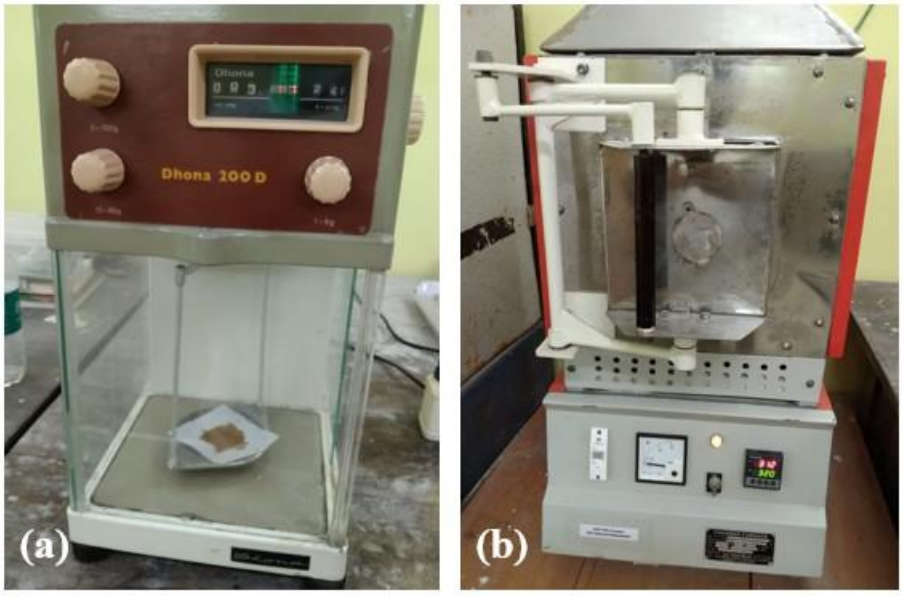

Fig 1: (a) Electrical balance, DHONA 200D (b) Electric-heated furnace

Table 3.1: Compositional ratio of glass nanocomposite xFe – (1-x) ($0.3V_2O_5$ – $0.2MoO_3$ – 0.4CdO – 0.1ZnO) on an 8 gm sample.

Values of x	Fe (gm)	V_2O_5 (gm)	MoO_3 (gm)	CdO (gm)	ZnO (gm)	Melting Temperature (^{0}C)
0	0	3.0557	1.6121	2.8765	0.4557	800
0.05	0.1612	2.994	1.5797	2.8185	0.4466	810
0.1	0.3330	2.9284	1.5450	2.7568	0.4368	820
0.2	0.7123	2.7836	1.4686	2.6203	0.4152	825
0.3	1.1481	2.6171	1.3808	2.4637	0.3903	835
0.4	1.6542	2.4238	1.2788	2.2817	0.3615	850
0.5	2.2486	2.1968	1.1591	2.0679	0.3276	890

3.4 Sample Characterization Techniques

In the present study, all nano-glassy composite samples have been characterized and investigated in different ways:

- Prepared glass samples have been characterized through microstructural and physical analysis.
- Prepared glass samples have been investigated through temperature-dependent electrical properties.
- Prepared glass samples have been characterized by their mechanical properties.

3.4.1 Microstructural Properties: Measurement Techniques

The importance of microstructural analysis of glass nanocomposite systems is already discussed in the literature review chapter in section 2.9. The microstructures of glass nanocomposites were investigated through different techniques like DSC, XRD, FTIR, and also FESEM analysis. Density, and the molar volume of the glass nanocomposites, are the most important properties that characterize the structures of the glass nanocomposites and are associated with electrical and mechanical behaviours.

3.4.1.1 Density and Molar Volume Measurements

Density (ρ) is a crucial physical variable for the determination of the changes in structure within a glass matrix. Throughout the glass matrix, it has become clear that density variation is important. Using Archimedes' method of applying non-solvent immersion liquid acetone (density of 0.78 g/cm^3 and 99% purity) at room temperature, the density of all prepared samples (x=0.0, 0.5, 0.1, 0.2, 0.3, and 0.4) was determined. In this study, for each sample, a measurement was repeated five times, and then the average value of density was taken.

The density of different glassy systems has been calculated using the Archimedes principle [84].

$$\rho = \rho_{\text{acetone}} \left(\frac{W_{air}}{W_{air} - W_{acetone}} \right) \quad (3.1)$$

Acetone was used as a solvent in this study. The weight of glass material in the presence of acetone and air is known as W_{air} and $W_{acetone}$. The density of acetone is $\rho_{acetone}$.

The following expression is used to reckon the molar volume (MV) of the glass system from the molecular weight and determined value of density [101].

The following expression for the molar volume

$$V_m = \sum \frac{x_i M_i}{\rho} \quad (3.2)$$

Here, x_i and M_i are the molar fractions and the molecular weight for i^{th} glass composition.

3.4.1.2 Fourier transform infrared (FTIR)

FTIR spectroscopic experiment of different glass nanocomposite samples (x=0.0, 0.05, 0.1, 0.2, 0.3, and 0.4) was recorded with a Bruker-Optics Alpha-T spectrophotometer (Fig. 3.2) over the range of 500 cm^{-1} to 4000 cm^{-1}. We have obtained pellets of thickness around~ 1mm using 1 part of the sample and 60 parts of KBr with the help pressing technique.

Fig. 3.2: Experimental set-up for FT-IR spectrophotometer

3.4.1.3 Differential scanning calorimetry (DSC) Analysis

DSC scans of individual glass nanocomposite samples were carried out in a DSC4000 (Perkin Elmer). Non-isothermal experiments were conducted at a heating rate of 20 °C/min within the temperature window from ambient to 850^{o}C using indium as a reference material.

3.4.1.4 X-ray powder diffraction (XRD)

Six different compositions of glass nanocomposite samples (x=0.0, 0.05, 0.1, 0.2, 0.3, and 0.4) were investigated by XRD. All glass samples were crushed and girded by Parkinson and agate mortar suitable for XRD analysis. XRD investigations were carried out in a (EMPYREAN) using Cukα X-rays and Ni filter (Fig. 3.3), and scanned in the range from 5^{o} to 80^{o} with a scanning speed of 2^{o} (2θ) per minute. The JCPDS numbers (ICDD–PDF2 database) were used to identify the developed crystal phases.

The crystallite sizes (d) of developed different nanocrystallites are calculated by the Debye–Scherrer equation [165].

$$d = \frac{0.89\,\gamma}{\beta \cos\theta} \qquad (3.3)$$

There are four characteristics of crystalline size: a) average crystalline size, b) Bragg diffraction angle, and c) width at half maximum (FWHM).

Fig. 3.3: X-ray powder diffraction (XRD) set-up

3.4.1.5 Field Emission-Scanning Electron Microscopy (FE-SEM)

A FE-SEM was used to explore the surface morphology and microstructure of the glassy system. In the present study, FESEM micrographs of polished surfaces of the glass nanocomposites of all six different batches (x= 0.0, 0.05, 0.1, 0.2, 0.3, and 0.4) were taken to investigate the microstructural development by Field Emission-Scanning Electron Microscope (FE-SEM, JEOL Model: JSM-7600F) (Fig-3.4).

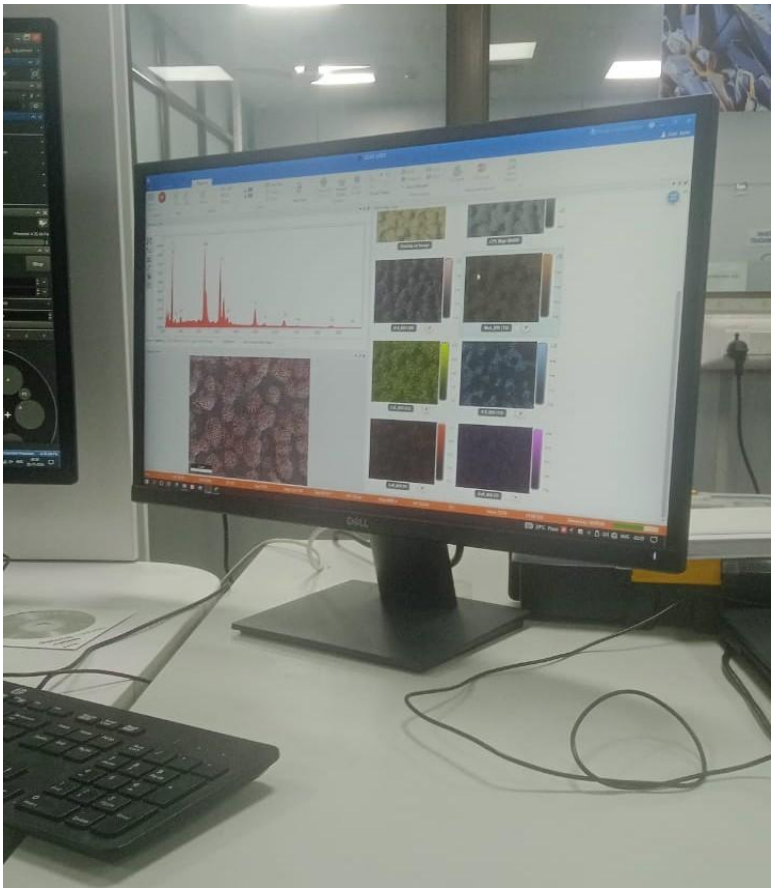

Fig. 3.4: FESEM and EDS set-up

3.4.2 Electrical Measurement of as-prepared samples

To characterize the electrical measurement, glass nanocomposites were resized and tested for area and thickness (~1 mm). Then, to get the electrodes, on either side of the glassy flakes were coated with silver. The Metravi digital meter (model no. 450 DMM) was then used to test the resistance of the glassy samples coated with silver paste at various temperatures. The experimental Setup for electrical measurement is shown in Fig. 3.5. A Hioki-made automatic high-precision LCR meter (Model No. 3532-50) was used to measure the AC electrical conductivity at various temperatures within the frequency range of 42 Hz to 5 MHz. AC conductivity of all the glassy samples (x=0.0, 0.05, 0.1, 0.2, 0.3, and 0.4) was analyzed by the Power Law and Almond-West formalism method.

Two probes of the DC electrical resistance of all-glass nanocomposite samples were measured using a Keithley Electrometer (Model No. 6514/E).

Fig. 3.5: Experimental set-up for electrical measurements

3.4.3 Mechanical Properties: Measurement Techniques

The importance of mechanical properties, mainly microhardness properties of glass nanocomposite systems already discussed in the literature review chapter in section 2.11. The microhardness of glass nanocomposites was measured through Vickers microhardness testing.

The accurate microhardness measurement values are determined by placing the cleaned and polished specimen's surface right perpendicular to the indentation direction of the respective testing machine.

For this test, samples were mounted in a suitable small cylindrical pipe with the help of cold mounting liquid and cold mounting powder. Using a different grade of emery paper, the top surfaces of the mounting samples were polished by the mechanical polishing machine (Fig. 3.7a). Finally, the sample's surfaces were smoothened by using the cloth-fitted mechanical disc polishing machine (Fig. 3.7b).

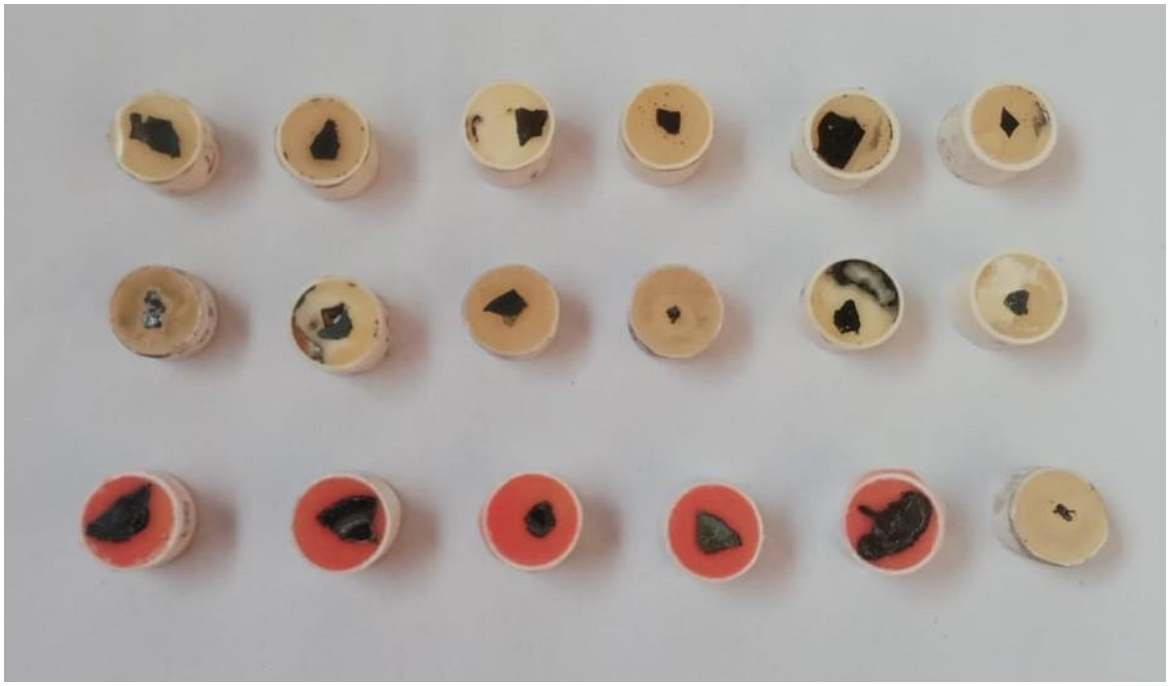

Fig. 3.6: Some polished glassy samples for microhardness measurement

Vickers Microhardness measurement of all glass nanocomposite samples was performed by using indentation with a digital Vickers microhardness tester (MATSUZAWA, MMT-X) at room temperature. (Fig. 3.8). The indentation load was applied for 10 s dwell time using five loads ranging from 0.049 N to 0.980 N. The indenter was applied at five regions of each sample surface for each load.

The load-dependent Young's modulus (E), Yield strength (Y), and modulus of rigidity or shear modulus (G) have been calculated following equations [134-137]:

$$E = 81.9635\ H_v \quad (3.4)$$

$$Y = (H_v/2.9)*[1-(n-2)]*[\{12.5(n-2\})/\{1-(n-2)\}]n-2 \text{ , for } n > 2 \quad (3.5)$$

$$Y = H_v/3 \text{ , for } n < 2 \quad (3.5.1)$$

$$G=H_v/0.151 \quad (3.6)$$

where, n = Meyer's index

Meyer's index (n) has been elaborated in Eq. (2.4) in Section 2.11.4.1 of chapter 2.

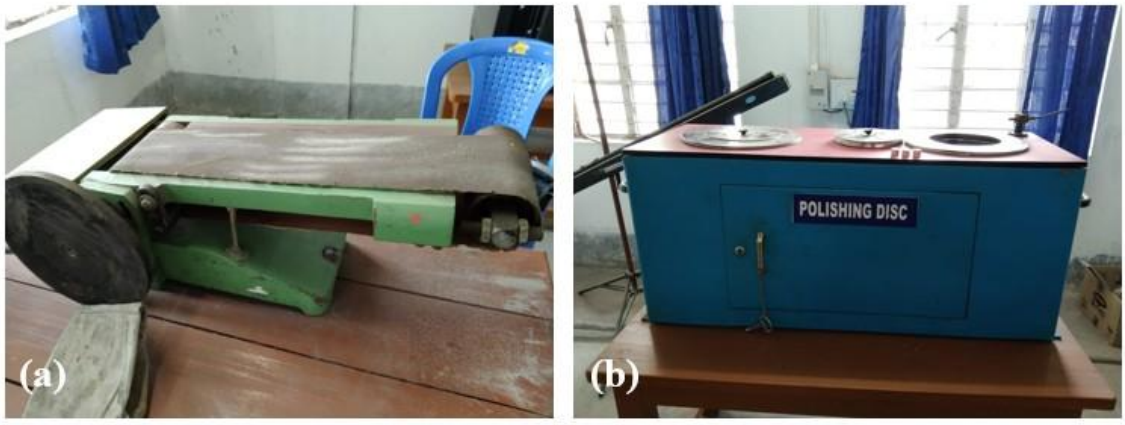

Fig. 3.7: (a) Mechanical polishing machine **(b)** Mechanical disc polishing machine

Fig. 3.8: Experimental Set-up for Microhardness tester (MATSUZAWA, MMT-X)

3.5 Conclusion

V_2O_5, MoO_3, CdO, and ZnO were used as chemical reagents for developing the glass nanocomposites system. Here, transition metal Fe is used as doping material in the glass system. The structural analysis of developed glass nanocomposites was investigated through FT-IR, DSC, XRD, and FESEM. The electrical properties of as prepared glass composites system were tested through AC and DC conductivity and mechanical properties were examined by Vickers microhardness testing.

CHAPTER-4

Results and Discussions

Contents

Chapter-4

4.1 Microstructural Evaluation of $Fe{\cdot}V_2O_5{\cdot}MoO_3{\cdot}CdO{\cdot}ZnO$ Glass Nanocomposite System

4.1.1 Introduction

Glass-nanocomposites exhibit atomic arrangements that resemble those found in crystalline materials, although their structure is irregular, reflecting local order [166]. These materials are classified as non-crystalline solids. But, there is an area that needs to undergo well enough on the effect of nano-sized inclusions on mechanical properties [167-168]. Research indicates that reducing the size of inclusions significantly influences mechanical properties, underscoring the need for further investigation [169-171].

The interest in glassy systems has surged in recent years due to their extensive uses [1, 2]. Oxide glass systems containing transition metal ions are particularly noteworthy because of their semiconducting behavior. These materials have found applications in gas sensors, solar cells, laser di odes, and photocatalysis [7-9]. Additionally, they exhibit properties such as electrical threshold behavior, switching phenomena, and electrochromic effects [7-9].

The mechanical properties of these materials are closely linked to their microstructure. Key factors such as the morphology of the reinforcing phase—its size, shape, and distribution—play a critical role. The processing techniques and the chemical composition of the material influence these characteristics.

This chapter focuses on the prepared samples' mechanical and electrical characterization and structural analysis. Techniques such as XRD and FESEM were employed to analyze the microstructure's qualitative and quantitative aspects.

The primary goal of this investigation is to obtain an inclusive understanding of the behaviour and properties of glassy systems, particularly their potential to contribute to technological advancements. The insights obtained from this research can pave the way for the evolution of novel materials tailored for special uses in critical technological domains.

4.1.2 Density and Molar Volume Analysis

The density (ρ) is a fundamental physical parameter critical for studying structural changes within a glass matrix. Variations in density provide insight into the structural

compactness and atomic arrangement within the glass system. In this study, the density of various glassy systems was calculated using Archimedes' principle, as expressed by the following equation [84].

$$\boldsymbol{\rho} = \boldsymbol{\rho}_{\text{acetone}} \left(\frac{\boldsymbol{W_{air}}}{\text{W}_{\boldsymbol{air}} - \text{W}_{\boldsymbol{acetone}}} \right) \qquad (4.1.1)$$

Here, acetone has been used as a solvent. W_{air} and $W_{acetone}$ are the weight of glass material in the presence of air and acetone. $\rho_{acetone}$ is the density of acetone.

The following expression is utilised to reckon the molar volume (MV) of the glass system from the molecular weight and measured value of density [101].

$$\boldsymbol{V_m} = \sum \frac{\boldsymbol{x_i M_i}}{\boldsymbol{\rho}} \qquad (4.1.2)$$

Here, xi and Mi are the molar fractions and the molecular weight for i^{th} glass composition.

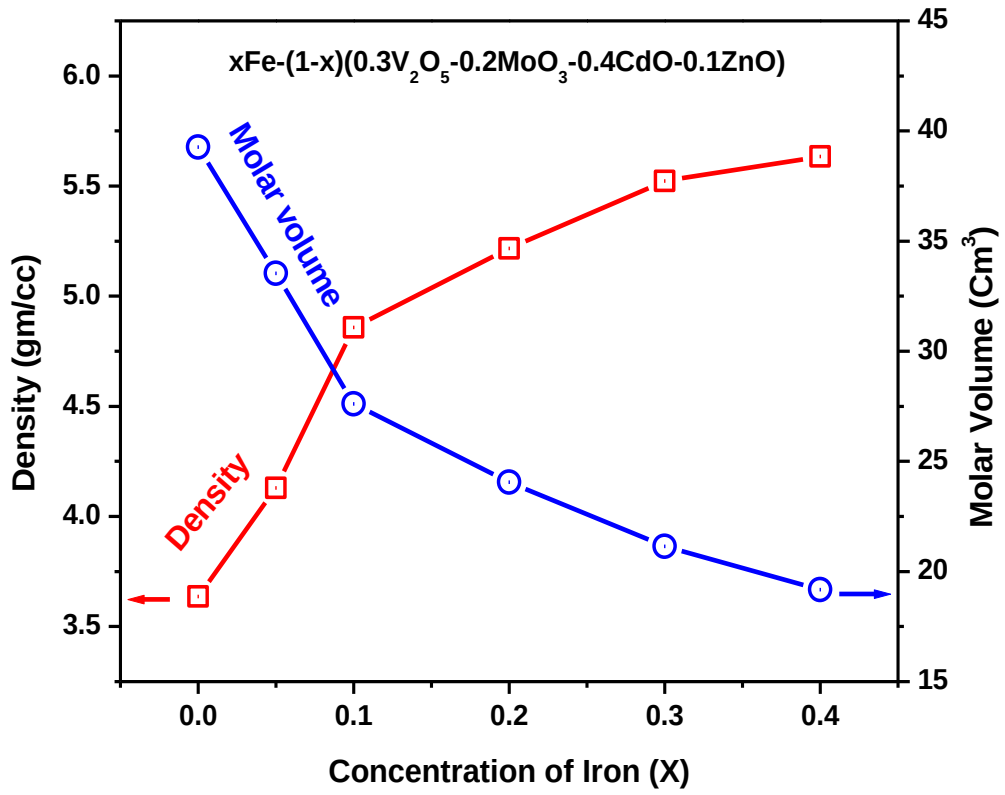

Fig. 4.1.1: Density and Molar volume of xFe – (1-x) $(0.3V_2O_5 – 0.2MoO_3 – 0.4CdO – 0.1ZnO)$ glass nanocomposite where x = 0.0, 0.05, 0.1, 0.2, 0.3, and 0.4.

A variation in the density and molar volume of Fe-containing samples has been shown in Fig. 4.1.1. As can be noticed in Fig. 4.1.1 density and molar volume change in the opposite direction. In general, density has increased with the increase in higher molecular weight. The density and molar volume of the Fe undoped (x=0.0) along with the other Fe doped glass samples (x= 0.5, 0.1, 0.2, 0.3, and 0.4) are shown in Table 4.1.1 Despite this, the density in the present study increases as Fe concentration increases, while V_2O_5 modifies the glass network and increases its compactness. An increase in non-bridging oxygen may cause a fall in density with increasing V_2O_5 levels [101, 171-175]. Increased non-bridging oxygen along with different nanophases of V_2O_5 [176-178] in the glass matrix is responsible for the increase in molar volume caused by adding V_2O_5. Changes in density and molecular weight determine molar volume changes. With an increase in Fe (x) content, molar volume increases along with molecular weight and density.

Table 4.1.1: Density and molar volume of the glass nano composite xFe – (1-x) ($0.3V_2O_5$ – $0.2MoO_3$ – 0.4CdO – 0.1ZnO) glass nanocomposite systems where, x = 0.0, 0.05, 0.1, 0.2, 0.3, and 0.4.

sample	**Density (gm/cm^3)**	**Molar vol. (cm^3)**
x=0.0	3.64	39.28
x=0.05	4.13	33.55
x=0.1	4.86	27.62
x=0.2	5.22	24.15
x=0.3	5.52	21.14
x=0.4	5.63	19.19

4.1.3 Fourier transforms infrared (FT-IR) Spectra Analysis

Figure 4.1.2 illustrates the FT-IR spectra for the glass system with varying compositions of x = 0.0, 0.05, 0.1, 0.2, 0.3, and 0.4 of the glass system. The band appears at

1617 and 3450 cm^{-1}, which indicates the existence of asymmetric stretching vibrations of O-H bonds [83]. The band appears at 810-780 cm^{-1}, which is mainly accountable for the creation of the vibration of Cd-O [98]. The crystal structure of zinc vanadium oxide [ZnV_2O_6] is built up from VO_5 groups bonded in a chain by common edges (V_2O_2 units) [179]. The bands at 810 and 950 cm^{-1} may be associated with the stretching vibration V_s and V_{as} of VO_2 units in ZnV_2O_6 [178, 180]. The primary units V_2O_7 of $Zn_2V_2O_7$ in which $2VO_4$tetrahedra groups are linked with corners (V-O-V bridges) and 3 terminal V-O bonds form VO_3 units [181]. The band at 950 cm^{-1} is associated with the stretching vibration V_s while V_{as} of 810 cm^{-1} [182]. The main structural groups of $Zn_3V_2O_8$ are separated VO_4 tetrahedra and observed bands may be designated to νs and νas of separated VO_4 [183]. The band appears at 950 cm^{-1} due to the stretching vibrations of Mo-O [184-185]. The stretching vibration of mixed bridging V–O–Fe and V–O–Fe might be in the range of 500-530 cm−1 [186]. In all samples, the band appears at 2850 and 2930 cm^{-1} due to the water and hydrogen bonding [187-188]. Due to the presence of asymmetric stretching vibrations, the band is visible at 1390 cm^{-1} [187]. Due to the existence of vanadium content, each batch exhibits some minor differences, including the appearance of a shoulder at approximately 1617 cm^{-1}[187-188]. Higher Fe concentrations should result in lower energy requirements to vibrate the Zn-O and V-O bands. Acoustic phonon vibrations are aided by ZnO nanophases [184]. This finding leads us to believe that the current glass nanocomposites containing greater Fe are unstable due to acoustic phonon vibrations. This conclusion is supported by XRD analysis results that show an increase in the average dislocation density and a decrease in structure stability with increasing Fe content.

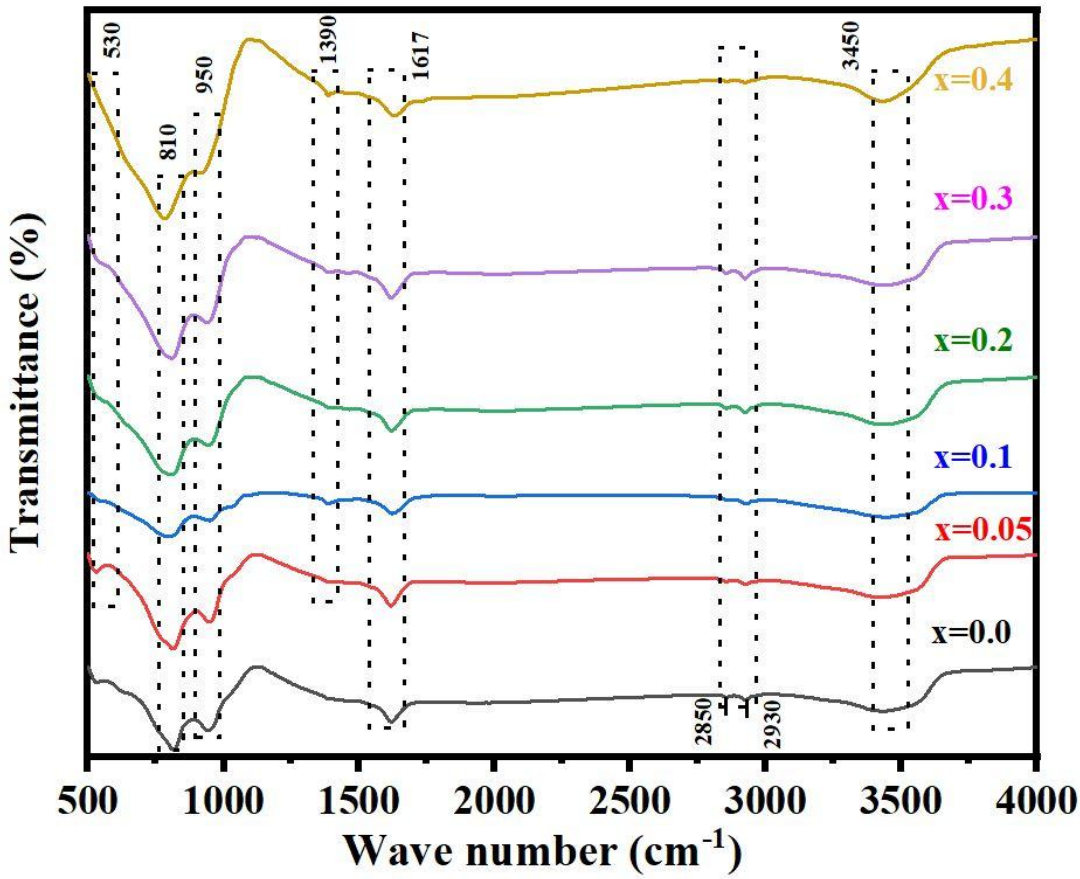

Fig. 4.1.2: FTIR plot of xFe – (1-x) ($0.3V_2O_5$ – $0.2MoO_3$ – 0.4CdO – 0.1ZnO) glass nanocomposite systems with different x values.

4.1.4 Differential scanning calorimetry (DSC) Analysis

Glass transition temperature (T_g) of all prepared samples (x=0.0, 0.05, 0.1, 0.2, 0.3, and 0.4) are presented in Fig. 4.1.3, which are characteristic from the endothermic baseline shift of the DSC plots. Figure 4.1.3 shows one crystallization peak (T_P^1) formed in x=0.0 and x=0.05 samples. Other hand when Fe concentration has been increased gradually, another crystallization peak (T_P^2) has been initiated. The results show a consistent increase in T_g values with the rising Fe (x) content in the glass system. The continuous increase in T_g can be primarily linked to the enhanced crosslink density and alterations in the bonding nature within the quaternary glass system [189]. In a glass matrix, T_g is heavily influenced by the degree of network connectivity, which depends on the type and number of bridging oxygens formed between glass-forming constituents. The incorporation of Fe ions contributes to the emergence of stronger Fe-O and Fe-V bonds, thereby raising the network rigidity and, consequently, the glass transition temperature. The findings align with previous studies that have highlighted the

critical influence of crosslink density and bond strength on the thermal properties of glass systems [189-191]. The gradual increase in T_g with Fe content reflects the interplay between compositional changes, structural rearrangements, and the presence of crystalline phases, offering valuable insights into the thermal behaviour of the glass nanocomposites [189-191].

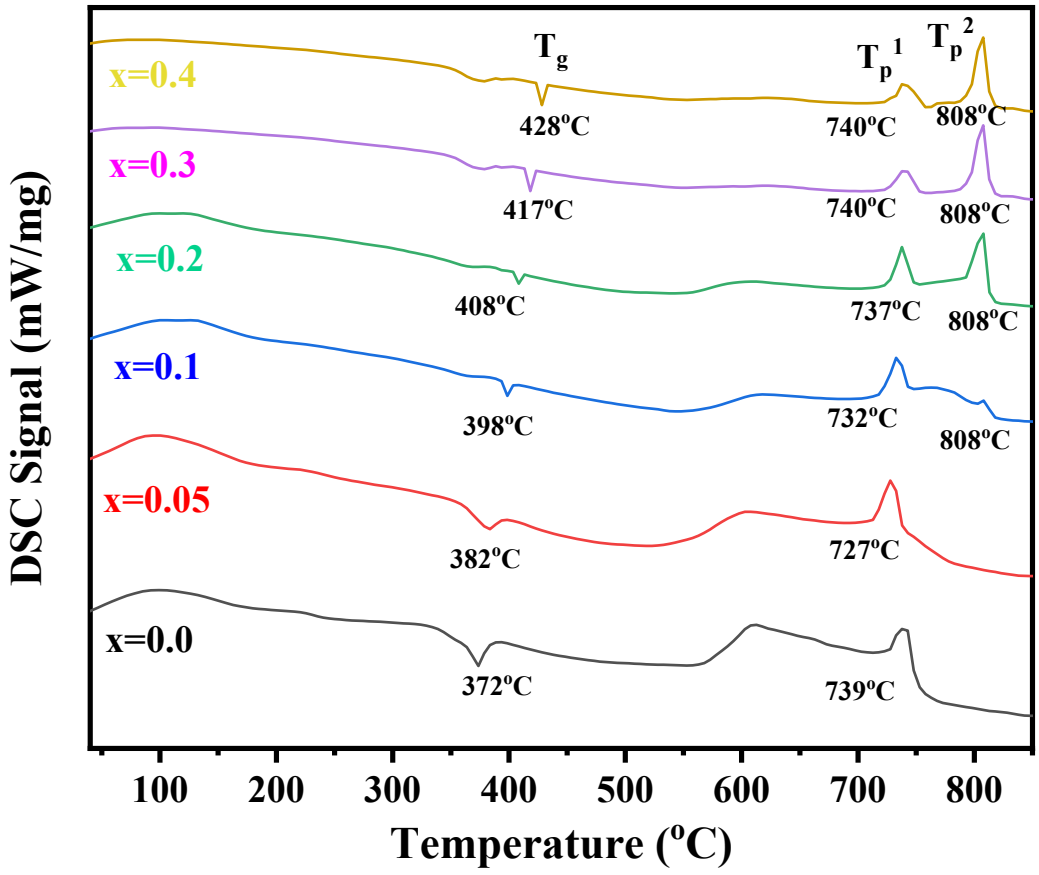

Fig. 4.1.3: DSC analysis plot of xFe – (1-x) ($0.3V_2O_5$ – $0.2MoO_3$ – 0.4CdO – 0.1ZnO) glass nanocomposite where, x= 0.0, 0.05, 0.1, 0.2, 0.3 and 0.4.

4.1.5 X-ray Diffraction (XRD) Analysis

Figure 4.1.4 displays the XRD patterns of all prepared (x= 0.0, 0.05, 0.1, 0.2, 0.3, and 0.4) glass nanocomposite samples. The various crystal phases were grown in each of the as-prepared samples and were recognized using the JCPDS reference files. The crystal phase of zinc vanadium oxide (ZnV_2O_6) [Zn_1V], $Zn_2V_2O_7$ [Zn_2V], and $Zn_3V_2O_8$ [Zn_3V] are observed as a major phase in all samples of prepared samples [192]. Characteristic peaks of cadmium vanadium oxide ($Cd_2V_2O_7$) [CdV] and vanadium molybdenum oxide (V_2MoO_8) [VMo] appear

in all prepared samples. Apart from that Fe added sample has two new peaks of iron vanadium oxide ($FeVO_4$) [FeV] appear along with other major and minor peaks.

Crystallite size (d) of different nanocrystallites was estimated using Debye–Scherrer equation [165].

$$d = \frac{0.89\,\gamma}{\beta \cos\theta} \qquad (4.1.3)$$

Where,

d = is the average crystalline size

λ = wavelength of the Cu-Kα X-ray (1.54 Å) radiation

2θ = Bragg diffraction

β = full width at half maximum

The average nanocrystalline size decreases with increasing the Fe (x) content (Table 4.1.2). The average dislocation density values for different Fe contents in the glass samples as shown in Table 4.1.2. Further, the dislocation density increases with raising Fe content in the developed samples. The enhancement of dislocation density may reduce structural stability [193]. Therefore, a rise in the addition of Fe content may result in a reduction in crystallite size and a consequent rise in system fragility. In general, density and molar volume results agree well with the average nanocrystalline size. The average nanocrystalline size decreases as the Fe (x) content increases, which may be conducive to healthier electrical transport phenomena.

Figure 4.1.5 shows the decomposition of the initial crystal phases along with all other phases and it seems as an amorphous phase containing samples.

Figure 4.1.6 displays the XRD patterns of the heat-treated samples (x=0.4) subjected to different heat treatment conditions (1h, 3h, and 5h). The various crystal phases developed in each of the heat-treated samples were recognized using the JCPDS reference files. In Fig. 4.1.6, the major crystal phases observed for x=0.4 include zinc vanadium oxide (ZnV_2O_6), $Zn_3V_2O_8$, cadmium vanadium oxide ($Cd_2V_2O_7$), and iron vanadium oxide ($FeVO_4$) [192,194-198]. From Fig. 4.1.4 and Fig. 4.1.6, it can be observed that different heat treatment conditions (1 h, 3 h, and 5 h) lead to notable changes in the intensity of various peaks in the sample of x=0.4. The peaks corresponding to iron vanadium oxide ($FeVO_4$) show an increase in intensity [199-201]. Additionally, the crystal phases of zinc vanadium oxide ($Zn_3V_2O_8$) [Zn_3V] are also observed, with their intensity increasing compared to the sample (x=0.4) without heat treatment.

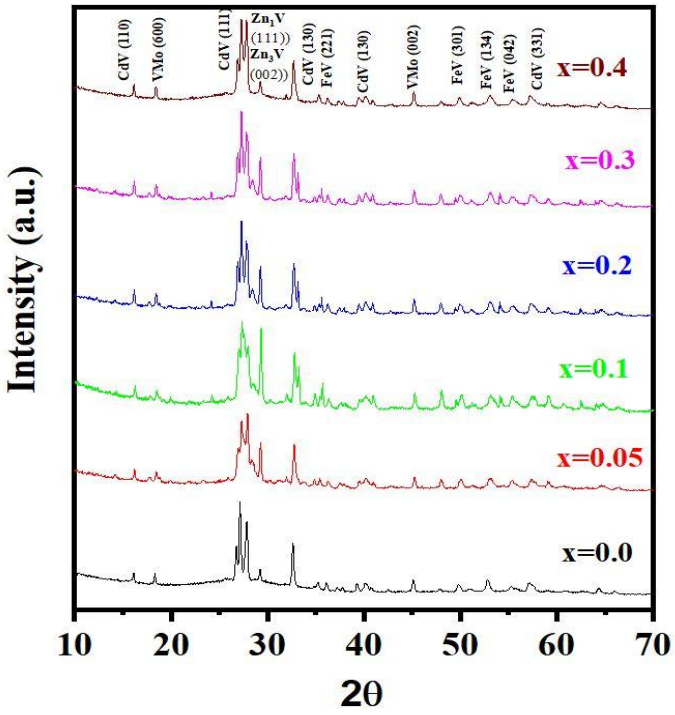

Fig. 4.1.4: XRD plot of xFe – (1-x) ($0.3V_2O_5$ – $0.2MoO_3$ – 0.4CdO – 0.1ZnO) glass nanocomposite with different x values.

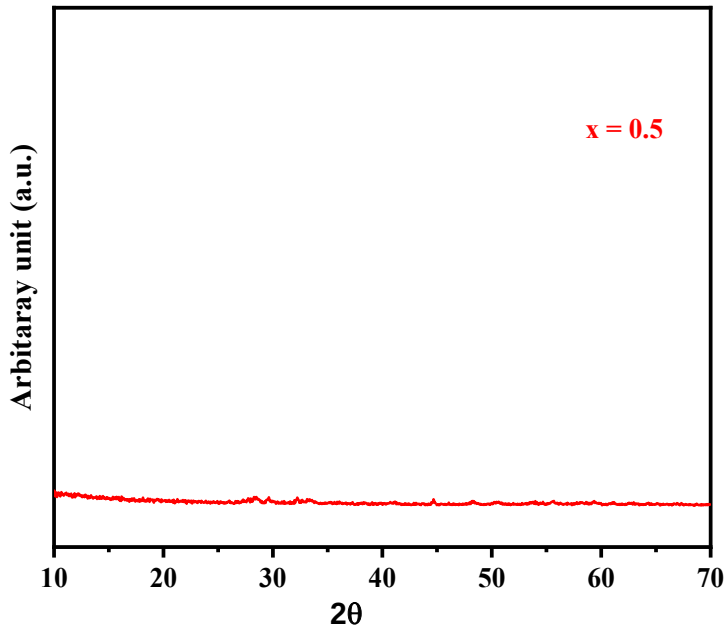

Fig. 4.1.5: XRD plot of xFe – (1-x) ($0.3V_2O_5$ – $0.2MoO_3$ – 0.4CdO – 0.1ZnO) glass nanocomposite where, x= 0.5.

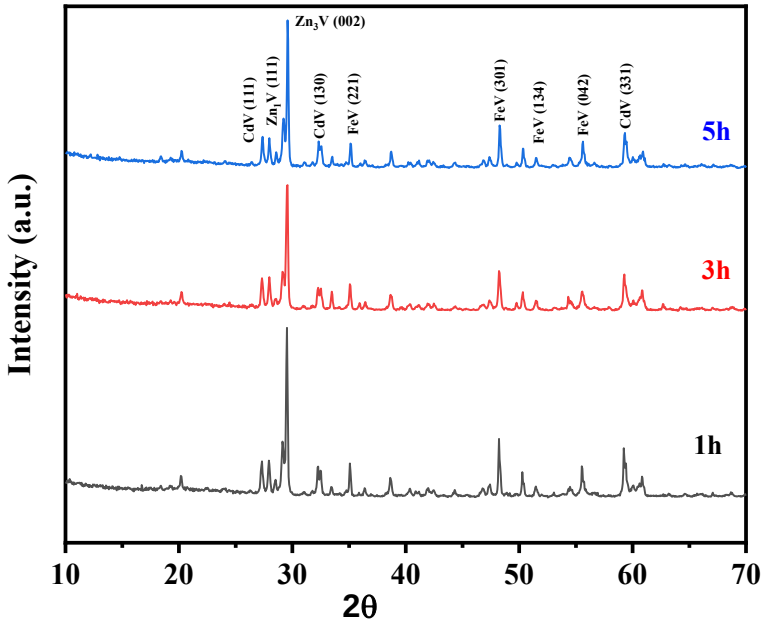

Fig. 4.1.6: XRD patterns of the developed system, xFe – (1-x) ($0.3V_2O_5$ – $0.2MoO_3$ – 0.4CdO – 0.1ZnO) where x= 0.4 at different heat treatment conditions (1h, 3h and 5h).

[Zn1V- Zinc Vanadium Oxide {ZnV_2O_6} (JCPDS Ref. file- 75-1392); Zn_2V-Zinc Vanadium Oxide {$Zn_2V_2O_7$} (JCPDS Ref. file- 70-1532); Zn_3V-Zinc Vanadium Oxide {$Zn_3V_2O_8$} (JCPDS Ref. file- 34-0378); VMo- Vanadium Molybdenum Oxide {V_2MoO_8} (JCPDS Ref. file- 74-1510); CdV-Cadmium Vanadium Oxide {$Cd_2V_2O_7$} (JCPDS Ref. file-78-1182); FeV-Iron Vanadium Oxide {$FeVO_4$} (JCPDS Ref. file- 71-1592)]

Table 4.1.2: Different parameters, i.e., FWHM, average crystallite size, average microstrain, and average dislocation density obtained from XRD study of the system, with various x values.

x	2θ (degree)	FWHM	Crystallite Size (nm)	Avg. Crystallite Size (nm)	Micro strain (∈)	Avg. Micro strain (∈)	Avg. Dislocation density (nm^{-2})
0	16.11	0.41261	20.3	29.11	0.01272	0.00539889	0.001179461
	26.74	0.50035	17.03		0.00919		
	27.12	0.29277	29.14		0.0053		
	27.85	0.22236	38.42		0.00391		
	29.21	0.19269	44.48		0.00323		
	32.62	0.23763	36.36		0.00354		
	45.09	0.26403	34.01		0.00277		
	52.76	0.34504	26.83		0.00304		
	57.09	0.60945	15.49		0.00489		
0.05	16.16	0.20275	41.31	30.24	0.00623	0.00503429	0.00109308
	18.42	0.20275	41.44		0.00546		
	26.89	0.23631	36.08		0.00431		
	27.27	0.63392	13.46		0.0114		
	27.86	0.2029	42.11		0.00357		
	29.25	0.2006	42.73		0.00335		
	32.68	0.32162	26.87		0.00479		
	35.29	0.20856	41.73		0.00286		
	40.15	0.86624	10.19		0.01034		
	45.15	0.23014	39.03		0.00242		
	49.84	0.26378	34.67		0.00248		
	52.98	0.49241	18.82		0.00431		
	55.32	0.46131	20.3		0.00384		
	57.39	0.64248	14.71		0.00512		
0.1	16.2	0.1998	41.92	28.06	0.00613	0.00642688	0.001269722
	18.46	0.2029	41.41		0.00545		
	25.91	0.2538	33.53		0.00481		
	26.91	0.2728	31.26		0.00498		

x	2θ (degree)	FWHM	Crystallite Size (nm)	Avg. Crystallite Size (nm)	Micro strain (∈)	Avg. Micro strain (∈)	Avg. Dislocation density (nm^{-2})
	27.29	0.592	14.41		0.01064		
	27.93	1.3775	6.2		0.02417		
	28.37	0.2428	35.23		0.00419		
	29.27	0.21983	38.99		0.00367		
	35.43	0.21027	41.4		0.00287		
	40.17	1.25703	7.02		0.015		
	45.22	0.22711	39.56		0.00238		
	47.96	0.226	40.16		0.00222		
	52.98	0.49241	18.82		0.00431		
	55.32	0.46131	20.3		0.00384		
	57.39	0.64248	14.71		0.00512		
	59.05	0.39551	24.1		0.00305		
	16.2	0.20788	40.29		0.00637		
	18.4	0.22687	37.03		0.00611		
	27.3	0.35889	23.78		0.00645		
	27.8	0.44861	19.04		0.00789		
	29.7	0.4106	20.89		0.00676		
	32.7	0.65138	13.27		0.00969		
	35.5	0.37504	23.22		0.00511		
x=0.2	40.2	0.37023	23.85	26.44	0.00441	0.005128	0.001431
	45.2	0.21303	42.17		0.00223		
	47.9	0.22726	39.93		0.00223		
	49.9	0.38606	23.69		0.00362		
	53.1	0.49619	18.68		0.00433		
	54.1	0.56904	16.36		0.00486		
	57.3	0.23825	39.67		0.00191		
	59.4	0.64716	14.75		0.00495		
	16.29	0.19005	44.08		0.00579		
x=0.3	18.4	0.20641	40.71	25.22	0.00556	0.006435	0.001572
	27.39	1.22075	6.99		0.02186		

x	2θ (degree)	FWHM	Crystallite Size (nm)	Avg. Crystallite Size (nm)	Micro strain (∈)	Avg. Micro strain (∈)	Avg. Dislocation density (nm^{-2})
	27.8	0.1753	48.74		0.00308		
	29.7	0.2728	31.45		0.00449		
	33.2	0.62754	13.79		0.00918		
	35.9	0.32411	26.89		0.00437		
	40.6	1.05245	8.4		0.01241		
	45.5	0.23135	38.87		0.00241		
	48.3	0.2791	32.58		0.00271		
	50.4	0.44882	20.42		0.00416		
	53.4	0.7267	12.77		0.0063		
	54.4	0.66651	13.99		0.00566		
	57.7	0.7157	13.23		0.00567		
	59.5	0.37606	25.4		0.00287		
x=0.4	16.4	0.25165	32.71	22.76	0.00776	0.008742	0.001921
	18.8	0.21881	38.42		0.00577		
	27.5	1.44038	20.92		0.02568		
	29.7	0.52896	26.22		0.0087		
	33.2	0.82646	20.47		0.0121		
	35.9	1.10467	17.89		0.01488		
	40.5	1.18605	17.45		0.01403		
	45.5	0.2265	39.69		0.00236		
	48.2	0.41901	21.68		0.00409		
	50.2	0.02694	40.36		0.00211		
	53.4	0.53527	7.34		0.00464		
	54.4	0.44534	20.14		0.00378		
	57.7	0.68632	8.79		0.00544		
	59.4	1.44432	6.61		0.01105		

4.1.6 Field emission-scanning electron microscopy (FE-SEM) analysis

FE-SEM was used to examine the morphologies of the present glassy samples (x=0.0, 0.05, 0.1, 0.2, 0.3, and 0.4). The plate-like crystals have been observed in the microstructure with an average crystal size of 10-15 nm in the Fe undoped sample (x=0.0) shown in Fig. 4.1.7a. The plate-like crystals disperse throughout the glass matrix. In sample x=0.05, uniform and dense microstructures have been found where the dendrite structure (average size of 15-20 nm) crystal develops (Fig. 4.1.7b). The dendrite crystal structures $FeVO_4$ along with other cadmium and molybdenum-rich crystal phases [202-203]. The interlocking dendrite crystal structure appeared (average size 1-5 nm) in the x=0.1 sample (Fig. 4.1.7c). As Fe doping concentration increases from x=0.05 to x=0.4, a noticeable growth in the size of the dendritic crystals is observed. The present samples x= 0.05, 0.1, 0.2, 0.3, and 0.4 (Figures 4.1.7 b–f) display progressively larger dendrites, suggesting enhanced nucleation and growth of crystalline phases due to the presence of Fe. The glass matrices in all samples with Fe are covered with needle-like crystals. The undoped sample (x=0.0) primarily consists of smaller dendritic crystals. In contrast, Fe-doped samples show increased crystal sizes, indicating that Fe incorporation promotes crystallite growth. The dendrite crystal structures have appeared as definite high-order assemblies. The different crystal phases of $Cd_2V_2O_7$, V_2MoO_8, and $FeVO_4$ were identified by XRD analysis (Details in section 4.1.5 of chapter 4), which corroborates the FE-SEM observations [198-201, 204]. During crystallization, Fe facilitates the formation of these phases due to its chemical composition in glass. The presence of $FeVO_4$ nano crystallites in Fe-doped samples further underscores the influence of Fe indicating the crystalline phase composition. These iron vanadium oxide crystallites coexist with cadmium and molybdenum-rich phases, suggesting a multi-phase microstructure that evolves with Fe doping. Despite the variation in dendritic crystal sizes, the overall distribution of crystals remains relatively uniform across the samples [192, 204]. This uniformity indicates that the melt-quenching process employed in synthesizing the glass nanocomposites is effective in achieving consistent microstructural characteristics across different Fe concentrations.

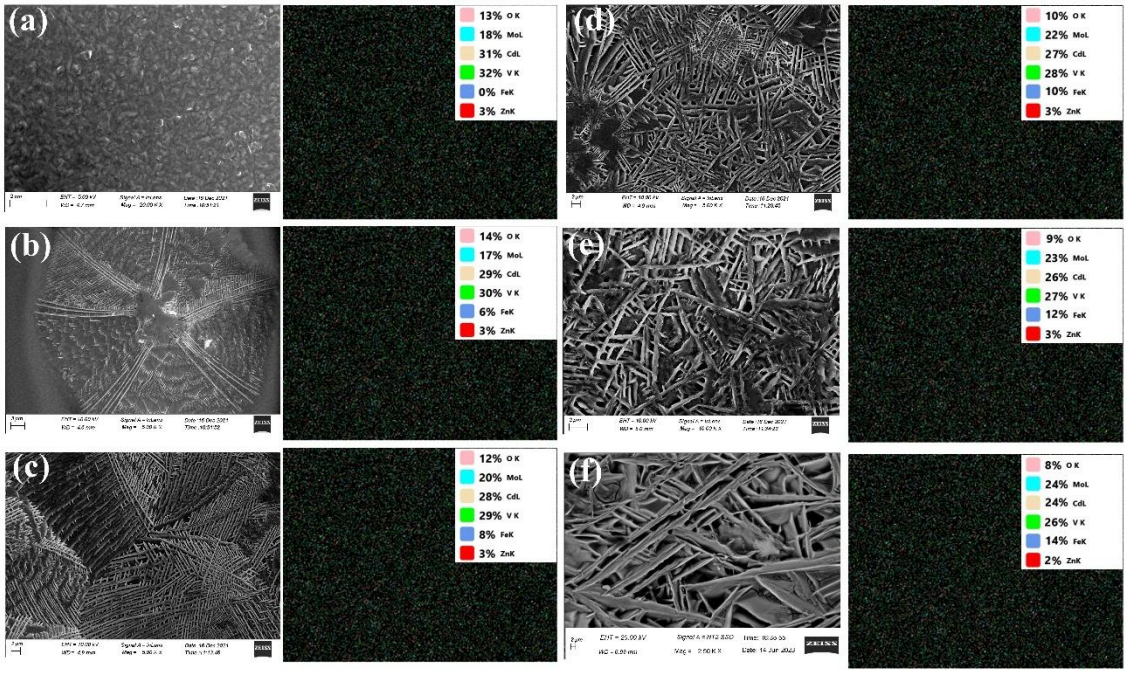

Fig. 4.1.7: FE-SEM micro graphs along with the EDAS mapping images of xFe – (1-x) ($0.3V_2O_5$ – $0.2MoO_3$ – 0.4CdO – 0.1ZnO) glass nanocomposite system with x= (a) 0.0, (b) 0.05, (c) 0.1, (d) 0.2, (e) 0.3 and (f) 0.4.

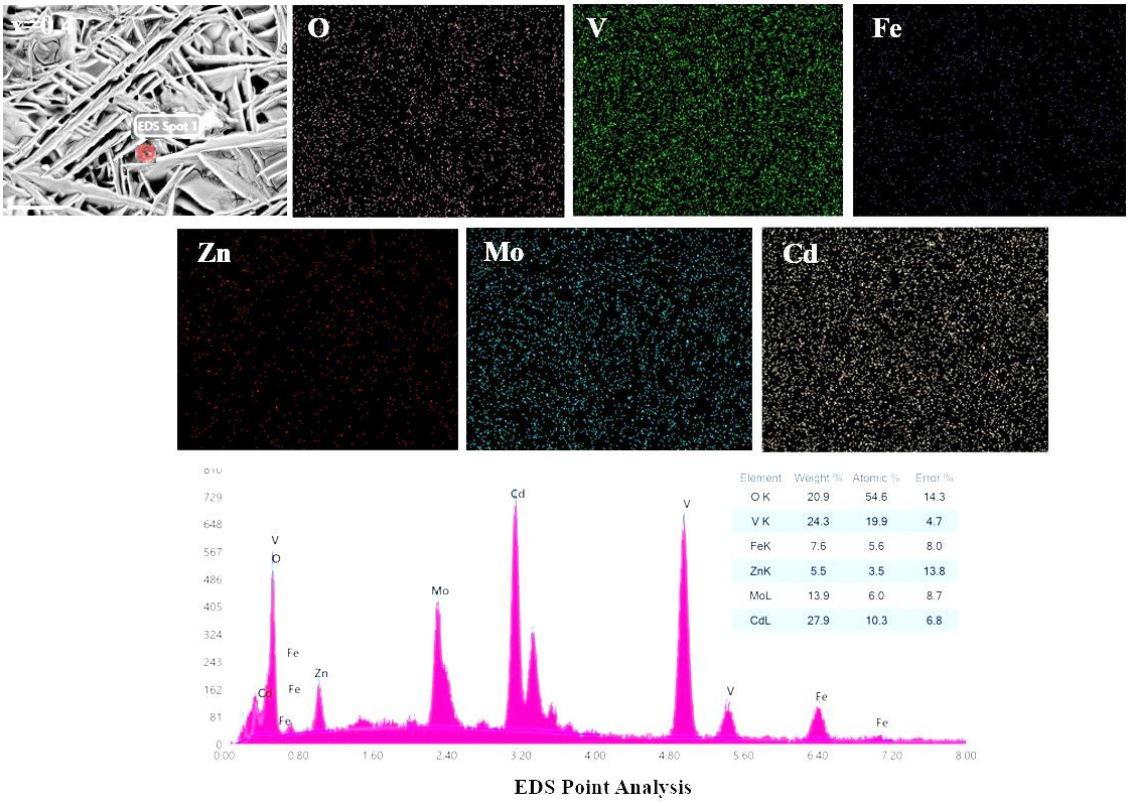

Fig. 4.1.8: EDS elemental mapping of xFe – (1-x) ($0.3V_2O_5$ – $0.2MoO_3$ – 0.4CdO – 0.1ZnO) glass nanocomposite system for x=0.4 sample.

The EDS mapping images used to verify the elements' presence in the glass nanocomposite samples are shown in Fig. 4.1.7: (a-f). The growth of the glass nanocomposite Fe undoped sample (x=0.0) is confirmed by the elemental mapping of the various elements such as Mo, V, Cd, Zn, and O. For other samples (x = 0.05, 0.1, 0.2, 0.3, and 0.4), the presence of the different elements includes Fe, Mo, V, Cd, Zn, and O confirm the growth of quaternary glass nanocomposite. Fig. 4.1.8 shows the EDS elemental mapping of x= 0.4 sample of the present glass nanocomposite system. Fig. 4.1.6 reveals the bulk distribution of Fe, Mo, V, Cd, Zn, and O.

Figure 4.1.9 shows the FE-SEM micro graph for x=0.5 sample of the present glass nanocomposites system. The FESEM image of x=0.5 appears to be high porosity in nature (~75.4% porous). This directly correlates with the decrease in density and decomposition of the initial crystal phases along with all the other phases, as indicated by the XRD results. In view of this, the x=0.5 sample was not considered for further characterization and electrical and mechanical properties analysis.

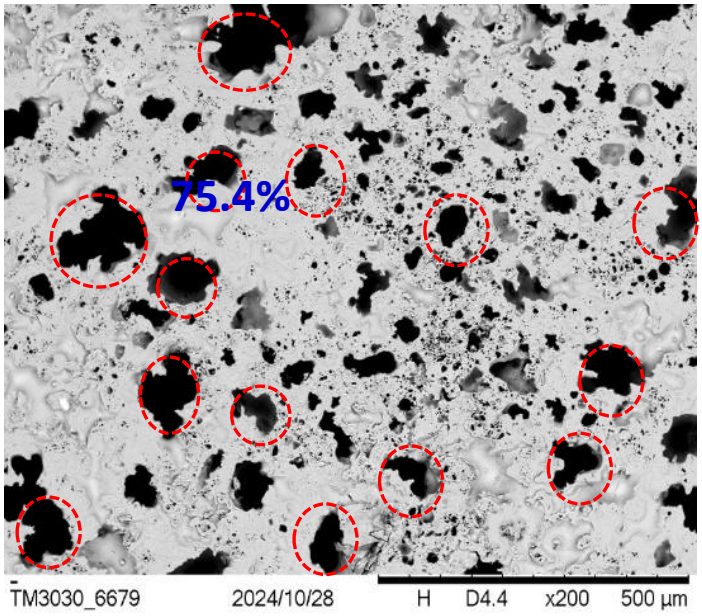

Fig. 4.1.9: FE-SEM micrograph of xFe – (1-x) ($0.3V_2O_5 – 0.2MoO_3 – 0.4CdO – 0.1ZnO$) glass nanocomposites system where x= 0.5.

The effect of heat treatment subjected to different durations (1h, 3h, and 5h) on the developed glass nanocomposites has been investigated. Figures 4.1.8, 4.1.9, and 4.1.10 depicted the correlation between the microstructures of different Fe concentered (x = 0.0, 0.05,

0.1, 0.2, 0.3, and 0.4) glass nanocomposites subjected to under varying heat treatment durations (1h, 3h, and 5h).

Fig. 4.1.10 shows the FE-SEM micrographs of x= 0.0 glass nanocomposite sample at different heat treatment conditions (1h, 3h, and 5h). The irregular pebbles-like nanoparticles were found to be present in the microstructure of the Fe undoped sample (x=0.0) at different heat treatment conditions (1h, 3h, and 5h) shown in Fig. 4.1.10 (a-c). Some of the particles are observed as elongated, regular, and irregular round shapes throughout the glass matrix (fig. 4.1.10(a-c)). The average size of the particles in microstructures has been reduced followed by an increase of heat treatment time (1h to 5h). In 1h heat treatment condition, the microstructure of the glass composite (x=0.0) showed a predominantly crystalline morphology in the glassy matrix. The absence of distinct crystalline phases in the micrographs at 3h and 5h. FE-SEM micrographs also validated the lack of phase segregation at this stage of heat treatment in the x=0.0 sample.

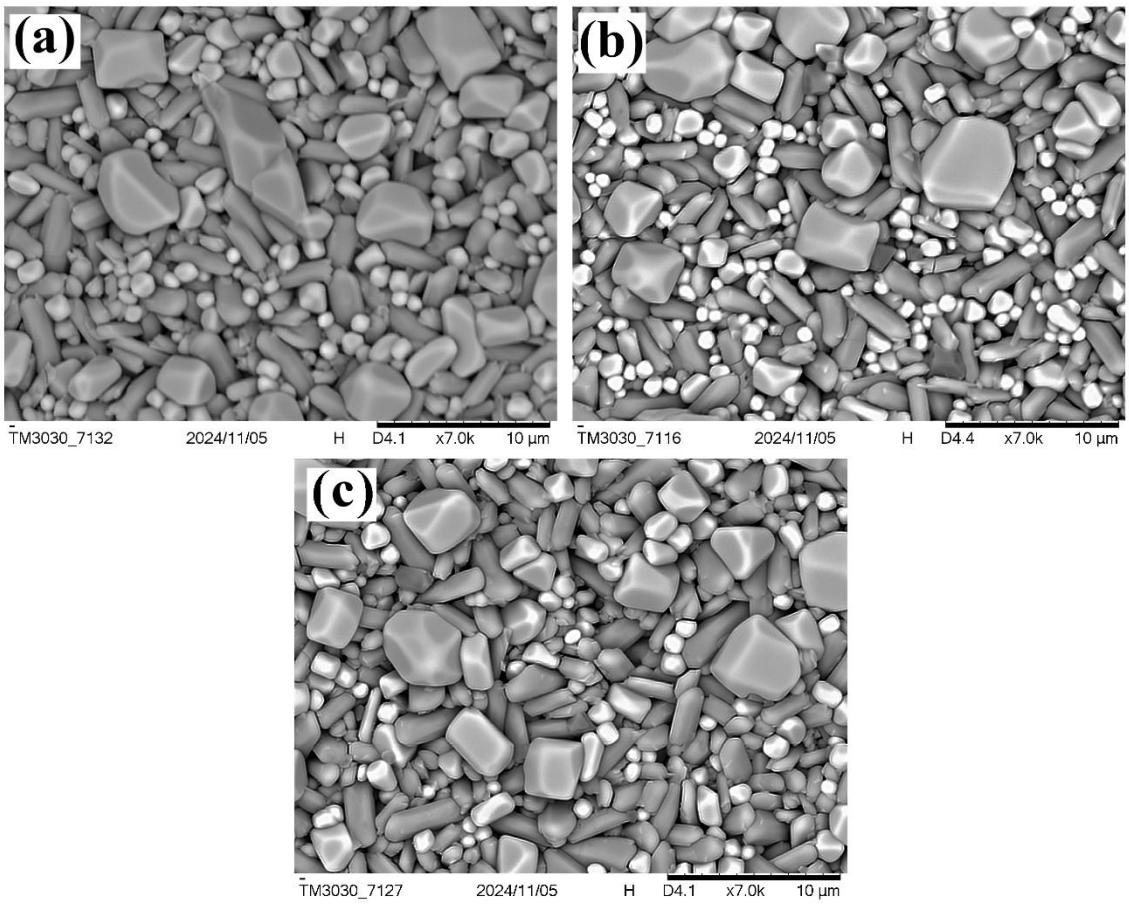

Fig. 4.1.10: FE-SEM micrographs of xFe – (1-x) ($0.3V_2O_5$ – $0.2MoO_3$ – 0.4CdO – 0.1ZnO) glass nanocomposite with values of x is 0.0 at (a) 1h (b) 3h and (c) 5h heat treatment conditions.

Figure 4.1.11 exhibited the correlation between the comparison of FE-SEM micrographs of the present glassy system where, x=0.0, 0.05, 0.1, 0.2, 0.3, and 0.4 at 5h heat treatment conditions. Physical observation of the micrographs reveals that particle size has decreased with the Fe concentration at the same duration of heat treatment (5 h). The size, shape, and variation of particles throughout out microstructure of the samples also decreased from the x=0.0 sample to the x=0.4 sample at the same duration of heat treatment (5 h). The irregular pebbles-like nanoparticles were found to be present in the microstructure of the Fe undoped sample (x=0.0) at 5h heat treatment conditions. Due to increasing the duration of heat treatment in the glassy matrix, the size, shape, and distribution of particles have been changed. Due to the addition of Fe, the irregular pebbles-like particles converted into regular, and irregular round-shaped particles throughout the glass matrix. The addition of Fe disrupted the glass network by dropping the connectivity of the other elements, promoting crystallization [192, 204]. As Fe doping concentration increases from x=0.05 to x=0.4, a noticeable arrangement in the size of the crystals is observed.

Fig. 4.1.12 displays the FE-SEM micrographs of x= 0.4 glass nanocomposite at different heat treatment conditions (1h, 3h, 5h). The regular, and irregular round shapes crystals disperse throughout the all-glass matrix. In sample x=0.4 (1h HT), uniform and dense microstructures have been found. The crystal structures may be developed by the $FeVO_4$ and along with other cadmium and molybdenum-rich crystal phases [42-43]. As the duration of heat treatment increases from 1h to 5h, a noticeable arrangement in the size of the particles is observed. The samples 1h, 3h, and 5h (Figures 4.1.12a–c) display progressively smaller crystals, suggesting enhanced nucleation and growth of crystalline phases due to the presence of Fe. The different crystal phases of ZnV_2O_6, $Zn_3V_2O_8$, $Cd_2V_2O_7$, and $FeVO_4$ were identified by XRD analysis (Details in section 4.1.5 of chapter 4), which corroborates the FE-SEM observations [192,194-198]. The presence of $FeVO_4$ particles in Fe-doped samples further underscores the influence of Fe indicating the crystalline phase composition [199-201]. These iron vanadium oxide crystallites coexist with cadmium and molybdenum-rich phases, suggesting a multi-phase microstructure that evolves with Fe doping. Despite the variation in crystal sizes, the overall distribution of crystals remains relatively uniform across the samples (x=0.4) at different durations of heat treatment (1h, 3h, and 5h).

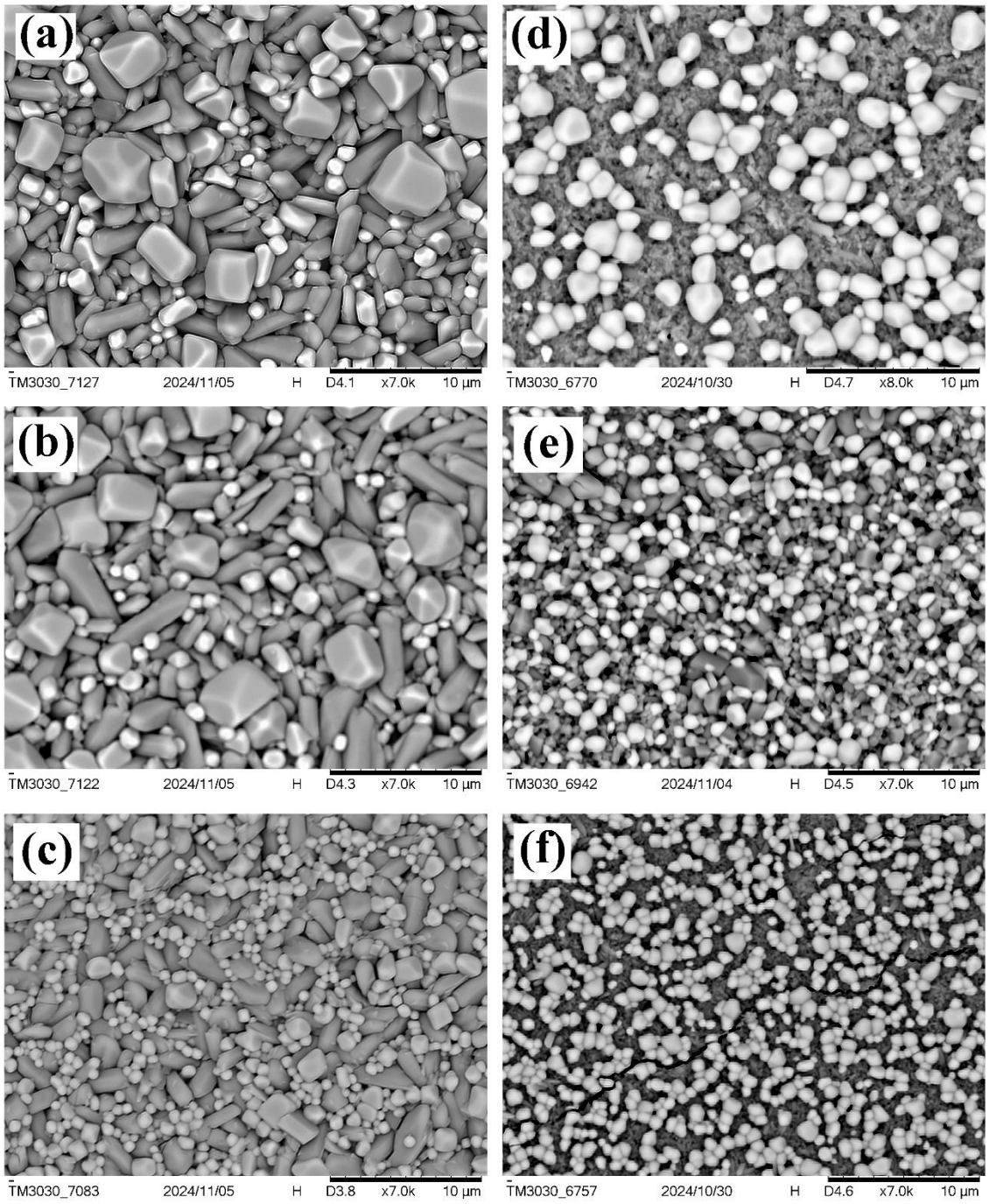

Fig. 4.1.11: FE-SEM micrographs of xFe – (1-x) $(0.3V_2O_5 – 0.2MoO_3 – 0.4CdO – 0.1ZnO)$ glass nanocomposite with x= (a) 0.0, (b) 0.05, (c) 0.1, (d) 0.2, (e) 0.3 and (f) 0.4 at 5h heat treatment condition.

The EDS mapping images used to confirm the presence of elements in the glass nanocomposite sample (x=0.0) after a 5-hour heat treatment are shown in Fig. 4.1.13. The color mapping clearly verifies the presence of Mo, V, Cd, Zn, and O, confirming the formation of the Fe-undoped glass nanocomposite (x=0.0). The EDS point analysis graph in

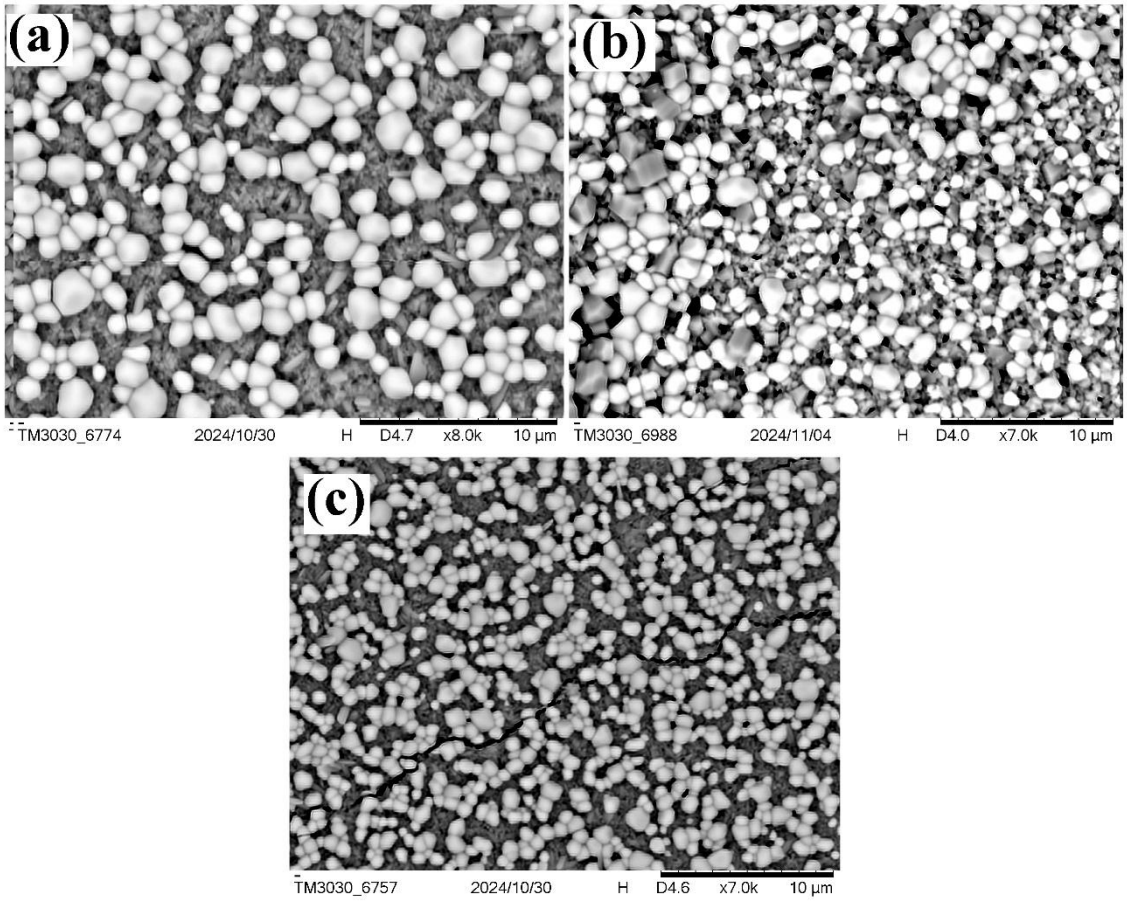

Fig. 4.1.12: FE-SEM micrographs of xFe – (1-x) $(0.3V_2O_5 – 0.2MoO_3 – 0.4CdO – 0.1ZnO)$ where, x= 0.4 glass nanocomposite at different heat treatment condition (a) 1h (b) 3h, and (c) 5h.

Fig. 4.1.13 distinctly shows peaks corresponding to V, Cd, O, Mo, and Zn. Figure 4.1.14 presents the EDS elemental mapping for the glass nanocomposite sample with x=0.4 after a 5h heat treatment. The mapping illustrates the uniform distribution of Fe, Mo, V, Cd, Zn, and O, confirming the presence of Fe in the x=0.4 glass nanocomposite [204]. Additionally, the EDS point analysis graph in Fig. 4.1.14 clearly displays peaks for V, Cd, O, Mo, and Zn, along with Fe peaks.

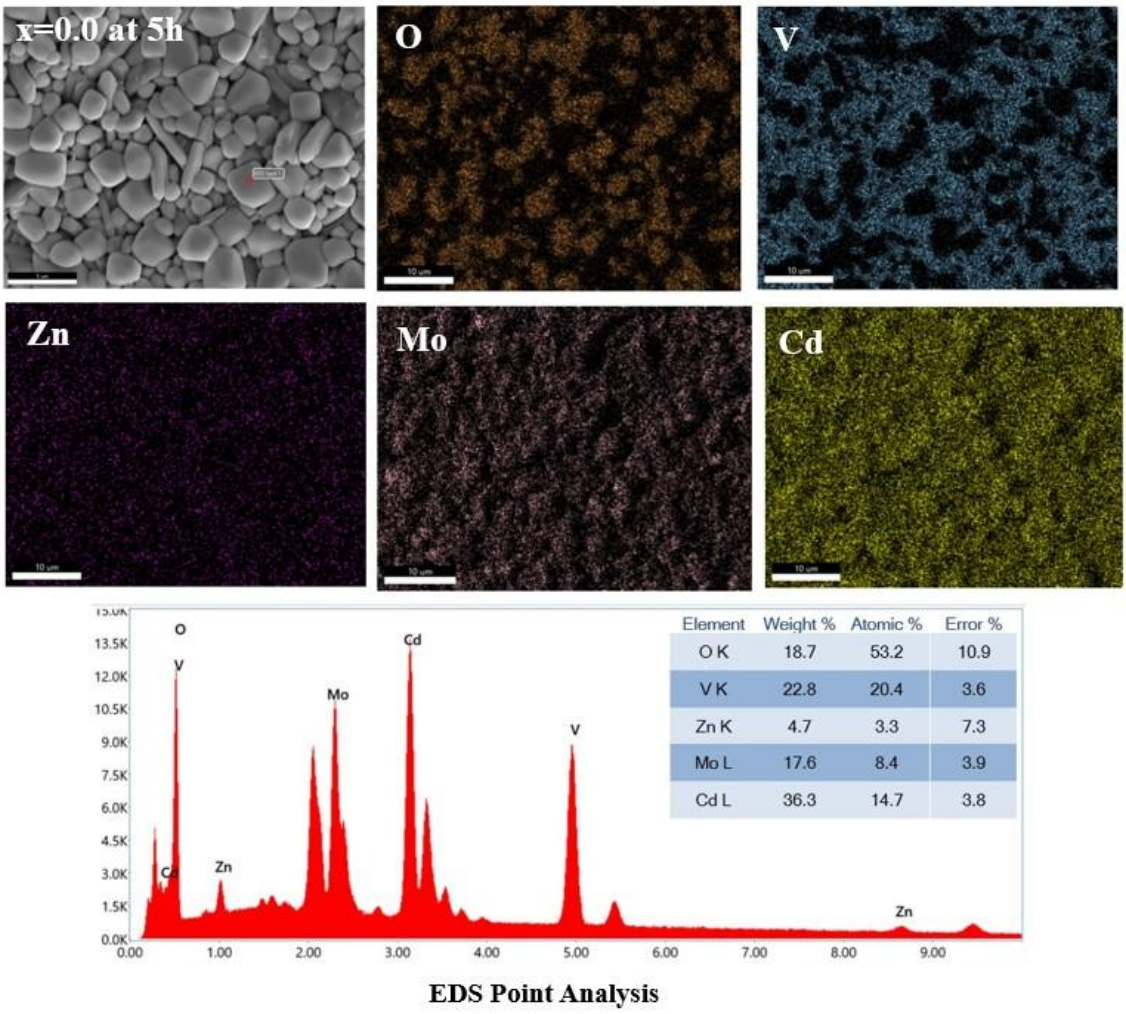

Fig. 4.1.13: EDS elemental mapping of xFe – (1-x) ($0.3V_2O_5$ – $0.2MoO_3$ – 0.4CdO – 0.1ZnO) glass nanocomposite system for x=0.0 sample at 5h heat treatment condition.

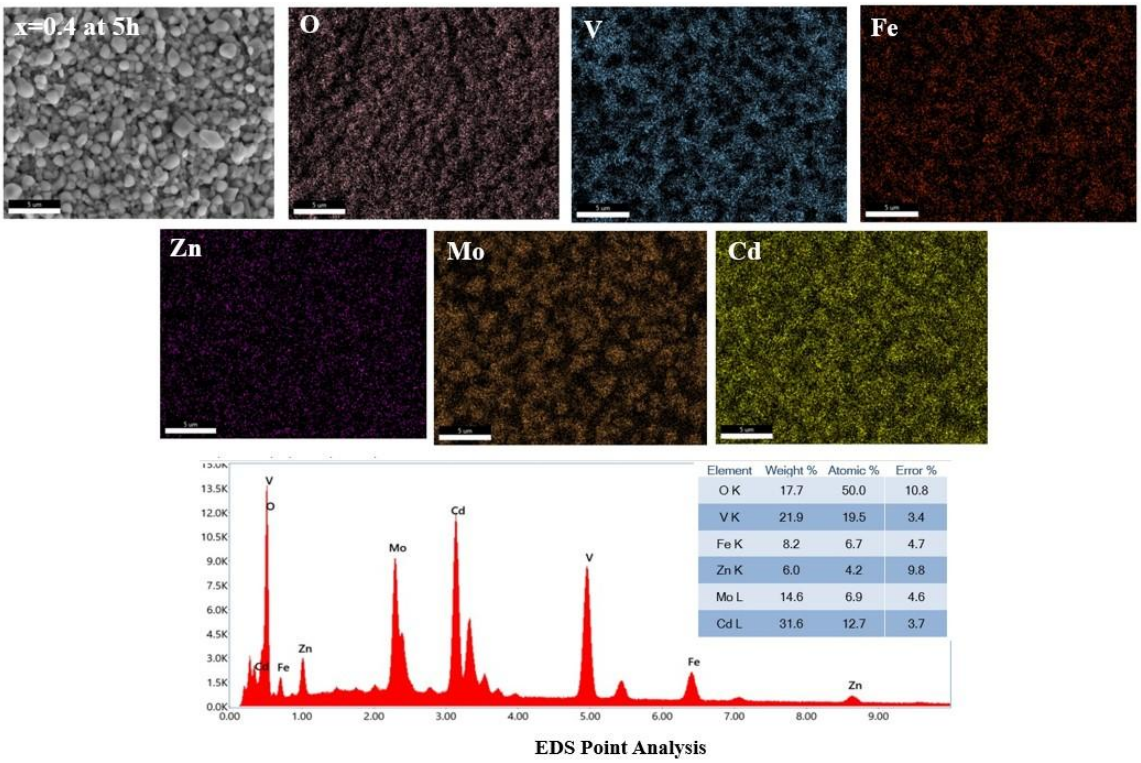

Fig. 4.1.14: EDS elemental mapping of xFe – (1-x) ($0.3V_2O_5$ – $0.2MoO_3$ – 0.4CdO – 0.1ZnO) glass nanocomposite system for x=0.4 sample at 5h heat treatment condition.

4.1.7 Conclusion

This section explores various physical and structural properties using techniques such as density and molar volume measurement, FTIR, DSC, XRD, FESEM, and EDS analysis. The density in the present study increases as Fe concentration increases, while V_2O_5 modifies the glass network and increases its compactness. Changes in density and molecular weight determine molar volume changes. The molar volume also increases with an increase in Fe (x), along with molecular weight and density. FTIR analysis reveals that the higher Fe concentrations should result in lower energy requirements to vibrate the Zn-O and V-O bands. This result leads us to infer that the present glass system with a higher Fe content is unstable due to acoustic phonon vibrations. This conclusion is supported by XRD analysis results that show an increase in the average dislocation density and a decrease in structure stability with increasing Fe content. In DSC analysis, glass transition temperature (Tg) has been evaluated and correlated with the different Fe concentrations. Different crystal phases have been developed, which were identified through XRD analysis. The crystal phases of zinc vanadium oxide (ZnV_2O_6), $Zn_2V_2O_7$, and $Zn_3V_2O_8$ are observed as major phases in all prepared samples as well as heat-treated samples (x=0.4). The peak intensity of $Zn_3V_2O_8$ is higher in the x=0.4

sample than in other samples. Characteristic peaks of cadmium vanadium oxide ($Cd_2V_2O_7$) and vanadium molybdenum oxide (V_2MoO_8) appear in all prepared samples. The Debye–Scherrer equation has been used to estimate the average crystallite sizes, microstrain, and also dislocation density has been estimated. The heat-treated sample withx=0.4 shows an increase in the intensity of peaks corresponding to iron vanadium oxide ($FeVO_4$) under various heat treatment durations (1 h, 3 h, and 5 h). Additionally, crystal phases of zinc vanadium oxide ($Zn_3V_2O_8$) are observed in the same sample (x=0.4) after 5 h of heat treatment, with their intensity being higher compared to the untreated sample (x=0.4). FE-SEM has been used to examine the morphologies of the glass samples (x=0.0, 0.05, 0.1, 0.2, 0.3, and 0.4) along with various heat treatment conditions (1h, 3h, and 5h). The plate-like crystals have been observed in the microstructure in the Fe undoped sample (x=0.0). The plate-like crystals disperse throughout the glass matrix. In sample x=0.05, uniform and dense microstructures have been found where the dendrite structure crystal develops. Micrographs reveal that particle size has decreased with the Fe concentration. The size, shape, and variation of particles within the microstructure of the samples decreased as the composition changed from x=0.0 to x=0.4 under the same heat treatment duration (5 h). For the x=0.4 sample, the variation in crystal sizes and the overall distribution of crystals remains relatively uniform across different heat treatment durations (1 h, 3 h, and 5 h). The mapping reveals a uniform distribution of Fe, Mo, V, Cd, Zn, and O, confirming the presence of Fe in both the as-prepared samples and those subjected to 5 h of heat treatment. Furthermore, the EDS point analysis graphs clearly display peaks corresponding to V, Cd, O, Mo, and Zn, along with Fe peaks, in both the heat-treated and untreated samples.

4.2 Electrical Properties of Fe-V_2O_5-MoO_3-CdO-ZnO Glass Nanocomposite System

4.2.1 Introduction

In recent years, researchers have given much concentration to nanoglass semiconductor materials due to their excellent electrical, structural, and optical properties. Researchers had previously reported that nanoglassy transition metal oxide (TMO) composites exhibit semiconducting properties [1–4]. Many applications of these TMO glass nanocomposites have drawn increased attention, like switching, electro-optical devices, and optical and memory switching devices [7-11].

On the contrary transition metal ions are the appropriate cause of electrical conduction in the semiconducting nanocomposite glasses [106]. The process of conduction takes place because of the hopping phenomenon of an electron. It happens between ions that belong to the same transition metal but in various valence states dedicated to electronic conductivity [205-206]. There are several factors on which the oxide's glass electronic conductivity depends such as glass melting temperature, distance among the ions of transition metal, etc [206].

Different researchers have explored the electrical conductivity (both AC and DC) of glassy nanocomposites due to their semiconducting behavior as well as technological uses in modern civilization [26-30].

In this study, the AC as well as DC analysis of the present nano glassy system have been attempted to attain the knowledge relating to the electrical properties of these systems.

4.2.2 DC Conductivity

In the current study, the density of defect states inside the mobility gap may be taken into account when predicting the DC conductivity of amorphous semiconductors [22, 99]. The DC conductivity of the present system is temperature- sensitive, as shown in Fig. 4.2.1. Further, it also states the thermally activated nature [22, 99-100, 192, 207]. It can be seen that DC electrical conductivity is proportional to the reciprocal of temperature. A uniform conductivity is seen in all the samples held as the reciprocal of temperature.

The activation energies (E_σ) of DC conductivity (σ_{dc}) were calculated by approximating the temperature dependence of conductivity with the Arrhenius equation:

$$\sigma_{dc} = \sigma_0 \exp\left(-\frac{E_\sigma}{k_B T}\right) \qquad (4.2.1)$$

Where, σ_0 = pre-exponential factor, k_B = Boltzmann constant, T = absolute temperature

The DC activation energy (E_σ) was estimated from the slopes of the straight-line fits using the relation.

Activation energy (E_σ) = slop of log σ_{dc}vs. 1000/T curve × 0.198

This conveys the information that the temperature is dependent on activation energy and is symptomatic of the hopping conduction shown by the little polaron. DC conductivity also shows increasing characteristics with the enhanced temperature, which represents the semiconducting nature.

Table 4.2.1: The values of activation energy against the concentration of Fe (x)

Concentration of Fe (x)	**slope**	**Activation Energy (E_σ)**
0.0	5.327	1.054
0.05	3.249	0.643
0.1	2.846	0.563
0.2	2.687	0.532
0.3	2.445	0.484
0.4	2.263	0.448

A V_2O_5nanostructured glass sample [192] has DC conductivity values that agree well with those in Fig. 4.2.1. This semiconducting behaviour is seen in Fig. 4.2.1, which shows an increasing DC conductivity as temperature increases.

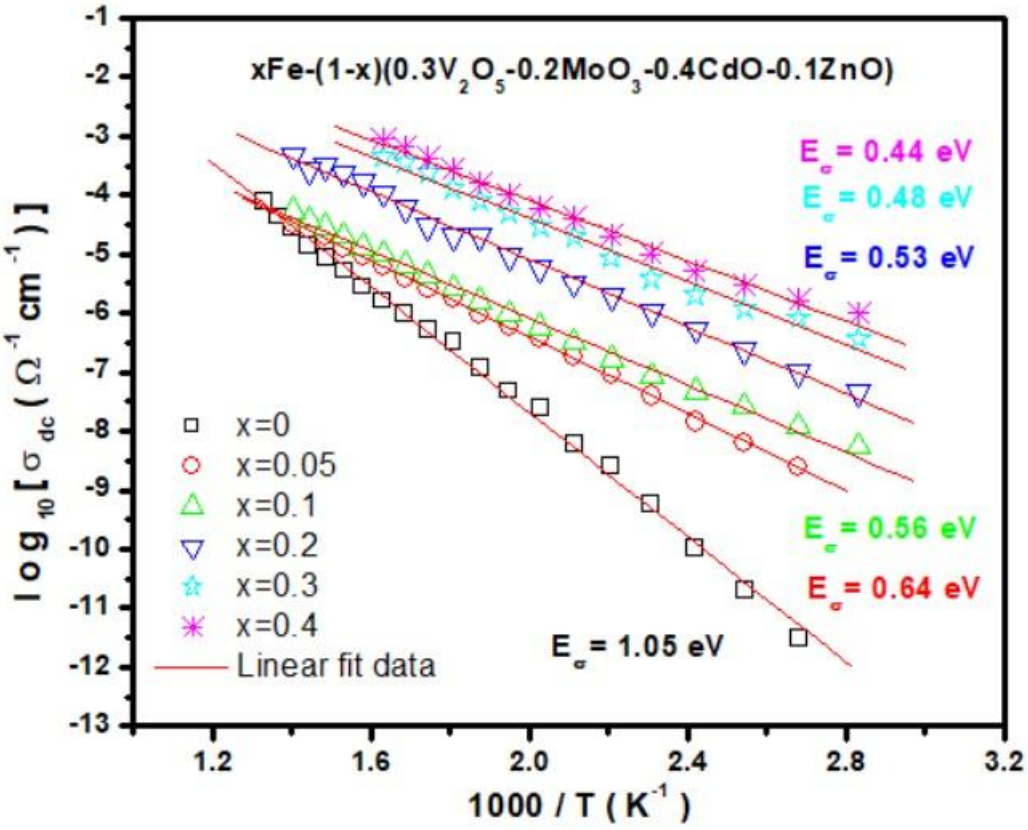

Fig. 4.2.1: Temperature dependence of DC conductivity of xFe – (1-x) ($0.3V_2O_5$ – $0.2MoO_3$ – 0.4CdO – 0.1ZnO) glass nanocomposite with various values of x.

Figure 4.2.1 shows the DC conductivity data, which is best fitted with straight lines. The slope of straight-line fits is used to calculate the DC activation energy. The activation energies are found to be 1.05, 0.64, 0.56, 0.53, 0.48, and 0.44 eV, when x =0.0,0.05, 0.1, 0.2, 0.3, and 0.4, respectively. Such a kind of demeanor of the conductivity of DC and the activation energy should have a relationship with the structural modifications and is found with the incorporation of Fe, and this is depicted in Fig. 4.2.2 [192]. Further, the reports indicate that to make a vibration in the Mo-O and Zn-O bands, minimal energy is required so that an acoustic phonon contribution is induced when the Fe content increases. When the concentration of Fe doping increases, the DC conductivity also rises. So the total information derived is that to synthesize a steady occurrence of little polarons so that the DC conductivity will improve, the dedication of photons to produce some regional states within the optical band gap is desired. This says that both photons and phonons helped in the conduction process, which took place with the contribution of small polarons [192].

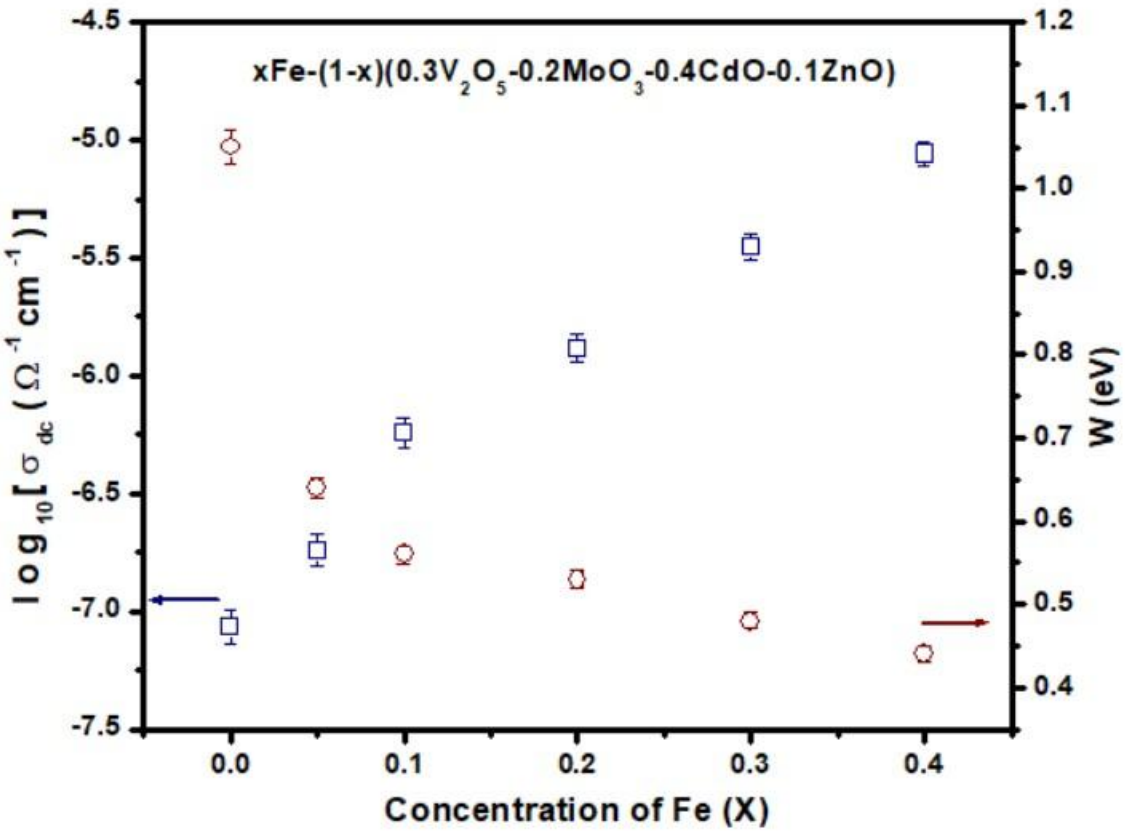

.

Fig. 4.2.2: Variation of DC conductivity, σ_{dc} at 513 K, and activation energy E_{σ}(ev) corresponding to Composition (x).

The components of all samples, such as capacitance, conductance, and dielectric loss tangent, were predicted using an automatic high-accuracy LCR meter. This is done at different temperatures and frequencies, ranging from 42 Hz to 5 MHz.It is possible to connect an external voltage to the current flowing through a sample using an AC response. The parallel RC circuit, which stands for a resistance-capacitance circuit, is a comparable circuit that combines two components, ideal resistive and reactive. The equation can be made as follows [208]:

$$\frac{1}{Z} = \frac{1}{Z_R} + \frac{1}{Z_C} \qquad (4.2.2.)$$

$$= \left(\frac{1}{R} + j\,\omega\,C\right)^{-1}$$

$$= \frac{R}{1 + j\omega\,RC}$$

$$= \frac{R}{1+(\omega RC)^2} - j\,\frac{\omega R^2 C}{1+(\omega RC)^2} \qquad (4.2.3)$$

Where, Z_R = Resistive component, Z_C = Reactive component

At high frequencies, the RC circuit acts as a capacitor, and in other ways, at low frequencies, it takes part as a resistor [209].

$$\left(Z_{re} - \frac{R}{2}\right)^2 + Z_{im}^2 = \left(\frac{R}{2}\right)^2 \quad (4.2.4)$$

The real impedance (Z_{re}) along with imaginary impedance (Z_{im}) can be to a greater extent by the above Eq. (4.2.4) [208]. It is shown by the graphs of complex impedance that equation (4.2.4) is a semi-circle in the plane of the complex.

From the Cole-Cole plot of resistivity (Fig. 4.2.3(a-f)), the DC resistance R was determined at different temperatures, and then DC conductivity was computed for the samples using the relationship:

$$\sigma = \frac{1}{R} \times \frac{t}{A} \quad (4.2.5)$$

Where, t = Thickness of the sample, A= cross-sectional area of the sample, R = Resistance of the glassy sample

Figure 4.2.3 (a-f) displays semi-circular arcs at different pinpoint temperatures and graphs for complex impedance at different temperatures when for all samples (x=0.0 to 0.4). Due to the wide impedance between the Fe undoped sample (x=0.0) and Fe high concentrated sample (x=0.4), it is not possible to compare between these samples (x=0.0 to 0.4) in a single graph. It has been divided into two plots (Fig. 4.2.4 a and b). Cole-Cole plot of resistivity of the system at different temperatures for x = 0.0, 0.05, and 0.1 at 533 K depicted in Figure 4.2.4 (a). The Fig. 4.2.4 (b) displays the Cole-Cole plot of resistivity for x = 0.2, 0.3, and 0.4 at same temperature. From Fig. 4.2.4 (a) and (b), it is clear that for a particular temperature at 533K where the semi-circular arc's radius is maximum for x=0.0 sample and semi-circular arc is minimum for the x=0.4 sample. Materials consisting of a single or many more relaxation processes but with the same magnitude find the Cole-Cole plot to be a very useful tool. The storage component of the dielectric is related to dielectric loss. At the same time, a semicircle is formed therefore pointing to the existence of relaxation time of a single nature [83, 193].

The glassy system's relaxation process is estimated using the essential condition of $\omega_{max} \times \tau = 1$, where τ is the relaxation time of Debye-type relaxation [83,210]. The values of ω_{max} are computed from the frequency dependence of Z´´plot. Fig. 4.2.5 shows the frequency

dependence of Z´´ plot at various temperatures of a system, where x = 0.0 to 0.4. Figure 4.2.6 (a) illustrates the temperature dependence of the relaxation time (τ) for all glassy samples, which demonstrates the thermally activated behaviour of τ. In Fig. 4.2.6 (a), the values of τ are found to decrease with increasing temperature, which specifies the semiconducting nature. Figure 4.2.6 (a) is also clear that the relaxation time (τ) decreases with raising the concentration Fe. Which is validated by conductivity data [83, 210].

The theoretical relaxation time is determined with the help of the following Eq. 4.2.6.

$$\tau = \tau_0 exp\left(-\frac{E_\tau}{k_B T}\right) \quad (4.2.6)$$

in which,

τ_0 = pre-exponential factor

K_B = Boltzmann constant

T = absolute temperature.

The activation energy (E_τ) linking the relaxation process is determined from the slopes. This slope is for the straight lines which are best-fitted as depicted in Fig. 4.2.6 (a) and estimated values of activation energy (E_τ) have been presented in table 4.2.2. In Fig. 4.2.6 (b), relaxation time (τ) when the fixed temperature is 533 K and related to composition, x has been incorporated. It has been seen that the relaxation time (τ) and activation energy (E_τ) have been minimized with increasing the concentration of Fe. That is validated by the conductivity data [210-211].

The low region of low frequency bearing value of conductivity which is much less than is at the ultimate end indicates phase angles as zero. Further, in the less frequency region, the gathering of charge carriers known as electrode polarization takes place as a result of the steady but periodic retroversion of the electric field, and this is reduced as the frequency is larger. For all prepared samples, shifting in the high-frequency area is found in

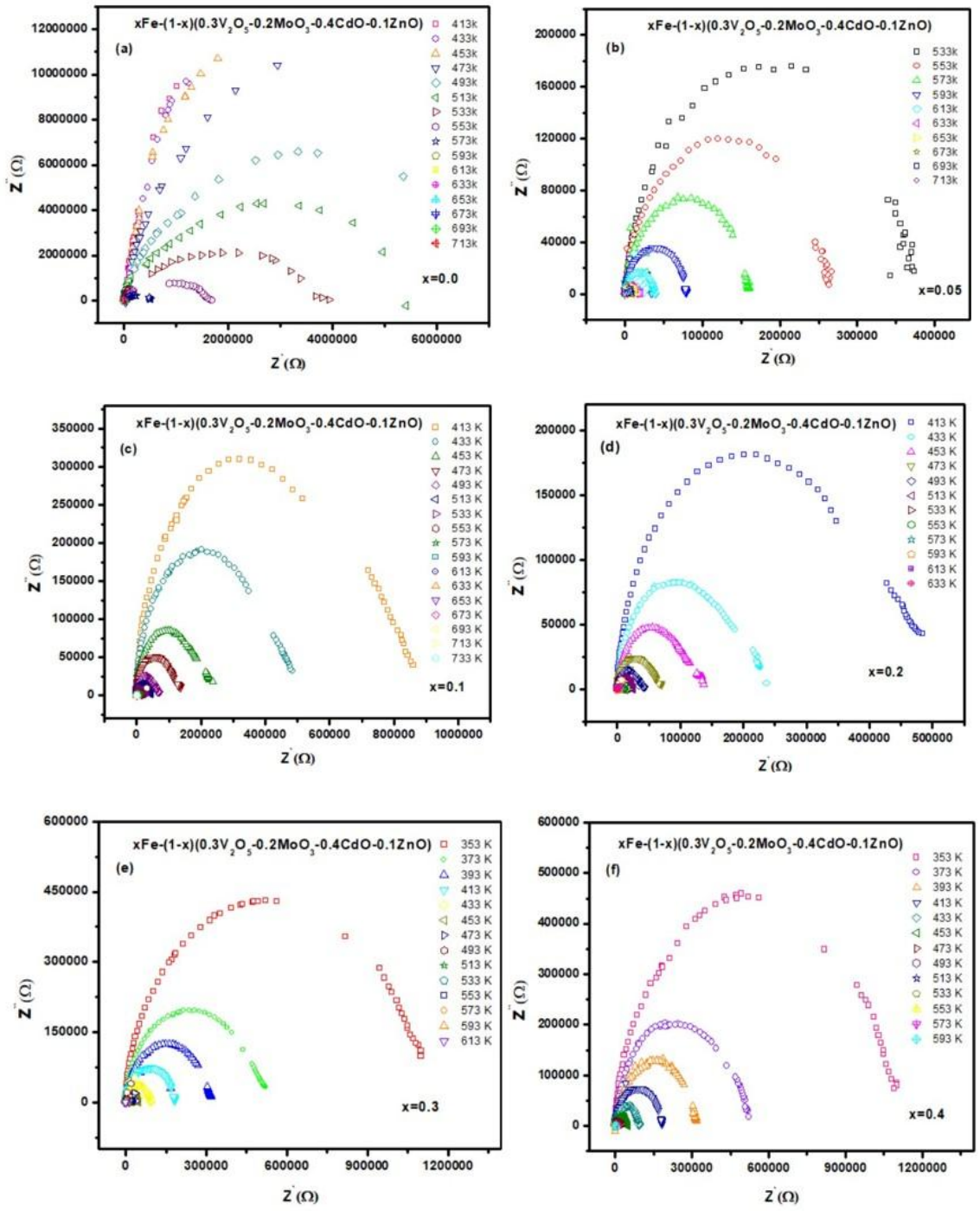

Figure 4.2.3: (a-f) Cole-Cole plot of resistivity of the glass nanocomposites xFe – (1-x) ($0.3V_2O_5$ – $0.2MoO_3$ – 0.4CdO – 0.1ZnO) with x= (a) 0.0, (b) 0.05, (c) 0.1, (d) 0.2, (e) 0.3 and (f) 0.4.

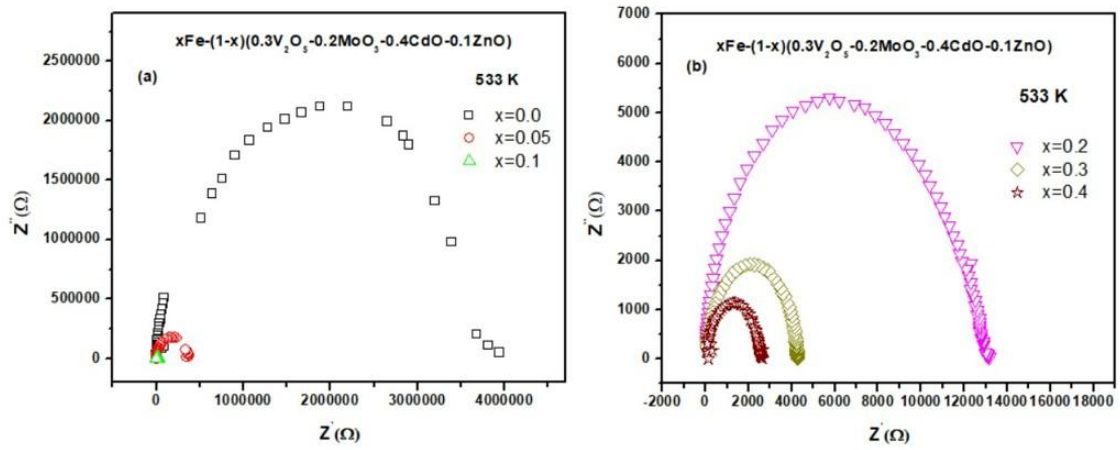

Figure 4.2.4: (a) Cole-Cole plot of resistivity of the present system for sample x = 0.0, 0.05, and 0.1 at 533 K**.** (b) Cole-Cole plot of resistivity of the present system for sample x = 0.2, 0.3, and 0.4 at 533 K**.**

two zones of moderate and larger frequency. The hope process of the polaron takes place in the lower frequency region and it is shown in the above-said discussion. Frequency reliable character can be confirmed from the spectra of frequency response conductivity.

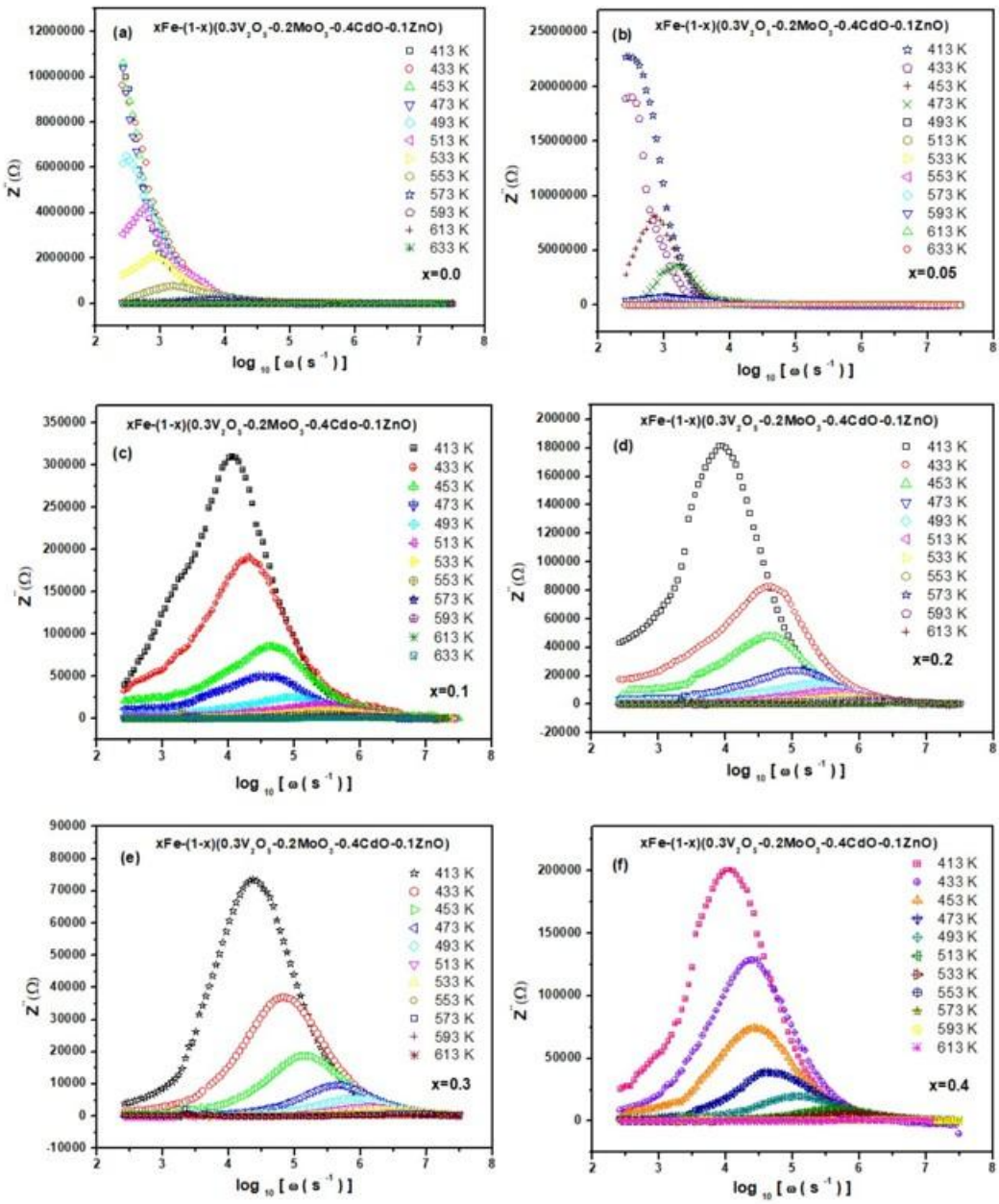

Fig. 4.2.5: Frequency dependence of $Z^{//}$ at various temperatures of xFe – (1-x) ($0.3V_2O_5$ – $0.2MoO_3$ – 0.4CdO – 0.1ZnO) glass nanocomposites system with x= (a) 0.0, (b) 0.05, (c) 0.1, (d) 0.2, (e) 0.3 and (f) 0.4.

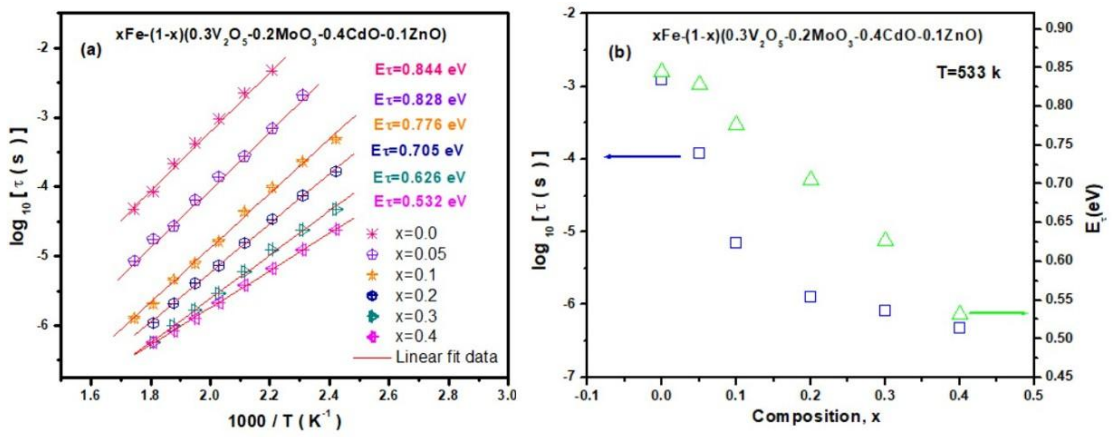

Fig. 4.2.6: (a) Relaxation time (τ) with 1000/T of the glass nanocomposites xFe – (1-x) ($0.3V_2O_5$ – $0.2MoO_3$ – 0.4CdO – 0.1ZnO) for different x values (b) Variation of relaxation time (τ) at 533 K and activation energy (E_τ) corresponding to composition, x.

Table 4.2.2: The values of activation energy (E_τ) associated with the relaxation process against the concentration of Fe (x).

Sl No.	Concentration of Fe (x)	Activation Energy (E_τ)
1	0.0	0.844
2	0.05	0.828
3	0.1	0.776
4	0.2	0.705
5	0.3	0.626
6	0.4	0.532

4.2.3 AC conductivity

4.2.3.1. Power law

The conductivity spectra under the region of more frequency for different temperatures for all samples are seen in Figs.7(a-f). There is an obvious increase in AC conductivity as the temperature rises, which indicates a thermally activated system.

Conductance was measured using a Hioki-made automatic high-precision LCR meter (Model No. 3532- 50) in the frequency window 42 Hz to 5 MHz at various temperatures.

The AC conductivity was carried out using the following Eq. 4.2.7.

$$\sigma_{ac} = \frac{t}{A} \times G \qquad (4.2.7)$$

Where, t = Thickness of the sample, A = sample's Cross-sectional, G= Conductance

Jonscher's universal power law [29] can be used to determine the AC conductivity of semiconductors that are amorphous in nature.

$$\sigma(\omega) = \sigma'_0 + A\omega^S \qquad (4.2.8)$$

Where, σ'_0= low-frequency conductivity, A = coefficient, S = frequency exponent.

The value of S is found by best linearly fitting the data in Figs. 4.2.7 (a-f). The slope of the line which is best fitted gives the number in terms of value for S.

With the help of suitable conduction models, the data on AC conductivity can be explained. Conduction models like QMT, CBH HOB, NSPT, etc. are deployed by a whole-number of researchers in this field [83, 209]. S vs T plot [Figs. 4.2.8 (a-f)] when the value of x is 0.0, 0.05, 0.1, 0.2, 0.3, and 0.4. Several research works have been conducted to enlighten the conduction process. Figures Figs. 4.2.8 (a-f) shows that when temperature rises, the value of S decreases, and this holds for all x values. Electrical conduction can be predicted by the variation of S corresponding to temperature. The modified CBH model is used to state the nature of S as it relates to temperature in the system and the predominant conduction technique in the current system [212]. Fig. 4.2.8 (a) displays a concave downward nature, while Figs. 4.2.8 (b-f) are noticed to be showing concave behavior in an upward direction. Lattice disfigurement could extend to many lattices of space and as a result, polaron hopping of a larger nature may occur with zero Fe concentration for the system, depicted in Fig. 4.2.8 (a) [192]. When Fe is doped simultaneously, there will be some restriction in the lattice distortion to the side by ions which leads to a hopping phenomenon consisting of small polaron in the current system [192]. XRD result shows that on the evolvement of different nano phases, structural modification should emerge. This limited lattice distortion results from the structural arrangement in the current system when Fe concentration is adjoined. When the current system is steadily increased with Fe, this type of environment charges a conversion of conduction technique from large to small hoping polaron [6, 212]. Electrical conductivity is increased side by side with compositions. Little polaron transit needs polarons hopping within the neighboring region [6, 212]. The S-T

curve depicts the behaviour of concave in the upward direction and is shown in Figure Figs. 4.2.8 (b-f).

The frequency exponent (S), can be written out using the CBH model as [212]:

$$S = 1 - \frac{6\,K_B\,T}{W_m + K_B T * \ln(\omega\,\tau_0)} \qquad (4.2.9)$$

Where, K_B= Boltzmann constant, T= absolute temperature,W_M=maximum barrier height and τ_0 = relaxation time

The equation CBH is slightly modified to obtain clear and accurate fitted graphs and is given by:

$$S = 1 - \frac{6\,K_B\,(T - T_0)}{W_m + K_B(T - T_0) * \ln(\omega\,\tau_0)} \qquad (4.2.10)$$

Where, T_0 = dimension of temperature.

The modified nature of the CBH model recognizes the meaning of T_0 in the physical sense [6, 83, 212]. It may be said that the transition temperature of glass is the ideal basis in the field of thermodynamics. This is because the conductivity pre-factor and the different hopping time behaviour must find an association with the free activation energy in the entropy part [6, 83, 212]. In the CBH modification model, the ideal transition temperature (T0) is derived from the temperature T. This can write the AC conductivity related to the CBH model as

$$\sigma_{ac} = n^{/}\pi^3[N(E_F)]^2\varepsilon\varepsilon_0\omega R^6_{H\omega}/24 \qquad (4.2.11)$$

Where, $N(E_F)$= concentration or intentness of pair conditions, $R_{H\omega}$= hopping distance at ω, and $n^{/}$= polarons number take part in the process of hopping

Table 4.2.3 shows the amount of W_m, τ_o, and T_0. This is evaluated from S and temperature graphs which are shown in Fig. 4.2.8 (a-f) with the new CBH model utilizing equation (4.2.10).

Further, it conveys the fact that W_m shows a reduction with the rise of x in the system. The XRD analysis represents the variation of dislocation densities, lattice strain and it shows to increase with the addition of the concentration of iron in the glass system along with the decrease of stability of structural on account of the formation of localized defects [212, 213]. It is also found from the analysis of conductivity (electrical) that the energy of activation corresponding to the conductivity of DC is reduced with the enhancement of the addition of iron content, which is presented in Fig. 4.2.2 [6, 213]. The behaviour of activation energy indicates the imbalance in the current system caused by doping the iron concentration. FTIR

study shows that the vibration of Zn-O and Mo-O bands take lower energy in the higher concentration of Fe containing batches, which is significantly affect the acoustic phonon vibrations. Therefore, the system in use containing more Fe amount shows the more unstable with higher acoustic vibration [192].

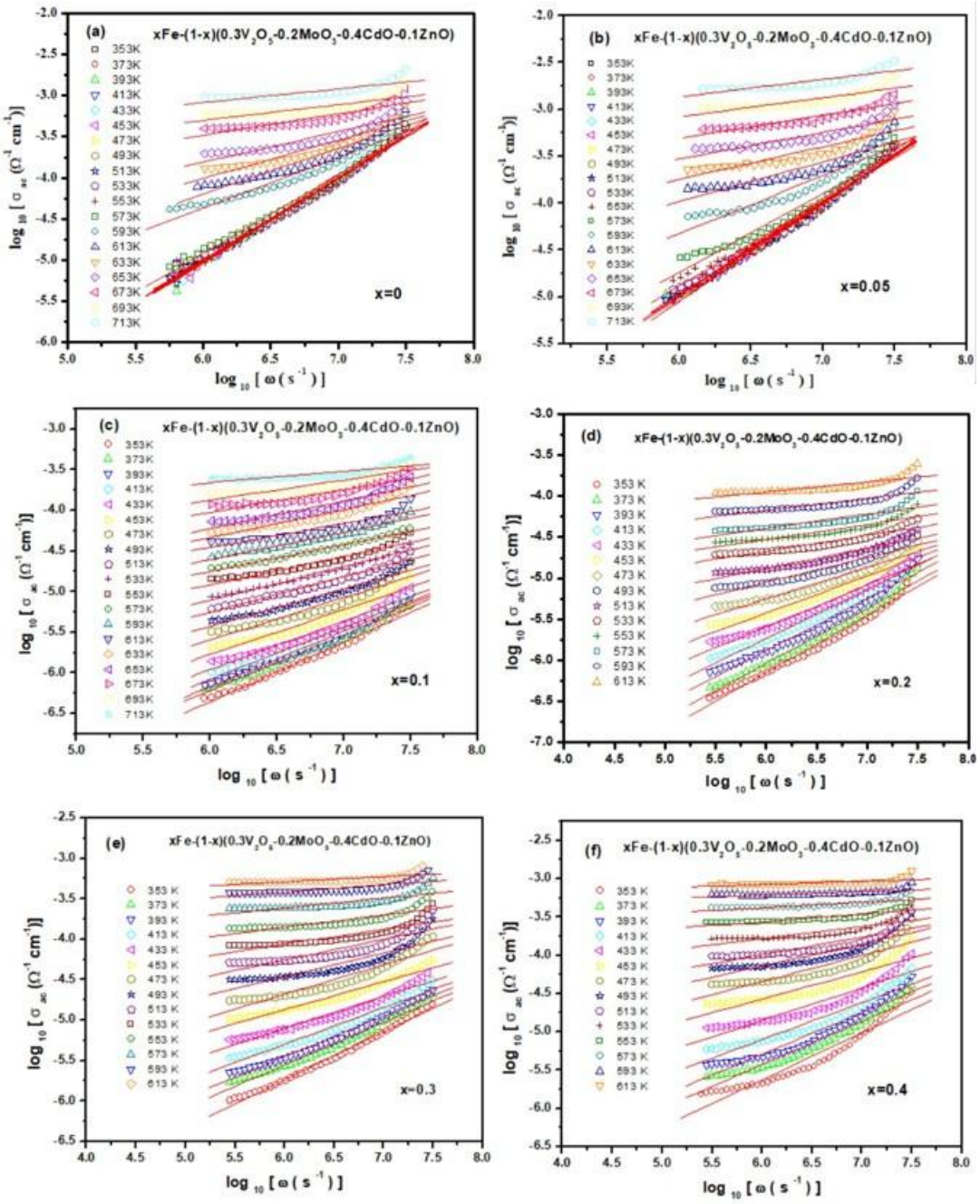

Fig. 4.2.7: High-frequency AC conductivity spectra for xFe – (1-x) ($0.3V_2O_5$ – $0.2MoO_3$ – 0.4CdO – 0.1ZnO) glass system with x= (a) 0.0, (b) 0.05, (c) 0.1, (d) 0.2, (e) 0.3 and (f) 0.4.

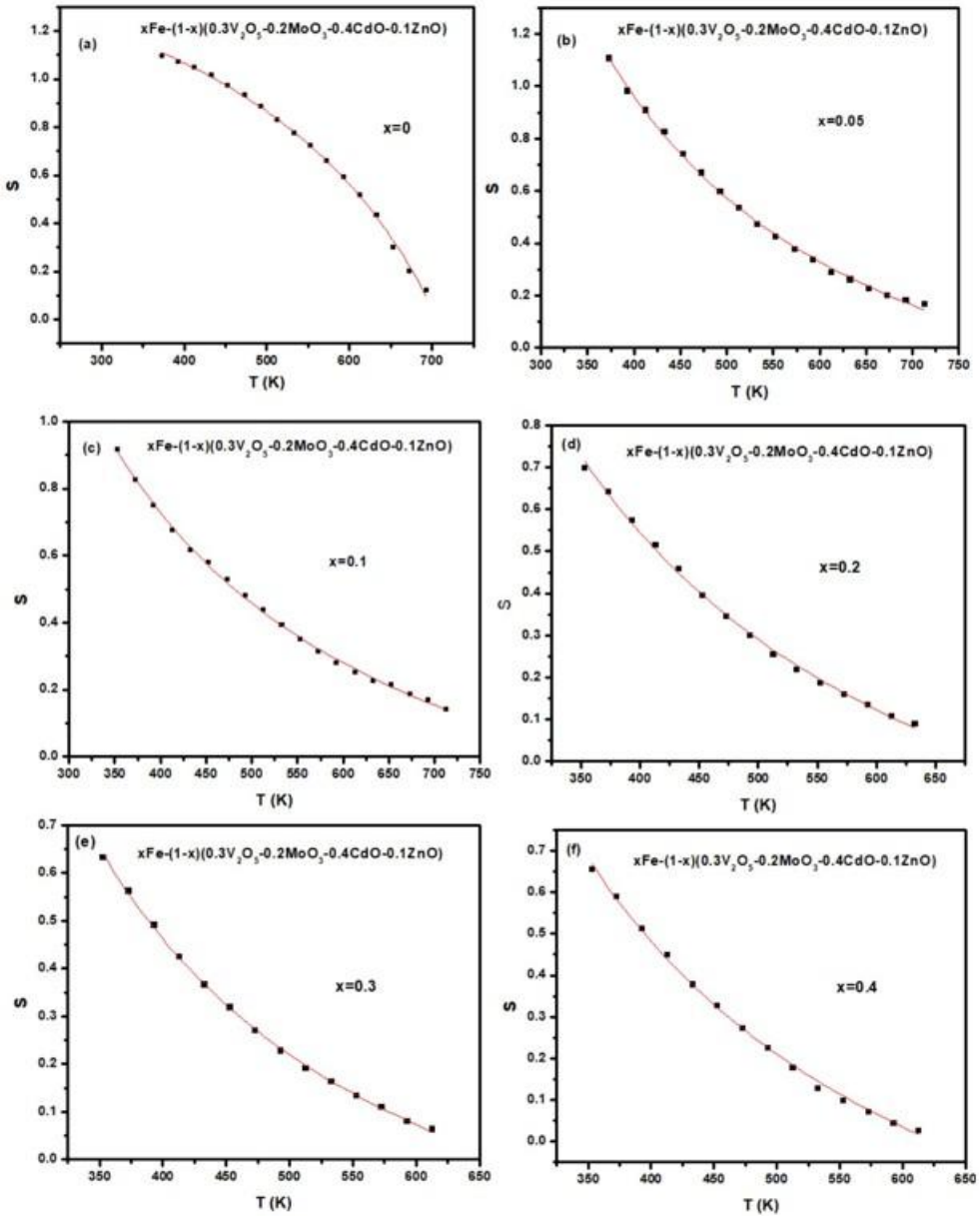

Fig. 4.2.8: Variation of S versus T plots for xFe – (1-x) ($0.3V_2O_5$ – $0.2MoO_3$ – 0.4CdO – 0.1ZnO) prepared system with x= (a) 0.0, (b) 0.05, (c) 0.1, (d) 0.2, (e) 0.3 and (f) 0.4. Solid lines in the plots are the nonlinear best-fit data of the Modified CBH Model.

Table 4.2.3: Parameters of CBH (Modified) model of the glass nanocomposites, xFe – (1-x) ($0.3V_2O_5 – 0.2MoO_3 – 0.4CdO – 0.1ZnO$) with different values of x. Estimated errors are also covered.

x	CBH (modified) model		
	P1=Wm (eV) (±0.10)	**P2=τ_0 (s) (±0.001)**	**P3=T_0 (s) (±0.50)**
0.0	1.19759	0.00401	307.24892
0.05	1.17194	0.00519	312.69933
0.1	1.12114	0.00708	314.19986
0.2	1.12994	0.00799	294.32869
0.3	1.10677	0.00808	291.11936
0.4	1.12114	0.0046	293.4948

4.2.3.2 Almond–West formalism

Figure 4.2.9 shows the AC conductivity spectra of a specific sample for all samples of a produced glassy system at different temperatures. It is manifested from Fig. 4.2.9 that the spectra of conductivity exhibit thermally excited behaviour. The frequency-independent zone appears when the frequency is lower, as seen in Fig. 4.2.9. It has a relationship with DC conductivity. At the crossover or hopping frequency, the dispersion begins to change from almost constant DC conductivity to AC conductivity. For all samples (x=0.0, 0.05, 0.1, 0.2, 0.3, and 0.4) AC conductivity plots were examined for different x values. The Almond-West Formalism [212] technique has been extensively utilized to explore frequency-dependent conductivity, which may be written as [212]:

$$\sigma\ (\omega) = \sigma_{dc}[(1 + (\frac{\omega}{\omega_H})^n \qquad (4.2.12)$$

Where, ω_H =hopping crossover frequency, n =fractional power law exponent, and σ_{dc} = low-frequency conductivity

In Figs. 4.2.9 and 4.2.10, AC conductivity data from a glassy system corresponded with the Almond-West Formalism to provide sufficient data regarding the conduction process. Using Eq. (4.2.12), values of parameters ω_H, n, and σ_{dc} have been obtained. AC conductivity data is

well by the frequency, which has already been shown in Fig. 4.2.9. At a fixed temperature of 513K, the conductivity spectra of all compositions (x =0.0, 0.05, 0.1, 0.2, 0.3, and 0.4) have been presented in Fig. 4.2.10. The behaviour of AC conductivity plots is unchanging as variations of doping Fe content. It is also marked in Fig. 4.2.10 that the order of the AC conductivity increases with raising Fe content in the matrices.

In Fig. 4.2.11 (a), the estimated values of ω_H were plotted against the temperature for all x values, indicating thermally triggered behaviour. Activation energy corresponding to ω_H of the glassy system attained from the best-fitted straight lines's slopes, which has been exhibited in Fig. 4.2.11. The estimated activation energies (E_H) for ω_H and n have been shown in Table 4.2.4. As prepared present glassy system illustrated that the hopping mechanism is the only component influencing the conductivity [214]. The values of n are shown in Table 4.2.4. Here, this present glassy system provides the higher values of n, which normally suggests the percolation-type motion [22, 83, 192, 212, 214-216]. Figure 4.2.11 (b)shows the spectra of AC conductivity of all compositions (x = 0.0, 0.05, 0.1, 0.2, 0.3, and 0.4) at temperature 513 K. From this figure, it can easily be understood that when Fe content is increased in the glass system, then AC conductivity is also found in increasing order. These results confirmed the results which are established from the DC conductivity analysis.

Table 4.2.4: Activation Energy for Hopping Frequency of glass nanocomposites, xFe – (1-x) ($0.3V_2O_5$ – $0.2MoO_3$ – 0.4CdO – 0.1ZnO) with different values of x. Calculated errors are covered.

X	**Activation Energy**	**n (±0.10)**
0.0	1.00	1.00
0.05	0.65	1.07
0.1	0.57	1.09
0.2	0.45	1.11
0.3	0.40	1.13
0.4	0.31	1.16

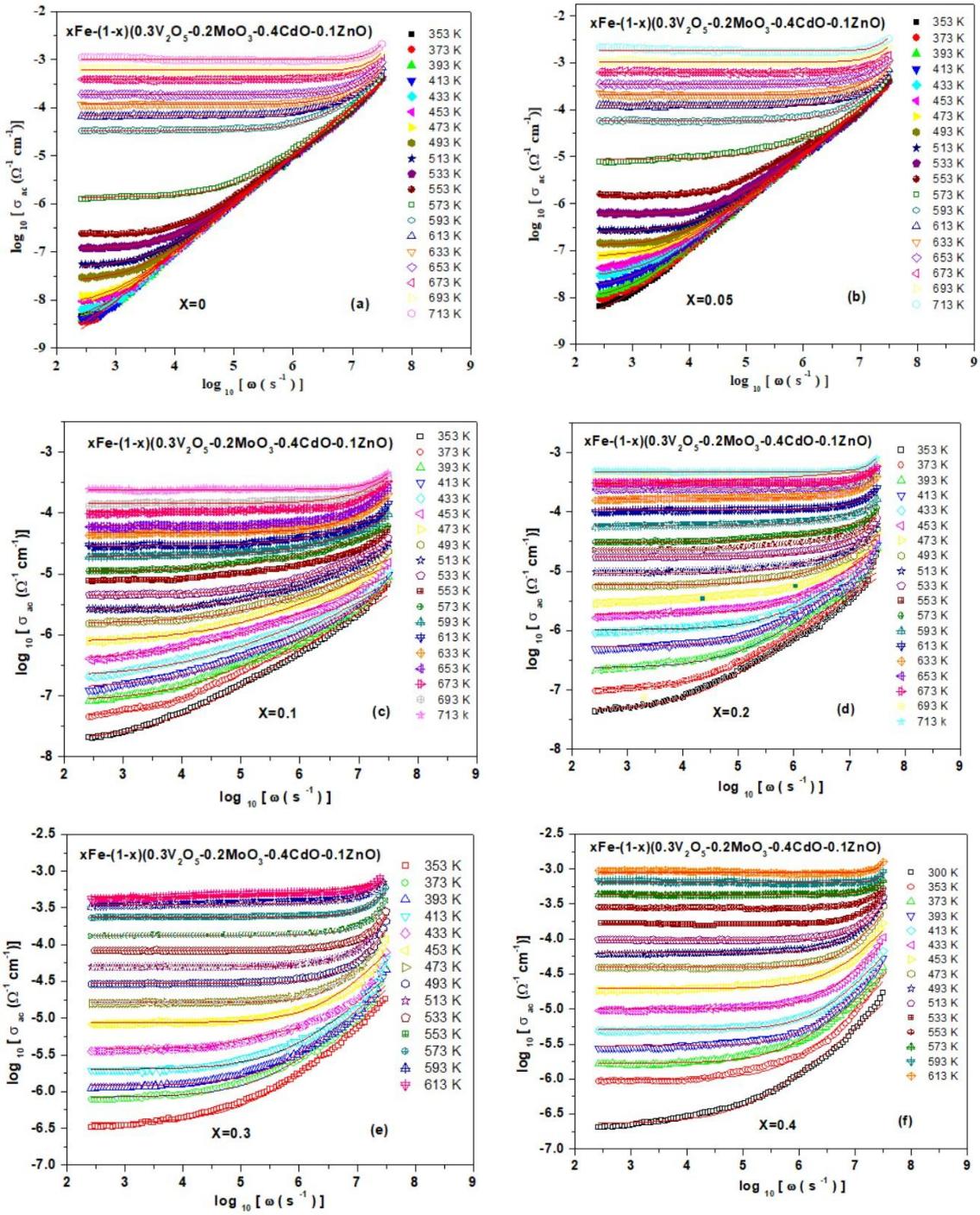

Fig. 4.2.9: Conductivity spectra at different temperatures for xFe – (1-x) ($0.3V_2O_5$ – $0.2MoO_3$ – 0.4CdO – 0.1ZnO) glass nanocomposite where x= 0.0, 0.05, 0.1, 0.2, 0.3 and 0.4. Solid lines that are seen in the plots indicate the fitting with Almond West Formalism.

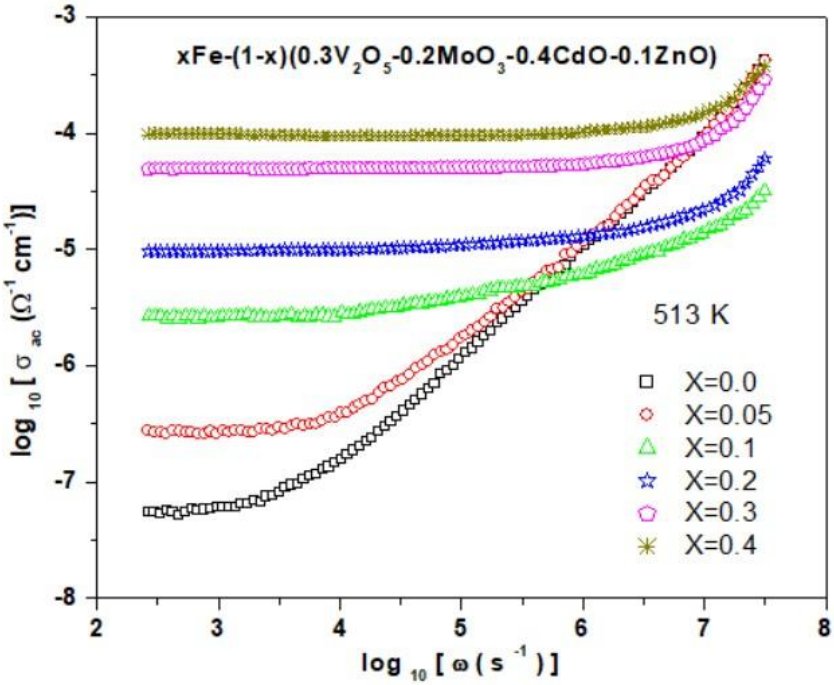

Fig. 4.2.10: Conductivity spectra for all prepared samples (x=0.0, 0.05, 0.1, 0.2, 0.3, and 0.4) at temperature 513 K.

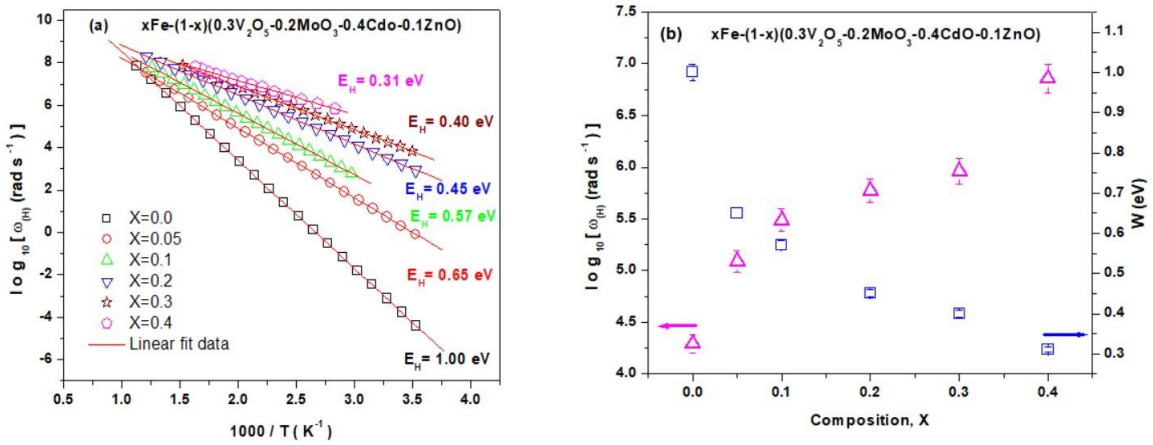

Fig. 4.2.11: (a) Differences of ω_H with 1000/T of xFe – (1-x) $(0.3V_2O_5 – 0.2MoO_3 – 0.4CdO – 0.1ZnO)$ glass nanocomposite with different values of x, solid lines indicate best-fitted straight lines. (b) Variation of ω_H and E_H corresponding to composition (x).

4.2.3.3 AC conductivity scaling

According to various literature, the "time-temperature superposition" (TTS) principle is a recognized technique for analyzing and predicting the temperature-dependent behavior of glassy materials [217-218]. TTS has scaled and adjusted the AC conductivity data such that it

can be overlaid onto a single master curve in terms of temperature and composition dependency [192, 217-218]. The conductivity axis and frequency axis have been sealed by σ_{dc} and ω_H, respectively, in this temperature scaling of conductivity spectra, which is followed by the expression:

$$\sigma(\omega)/\sigma_{dc} = F\ (\omega/\omega_H) \qquad (4.2.13)$$

Where, F= Scaling function, which is independent of temperature and composition. Figure 4.2.12 (a) shows the temperature scaling curve at various temperatures for a, x = 0.3 sample. It has been clearly stated in Fig. 4.2.12 (a) that conductivity spectra scaling obeys the TTS principle and all temperatures have an almost good overlap in a single master curve. At a certain temperature (513K), the temperature scaling of all prepared samples is shown in Fig. 4.2.12 (b), indicating that conductivity spectra for all glass compositions are not properly overlapped. As a result of the scaling phenomena of the currently glassy system, it has been demonstrated that the common relaxation mechanism of charge carriers/polarons is temperature-independent, but heavily reliant on composition or structure. [23].

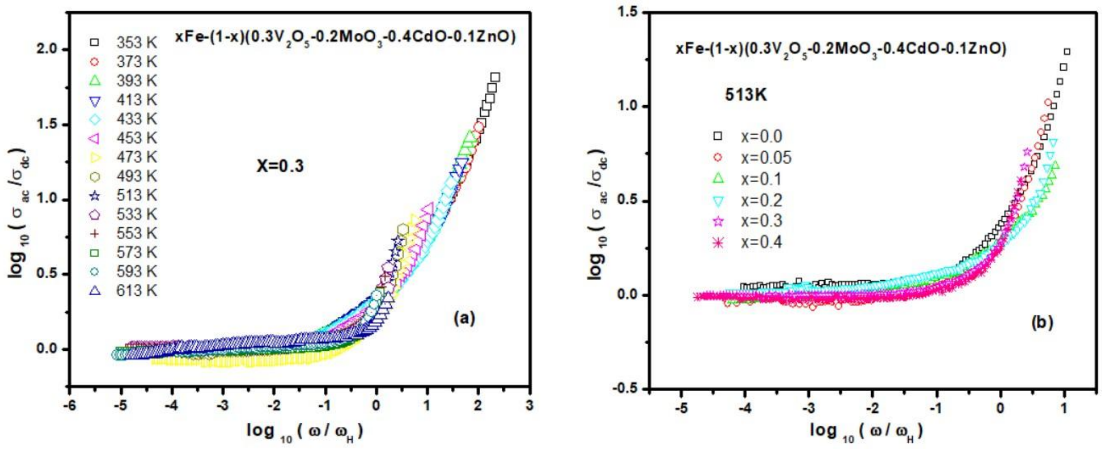

Fig. 4.2.12: (a)Temperature scaling of the AC conductivity spectra at different temperatures of the system for x=0.3 and (b) Temperature scaling of conductivity spectra for all compositions at a fixed temperature (513 K).

4.2.4 Conclusion

Fe undoped (x=0.0), as well as Fe, doped (x= 0.05, 0.1, 0.2, 0.3 and 0.4) nano glassy system has been investigated the electrical properties which were prepared through melt quenched method. FTIR reports indicate that to make a vibration in the Mo-O and Zn-O bands,

minimal energy is required so that an acoustic phonon contribution is induced when the Fe content increases. The larger the acoustic vibration, the more unstable the current system, which contains more Fe. It has been revealed that the DC conductivity of the present glassy system increases with temperature. XRD result shows that on the evolvement of different nano phases, structural modification should emerge. This limited lattice distortion results from the structural arrangement in the present system when Fe concentration is adjoined. When the current system is steadily increased with Fe, this type of environment charges a conversion of conduction technique from large to small hoping polaron. Both DC and AC conductivity have been increased as Fe is doped, which also shows a similar nature. The modified CBH model has been deployed to state the nature of S corresponds to temperature in the system and the prevalent conduction method is anticipated in the current system. It has also been found that the activation energy for DC conductivity (σ_{dc}), as well as hopping frequency (ω_H), are almost the same for all prepared samples (x=0.0, 0.05, 0.1, 0.2, 0.3, and 0.4) of the current glassy system. AC conductivity scaling phenomena have indicated that the common relaxation mechanism of charge carriers/ polarons is temperature-independent, but strongly dependent on the composition or structure of the presently glassy system.

4.3 Mechanical Properties of Fe-V_2O_5-MoO_3-CdO-ZnO Glass Nanocomposite System

4.3.1 Introduction

Microhardness studies in nanocomposite materials have seen limited research in the last few years, and are less commonly described in the literature. Nowadays, the mechanical properties of nanocomposites are crucial due to their exceptional chemical and physical attributes, making them highly useful in practical-world scenarios [56]. Glass nanocomposite materials have great interest in research because of their exceptional application in the field of solid-state ionic devices such as electrochemical capacitors, gas sensors, fuel cells, analog devices, and electrochromic displays, etc [119-121]. In addition, due to its high mechanical properties, transparent glass-ceramics are greatly accepted materials for the protective cover of the new generation mobile phones [12-13]. The parameters of microhardness measurement give valuable information about the composition of the materials. Apart from this, microhardness study also helps to measure the materials' yield strength, elastic modulus, and shear modulus. Vickers microhardness method is the convenient method for measuring the microhardness of composite systems [138-141].

Many models were established to illustrate ISE behavior in materials, including Meyer's law, elastic/plastic deformation models (EPD), proportional sample resistance (PSR), and the Hays–Kendall (HK) approach, which relates applied indentation test load (P) to the diagonal length of the indentation (d).[147-149].

The present study investigates the Vicker's microhardness behaviour of a new glassy nanocomposite system $xFe – (1-x) (0.3V_2O_5 – 0.2MoO_3 – 0.4CdO – 0.1ZnO)$ with x=0.0, 0.05, 0.1, 0.2, 0.3, and 0.4 along with different heat treatment condition. In the next step, we will investigate the effect of iron on this new glassy system's microhardness behavior. The experimental Vickers micro-hardness values have been calculated and analysed using various models to describe the usual ISE and the unusual reverse ISE in crystalline solids during as prepared as well as different heat treatment conditions.

4.3.2 Microhardness Analysis

The Vickers microhardness values (H_v) of the glass nanocomposite system, for various values of x were measured at various test loads ranging from 0.049 N to 0.980 N. The

microhardness values for each sample at different loads are presented in Table 4.3.1, and the changing of H_v with the load is illustrated in Fig. 4.3.1. For all samples, the microhardness values increased with increasing applied load. This trend is consistent in all Fe concentration batches, indicating a load-dependent hardness behaviour. The indentation size also increased with the applied load, showing two distinct regions in the load-hardness curve: the low load zone (AB) and the high load zone (BC). In the low load zone (AB), the behaviour is load-dependent and non-linear, while in the high load zone (BC), the behaviour is nearly linear and reaches a saturation point, referred to as the plateau region [134-137].

The microhardness values at a specific load increase with the Fe content in the samples. For instance, at a load of 0.049 N, the $H_v$value for x=0.0 is 1.0032 GPa, while for x=0.04, it increases to 1.7336 GPa. This represents a significant enhancement of approximately 72.8% in microhardness with the addition of Fe up to 0.4 concentration. Similarly, at a higher load of 0.980 N, the H_v value for x=0.0 is 3.0763 GPa, whereas, for x=0.4, it reaches 5.2321 GPa, marking a substantial increase of about 70.1%. The increase in hardness with Fe concentration suggests that Fe plays a crucial role in doing better with the mechanical properties of glass nanocomposites. Increasing Fe concentration indicates the presence of more Fe-containing crystal phases, and enhances the hardness. These results are in good concurring with the XRD and SEM investigations.

The load-dependent microhardness values show that as the load increases, the indentation size also increases. This is evident from the indents' larger diagonal lengths (d) at higher loads. The Vickers microhardness curves for all samples display two regions. In the low load zone (AB), there is a significant increase in microhardness values, suggesting that fresh dislocations are being nucleated at the indented zone. This behaviour is indicating the reverse indentation size effect, where hardness is increased with an increase in load applied. In the high load zone (BC), the microhardness values approach a plateau, indicating that the material has reached its maximum resistance to deformation under the applied loads [134-137]. For example, the plateau region for x=0.0 occurs at approximately 2.4952-3.0763 GPa, while for x=0.4, it is between 4.9230-5.2321 GPa. This behaviour suggests that the material exhibits stable and consistent hardness properties at higher loads, which is crucial for applications requiring high load-bearing capacity.

The elastic modulus (E) values for each sample at different loads are presented in Table 4.3.1. The elastic modulus (E) values (Discussed in section 3.4.3 of chapter 3) for the glass nanocomposites were calculated using the Vickers hardness values [161]. The data shows that the elastic modulus increases with both the applied load and the Fe concentration in the samples. For x=0.0 at a load of 0.049 N, the elastic modulus is 82.22699 GPa, whereas, for x=0.4 at the same load, it is 142.09520 GPa, indicating an increase of about 72.8%. At a higher load of 0.980 N, the elastic modulus for x=0.0 is 252.14791 GPa, while for x=0.4, it is 428.84122 GPa, showing an enhancement of approximately 70.1%. The data shows that the elastic modulus increases with both the applied load and the Fe concentration in the samples. This trend indicates that the materials become stiffer and more resistant to elastic deformation with increasing Fe content and applied load, making them more suitable for applications requiring high elastic modulus.

The yield strength (Y) values for each sample at different loads are presented in Table 4.3.1. The yield strength (Y) values (Discussed in section 3.4.3 of chapter 3) were derived from the Vickers hardness values, and the results indicate a similar trend to that observed for the elastic modulus [161]. The yield strength increases with higher Fe content and applied load, reflecting the enhanced ability of the material to withstand permanent deformation. At a load of 0.049 N, the yield strength for x=0.0 is 0.33440 GPa, whereas, for x=0.4, it is 0.57788 GPa, showing an increase of about 72.8%. At a load of 0.980 N, the yield strength for x=0.0 is 1.02544 GPa, and for x=0.4, it is 1.74403 GPa, reflecting an enhancement of approximately 70.1%. The increase in yield strength with Fe concentration suggests that Fe doping significantly improves the material's resistance to yielding and permanent deformation, which is crucial for structural applications.

The shear modulus (G) values for all samples at different loads are presented in Table 4.3.1. The values of shear modulus(Discussed in section 3.4.3 of chapter 3) were derived from the Vickers hardness values, and the results indicate a similar trend to that observed for the elastic modulus [161]. The shear modulus increases with higher Fe content and applied load, reflecting the enhanced ability of the material to withstand permanent deformation. At a load of 0.049 N, the shear modulus for x=0.0 is 6.643807 GPa, whereas for x=0.4, it is 11.48106 GPa, showing an increase of about 72.8%. At a load of 0.980 N, the shear modulus for x=0.0

is 20.37314 GPa, and for x=0.4, it is 34.64967 GPa, reflecting an enhancement of approximately 70.1%.

The observed microhardness results demonstrate a reverse ISE, where hardness is increased with an increase in load applied. This behaviour can be attributed to the nucleation of fresh dislocations at the indented zone, which improves the material's resistance to deformation at higher loads. The reverse indentation size effect is evident from the significant increase in microhardness values with increasing loads, particularly in the low load zone (AB) [48, 50-51, 134-137]. The presence of RISE in the glass nanocomposites indicates that the materials exhibit superior mechanical performance under varying loads. This behaviour is beneficial for applications where materials are subjected to different loading conditions, as it ensures consistent and reliable mechanical properties. The improvement in mechanical properties with Fe doping can be attributed to changes in the microstructure and phase composition of the glass nanocomposites. XRD analysis (Details in section 4.1.5 of chapter 4) reveals the presence of crystalline phases such as $FeVO_4$, $Cd_2V_2O_7$, and V_2MoO_8 in the samples. These phases contribute to the enhanced hardness, elastic modulus, and yield strength of the materials.

Table 4.3.1: Calculated H_V, E, Y & G values pertaining to the prepared glass nanocomposites xFe – (1-x) $(0.3V_2O_5 – 0.2MoO_3 – 0.4CdO – 0.1ZnO)$with different values of x.

Samples	P (N)	d (μm)	Hv (GPa)	Plateau region (GPa)	E (GPa)	Y (GPa)	G (GPa)
x=0	0.049	9.521	1.0032	2.4952-3.0763	82.22699	0.33440	6.643807
	0.098	11.80	1.3063		107.07000	0.43543	8.651081
	0.245	15.402	1.9167		157.10130	0.63890	12.69353
	0.490	19.09	2.4952		204.51736	0.83174	16.52467
	0.980	24.314	3.0763		252.14791	1.02544	20.37314
x=0.05	0.049	8.95	1.1353	2.7836-3.3666	93.055359	0.37844	7.518721
	0.098	10.072	1.7927		146.94393	0.59759	11.87283
	0.245	14.041	2.3061		189.02384	0.76873	15.27282
	0.490	18.074	2.7836		228.15372	0.92786	18.43445
	0.980	23.242	3.3666		275.94360	1.12222	22.29579
x=0.1	0.049	8.22	1.3459	3.2679-3.7591	110.31542	0.44863	8.913306
	0.098	9.843	1.8771		153.85837	0.62571	12.4315
	0.245	13.038	2.6746		219.22324	0.89154	17.71288
	0.490	16.681	3.2679		267.85102	1.08931	21.64192
	0.980	21.9951	3.7591		308.11334	1.25305	24.89505
x=0.2	0.049	7.774	1.5046	3.5167-4.0357	123.32916	0.50156	9.964794
	0.098	9.189	2.15397		176.54698	0.71799	14.26471
	0.245	12.665	2.8345		232.32657	0.94483	18.77161
	0.490	16.08	3.5167		288.24476	1.17224	23.2897
	0.980	21.228	4.0357		330.78395	1.34524	26.7268
x=0.3	0.049	7.377	1.6710	4.0357-4.8676	136.96127	0.55700	11.06625
	0.098	8.458	2.5422		208.37304	0.84742	16.8362
	0.245	11.286	3.5694		292.56515	1.18981	23.63879
	0.490	14.259	4.0357		366.56713	1.49077	29.61802
	0.980	19.329	4.8676		398.97308	1.62256	32.23637
x=0.4	0.049	7.245	1.7336	4.9230-5.2321	142.09520	0.57788	11.48106
	0.098	7.933	2.8919		237.03434	0.96398	19.15199
	0.245	10.801	3.8980		319.49864	1.29935	25.81497
	0.490	13.593	4.9230		403.51040	1.64101	32.60298
	0.980	18.644	5.2321		428.84122	1.74403	34.64967

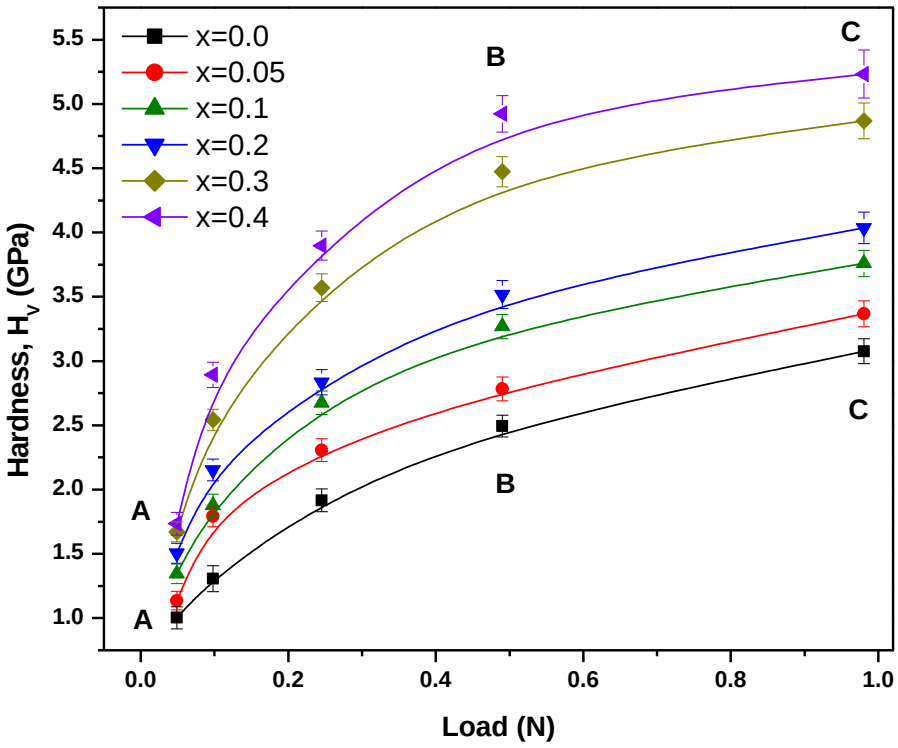

Fig. 4.3.1: The changes of microhardness along with various loads of the xFe – (1-x) ($0.3V_2O_5$ – $0.2MoO_3$ – 0.4CdO – 0.1ZnO) glass system for various values of x.

4.3.3 Analysis of Theoretical Models of Microhardness

The applied load on the indenter is a critical factor influencing the microhardness of a specimen. This relationship is captured by the phenomenon known as the ISE, where the microhardness of a material either increases or decreases with the applied load [48-50, 219]. Understanding this effect is essential for interpreting the mechanical behaviour of materials under different loading conditions [48]. There are two primary categorizations observed in indentation: the ISE and the reverse RISE [48].

In normal ISE, an increase in the applied test load leads to a decrease in microhardness. This behaviour is commonly observed in many materials and is attributed to the greater penetration depth of the indenter under higher loads, which tends to sample a larger volume of the material, including more defects and softer regions [48, 51, 135]. The larger contact area at higher loads distributes the applied force over a broader region, leading to a lower measured hardness. This phenomenon can be explained by factors such as the distribution of dislocations, strain hardening, and the heterogeneity of the material at different scales. Contrary to the normal ISE, RISE is characterized by an increase in microhardness with an increase in the applied test load [48-51]. This behaviour, observed in the present study, indicates that the

material exhibits greater resistance to deformation as the load increases. The RISE behaviour is often associated with the nucleation and interaction of dislocations, as well as the activation of additional deformation mechanisms at higher loads [48, 51, 135]. This effect suggests that the material becomes tougher and more resistant to plastic deformation as the load increases, which is a desirable for many engineering applications [48-51, 135, 145].

Several theoretical models established to investigate the ISE and reverse ISE behaviours of materials. Such models are crucial for explaining the structural and mechanical behavior of glass nanocomposites under different loading conditions. In this present study, various models like Meyer's law, EPD model, PSR model, HK approach, and IIC model were used to investigate Vickers microhardness values of as prepared glassy samples (x=0.0, 0.05, 0.1, 0.2, 0.3 and 0.4).

4.3.3.1 Meyer's law

Meyer's Law is fundamental in understanding the hardness behaviour of materials under varying loads [48, 146, 150] (Details in section 2.11.4.1 of chapter 2). The law establishes an interrelation between the applied load (P) and the resulting indentation diagonal length (d), expressed by the formula:

$$P = Ad^n \qquad (4.3.1)$$

Here, A is a material constant and n indicates Meyer's index, which indicates the nature of the indentation size effect (ISE). This law is instrumental in distinguishing between normal ISE and reverse indentation size effect (RISE) [46, 48, 146, 150]. For normal ISE, n is less than 2, signifying that hardness decreases with increasing load. In contrast, for RISE, n is greater than 2, mentioning an increase in hardness with increasing applied load. The special case where n=2 is described by Kick's Law, which states that microhardness is independent of the applied load. Figure 4.3.2, is best fitted using Meyer's Law equation [48, 146, 150]. The fitting parameter values (A and n) for all samples are presented in Table 4.3.2.

The importance of Meyer's Law lies in its ability to characterise the hardness behavior of materials under varying loads, providing insights into the material's deformation mechanisms. It can quantitatively determine whether the samples exhibit normal ISE or RISE by calculating Meyer's index for different Fe-doped glass nanocomposite samples. For example, Meyer's index values for all the nano glass composite is $n > 2$, indicating a RISE behaviour. Higher Meyer's index values indicate enhanced hardness with increasing load, reflecting the material's improved resistance to deformation. This information is crucial for applications where high mechanical strength is required [50, 155]. Meyer's index also provides

insights into the dominant deformation mechanisms at different loads. In the case of RISE, the increase in hardness with load suggests that additional mechanisms, such as dislocation interactions and phase transformations, become active at higher loads. Figure 4.3.2 and Table 4.3.2 shows that the value of n exceeds 2 for all glass nanocomposites. Due to these values of n, all glassy nanocomposite-prepared samples have been considered to follow RISE behavior.

Table 4.3.2: Experimental fitting parameters data according to Meyer's law for the prepared system.

Samples	**Mayer index (n)**	**lnA (GPa)**	**Hv (GPa)**
x=0	3.22695	-10.27002	2.4952-3.0763
x=0.05	3.013	-9.43966	2.7836-3.3666
x=0.1	3.03288	-9.29945	3.2679-3.7591
x=0.2	2.94467	-8.93952	3.5167-4.0357
x=0.3	3.06476	-8.95841	4.0357-4.8676
x=0.4	3.08173	-8.81079	4.9230-5.2321

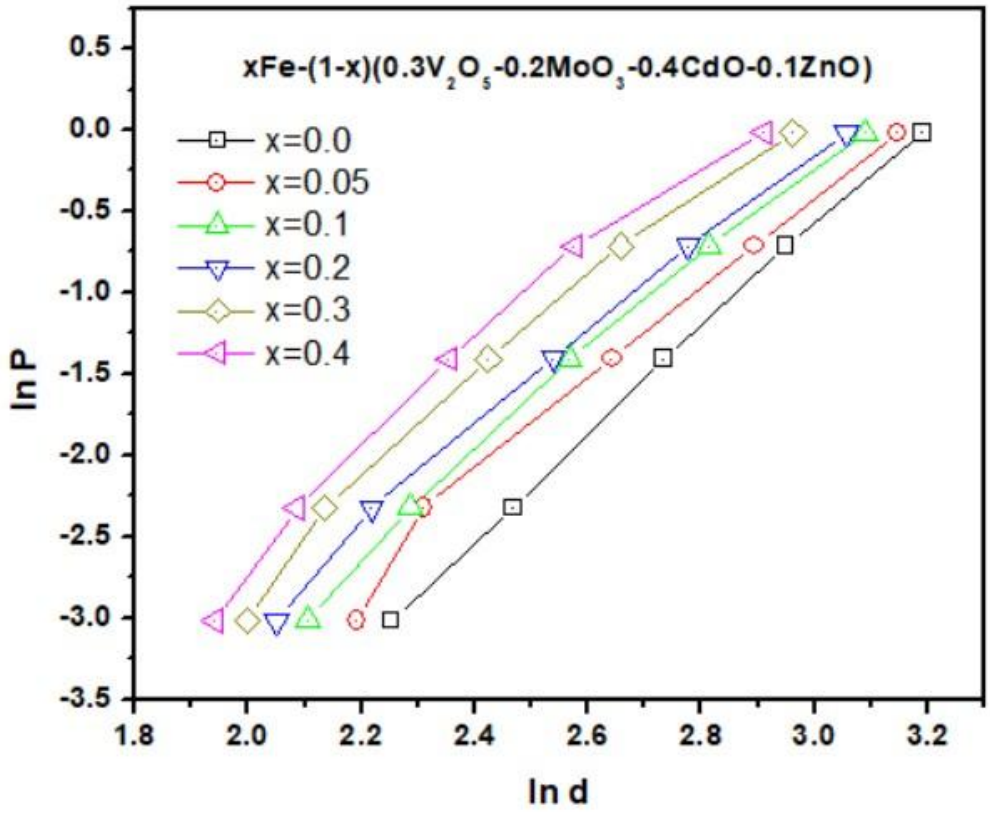

Fig. 4.3.2: Graph of ln P versus ln d for the prepared samples with various x values using Meyer's law.

4.3.3.2 Elastic/plastic deformation approach

The EPD approach (Details in section 2.11.4.2 of chapter 2) is a pivotal model for elucidating the ISE and RISE behaviors in glass nanocomposite samples [142, 151]. This model emphasises the elastic recovery surrounding the indentation impression and the formation of plastically deformed bands, capturing the complexity of deformation mechanisms. The EPD model is represented by the equation.

$$P = A_1 (d_p + d_e)^2 \qquad (4.3.2)$$

Here A_1 is a constant of load-independent, d_p, and d_e are the plastic deformation correction term, and the elastic deformation correction term. This equation underscores the interplay between plastic and elastic deformations under applied loads [142].

In the current study, the relationship between $P^{1/2}$ and d_p was analyzed (Figure 4.3.3), and the constants were derived from the best-fit straight lines in the $P^{1/2}$ versus d_p plot, as summarised in Table 4.3.3. The values of elastic deformation (d_e) were found to range from "-0.217 to -0.297" μm, indicating a negative nature and thereby confirming the RISE behaviour of the nano glassy composites [48, 142]. This negative elastic deformation suggests significant local structural disorders and grain size enlargement due to continuous Fe doping, which facilitates crack propagation in the samples. The negative values of d_e are critical because they highlight the material's tendency to exhibit increased hardness with increasing load, contrary to the typical ISE behaviour where hardness decreases with increased load.

The local structural disorder, as inferred from the negative d_e values, is indicative of Fe doping-induced defects and dislocations, which contribute to enhanced hardness at higher loads [48, 161]. The plastic deformation term (d_p) reflects the material's capacity to undergo permanent deformation, which determines the overall indentation response in conjunction with the elastic recovery. By combining these factors, simpler deformation models cannot capture the full complexity of deformation behaviour.

Vickers microhardness values for the EPD model (H_{EPD}) have been estimated from the Eq. 2.7 of Chapter 2. The microhardness values derived from this model (Table 4.3.3) show significant deviations from the experimentally observed Vickers microhardness values. For instance, the EPD model predicts a microhardness of 5.115 GPa for the x=0.0 sample, whereas the Vickers microhardness ranges from 2.4952 to 3.0763 GPa. Similarly, for the x=0.4 sample,

the EPD-derived hardness is 8.156 GPa, while the Vickers hardness ranges from 4.9230 to 5.2321 GPa.

These discrepancies underscore the limitations of the EPD model in fully capturing the real load-dependent microhardness behaviour of glass nanocomposite samples. The EPD model's theoretical framework emphasises the elastic and plastic contributions to hardness, yet it may overlook other critical factors such as microstructural heterogeneity, phase distribution, and the presence of secondary phases, which significantly influence the material's hardness [48, 142].

Furthermore, the EPD model's ability to explain the RISE behaviour is linked to the negative elastic deformation values. This behaviour contrasts with typical ISE behaviour observed in other materials, where positive elastic deformation values indicate a decrease in hardness with increasing load [48, 142, 151]. The negative values suggest that the prepared glassy nanocomposite samples exhibit unique deformation mechanisms, possibly due to the specific nature of Fe doping and its effect on the glass matrix.

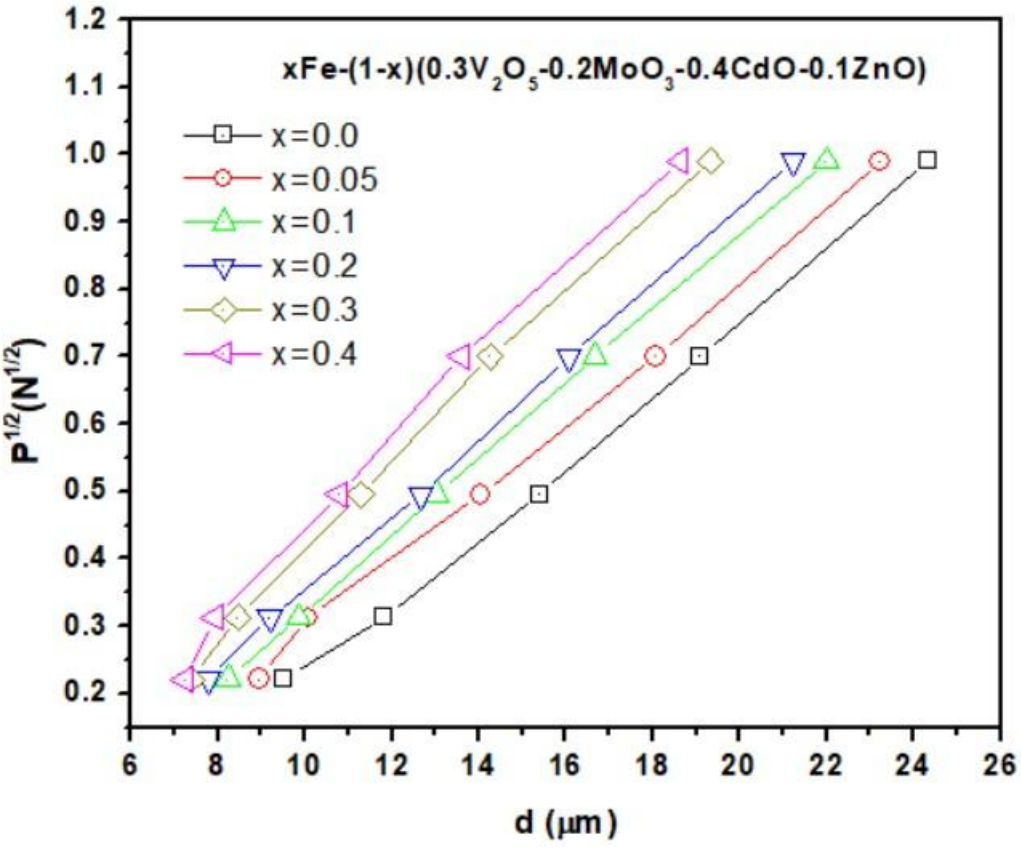

Fig. 4.3.3: Graphs of $P^{1/2}$ over d for the prepared samples with various x values using EPD Model.

Table 4.3.3: Experimental fitting parameters data according to EPD model for the prepared samples.

Samples	$A_2^{1/2}x10^3(N/\mu m^2)$	d_e (µm)	H_{EPD} (GPa)	H_V (GPa)
x=0	52.52	-0.297	5.1150	2.4952-3.0763
x=0.05	52.84	-0.236	5.1776	2.7836-3.3666
x=0.1	55.89	-0.235	5.7925	3.2679-3.7591
x=0.2	56.89	-0.217	6.0017	3.5167-4.0357
x=0.3	64.07	-0.233	7.6122	4.0357-4.8676
x=0.4	66.32	-0.228	8.1562	4.9230-5.2321

4.3.3.3 Proportional sample resistance model

The PSR model (Details in section 2.11.4.3 of chapter 2) is an essential tool for understanding the load-dependent as well as the load-independent microhardness of materials, particularly in the context of nanocomposite glass systems [150, 152-154].

The experimental fitting parameters (A and B, which can be derived from Eq. 2.8 of Chapter 2) from the PSR model, presented in Table 4.3.4, highlight significant observations. The negative values of A for all samples confirm the RISE behaviour, indicating that microhardness increases with increasing load [152, 155]. This negative value of A implies that the samples undergo predominantly plastic deformation, with no significant elastic recovery contributing to the indentation process. The B values, which are always positive, represent the load-independent constant associated with the intrinsic material hardness [152, 155].

In Fig. 4.3.4, the plot of the Fe-doped glass nanocomposites demonstrates the linear fit used to extract the values of A and B. The plot and corresponding linear fit confirm the model's applicability and validate the derived parameters [152, 155]. The gradual increase in B values with higher Fe content indicates that Fe doping improves the material's intrinsic resistance to indentation [153-154]. This trend correlates with the observed increase in Vickers microhardness (H_v) with higher Fe concentrations, as shown in Fig. 4.3.1.

The calculated load-independent Vickers microhardness values for the PSR model (H_{vPSR}) using Eq. 2.9 of Chapter 2 are summarised in Table 4.3.4, which are significantly higher than the actual measured Vickers microhardness values (H_v) at the saturation zone. For instance, the x=0.0 sample has a $(H_v)_{PSR}$ of 4.469 GPa compared to an actual H_v range of 2.4952 to 3.0763 GPa. Similarly, the x=0.4 sample exhibits a $(H_v)_{PSR}$ of 7.361 GPa, whereas the actual

H_v ranges from 4.9230 to 5.2321 GPa. This substantial difference suggests that while the PSR model provides a theoretical framework for understanding hardness, it may not fully capture the complex load-dependent behavior observed experimentally [153-154].

The PSR model's reliance on intrinsic structural factors and indenter orientation also plays a significant role in considering the hardness values. The negative A values, indicating RISE behavior, suggest that the prepared glass nanocomposites primarily undergo plastic deformation with minimal elastic recovery [51, 135]. This behaviour is consistent with the observed microstructural changes, such as increased grain size and structural disorder, due to Fe doping.

Furthermore, the gradual increase in B values with higher Fe content reflects the continuous improvement in the material's hardness properties [51, 135]. The incorporation of Fe into the glass matrix enhances the overall structural integrity, leading to increased resistance to deformation. This enhancement is attributed to the Fe atoms disrupting the glass network, creating localised stress fields that contribute to the material's hardness.

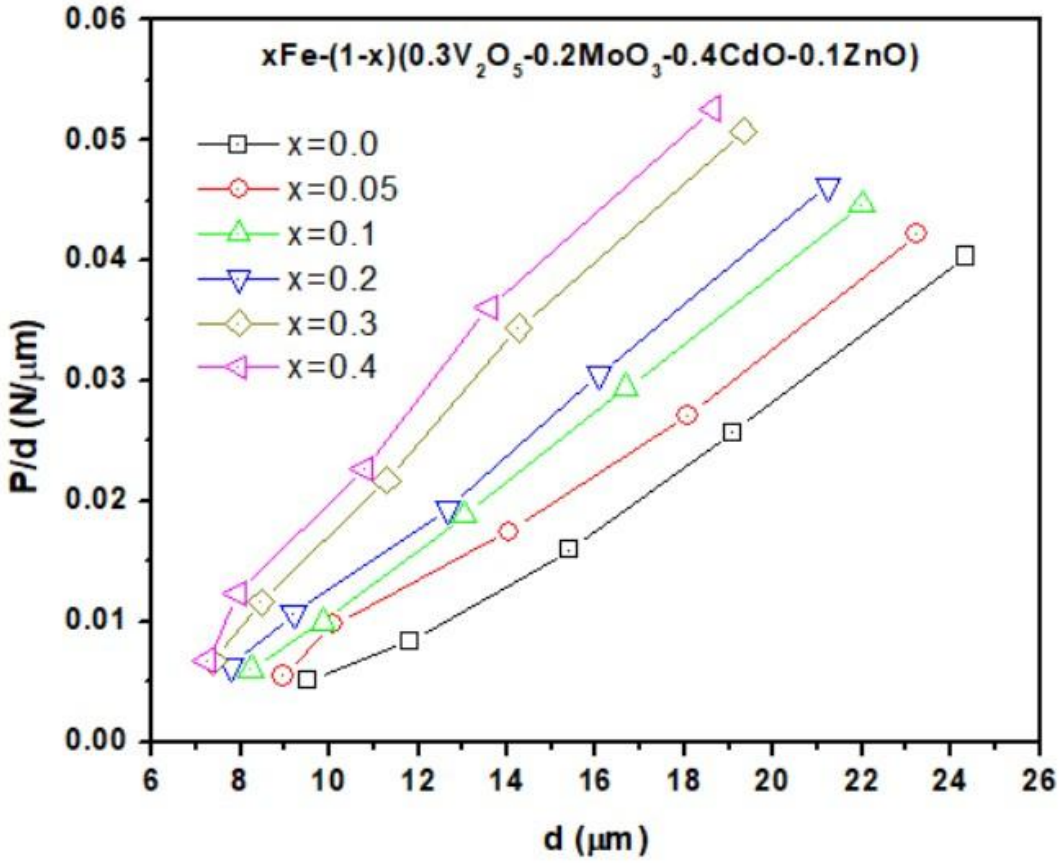

Fig. 4.3.4: Plots of P/d versus d for prepared samples using PSR model with different x values.

Table 4.3.4: Experimental fitting parameters data according to PSR model for the prepared samples.

Samples	**$Ax10^{-3}$ (N/µm)**	**$Bx10^{-4}$ ($N/\mu m^2$)**	**H_{PSR} (GPa)**	**H_V (Gpa)**
x=0	-19.58	24.1	4.4691	2.4952-3.0763
x=0.05	-16.59	24.9	4.6174	2.7836-3.3666
x=0.1	-17.62	28.2	5.2294	3.2679-3.7591
x=0.2	-16.99	29.6	5.4890	3.5167-4.0357
x=0.3	-19.89	37	6.8612	4.0357-4.8676
x=0.4	-20.11	39.7	7.3619	4.9230-5.2321

4.3.3.4 Hays Kendall approach

The HK model (Details in section 2.11.4.4 of chapter 2) provides a comprehensive approach to understanding the mechanical behavior and load-independent microhardness parameters of materials [145]. This model accounts for both plastic and elastic deformation when materials are subjected to a minimum test load.

The plot in Fig. 4.3.5, which shows the applied loads (P) versus the square of the diagonal length (d^2), helps in determining the values of A_3 and W from the best-fitted straight line. The parameters of A_3 and W have been already discussed in Eq. 2.10 of chapter 2. The negative values of W indicate that the effective load applied is slightly more than the actual applied load, suggesting that plastic deformation starts at a lower load than initially expected [145].

From Table 4.3.5, it is seen that W is negative. This conveys that the effective load is slightly more than the true functional load. The load-independent Vickers microhardness values (Hv_{HK}) using Eq. 2.12 of Chapter 2 are summarised in Table 4.3.5, and exhibit a significant increase with higher Fe content in the glass nanocomposites. For example, the x=0.0 sample has a $(Hv)_{HK}$ of 3.504 GPa, while the x=0.4 sample shows a $(Hv)_{HK}$ of 5.841 GPa. This increasing trend is attributed to the enhanced plastic deformation resistance due to Fe doping, which improves the overall hardness of the material.

However, the negative W values indicate that the HK model might not fully capture the elastic deformation component, as the effective load is consistently higher than the functional load. This observation suggests that the model primarily accounts for plastic deformation,

which is predominant in the material [48, 156]. The discrepancy between the calculated $(Hv)_{HK}$ values and the actual measured Vickers microhardness (Hv) at the saturation zone further supports this notion. For instance, the actual Hv values for the x=0.4 sample range from 4.9230 to 5.2321 GPa, which is lower than the calculated $(Hv)_{HK}$ of 5.841 GPa.

The positive A_3 values indicate a proportional increase in hardness with increasing indentation size, reflecting the material's resistance to deformation. This resistance is enhanced by Fe doping, which disrupts the glass network and introduces localized stress fields that contribute to the material's hardness. The increase in A_3 values with higher Fe content demonstrates the improved structural integrity and load-bearing capacity of the nanocomposites. The HK model highlights the significant role of Fe doping in enhancing the material's hardness and structural integrity, contributing to its improved load-bearing capacity [48].

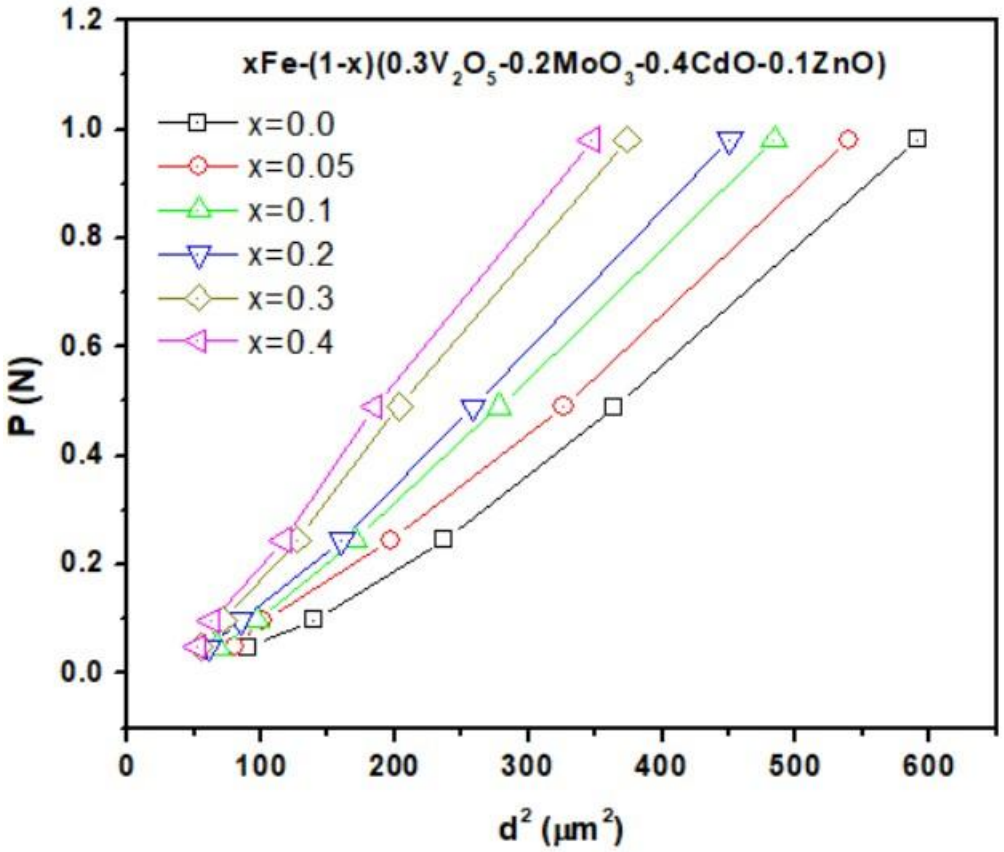

Fig. 4.3.5: Plots of P versus the d^2 for prepared samples using HK model.

Table 4.3.5: Experimental fitting parameters data according to HK model for a prepared system with various x values.

Samples	$A_3 \times 10^{-3}$(N/μm^2)	W_{HK} (N)	H_{HK} (GPa)	H_V (GPa)
x=0	1.89	-0.164	3.5048	2.4952-3.0763
x=0.05	2.00	-0.126	3.7088	2.7836-3.3666
x=0.1	2.25	-0.121	4.1724	3.2679-3.7591
x=0.2	2.40	-0.113	4.4505	3.5167-4.0357
x=0.3	2.93	-0.114	5.4333	4.0357-4.8676
x=0.4	3.15	-0.108	5.8413	4.9230-5.2321

4.3.3.5 Indentation-induced cracking model

The IIC model (Details in section 2.11.4.5 of chapter 2), developed by Li and Bradt, provides a comprehensive framework to analyze the mechanical properties of materials, particularly those exhibiting RISE behaviour [155, 156-159]. The values of K and m are load-independent constants, already explained in Eq. 2.14 of Chapter 2. The parameter m is crucial in determining the material's behavior: m > 0.6 indicates normal ISE behaviour, while m <0.6 indicates RISE behaviour [48, 50]. The values of m determined from the linear fit curve in Figure 4.3.6 for all nano-glassy samples range from 0.498 to 0.516. Since m < 0.6 for all samples, it is confirmed that the glass nanocomposite samples exhibit RISE behaviour. This behaviour indicates that as the applied load decreases, the hardness increases, a characteristic typically associated with significant plastic deformation before fracture [156-158].

The parameter K represents a load-independent constant related to the hardness of the material. The values of K increase with higher Fe content, from 6.036 for x=0.0 to 6.242 for x=0.4. This suggests that Fe-doping enhances the resistance of the glass nanocomposites to indentation-induced cracking, leading to higher overall hardness. Vickers microhardness values for the IIC model (H_{vIIC}) using Eq. 2.14 of Chapter 2 are tabulated in Table 4.3.6. The increase in K correlates well with the observed microhardness values (H_v), indicating that the IIC model effectively describes the hardness behavior of these materials.

To validate the IIC model, a comparison of microhardness values from different models (EPD, PSR, HK, and IIC) and the experimental Vickers microhardness (H_v) at the plateau region is necessary. The IIC model values (H_{vIIC}) closely match the experimental Vickers

microhardness (H_v), indicating its robustness in capturing the mechanical properties of Fe-doped glass nanocomposites. The slight variations between the experimental and theoretical values suggest that while the IIC model is effective, it might still require some adjustments for perfect alignment with experimental data [161]. As the Fe content increases, both the experimental and theoretical hardness values show an upward trend. This indicates that Fe incorporation strengthens the glass matrix, enhancing its resistance to deformation. The trend is consistent across all models, affirming the positive impact of Fe doping on the mechanical properties. The negative values of m in the IIC model confirm the RISE behaviour of the samples. This is further validated by the comparison with other models, where similar trends are observed, though the exact values differ. The RISE behaviour indicates predominant plastic deformation, which is critical for applications requiring high toughness and durability.

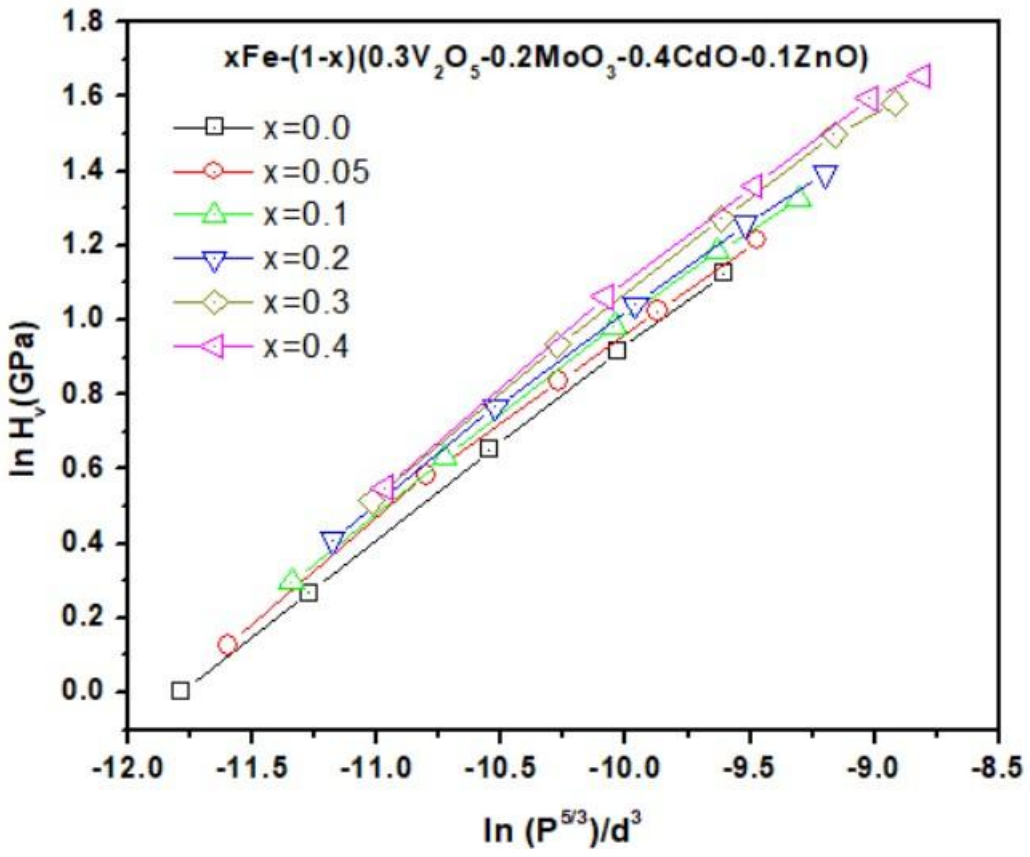

Fig. 4.3.6: Plots of Variation of $\ln H_v$ with $\ln(P^{5/3}/d^3)$ for prepared system with x values using IIC model.

Table 4.3.6: Experimental fitting parameters data according to IIC model for prepared samples.

Samples	M	lnK ($N^{(3-5m)/3}/\mu m^{(2-3m)}$	$(H_V)_{IIC}$ (GPa)	H_V (Gpa)
x=0	0.498	6.036	2.8247	2.4952-3.0763
x=0.05	0.506	6.098	3.0136	2.7836-3.3666
x=0.1	0.507	6.101	3.3813	3.2679-3.7591
x=0.2	0.509	6.147	3.6731	3.5167-4.0357
x=0.3	0.512	6.184	4.4552	4.0357-4.8676
x=0.4	0.516	6.242	4.9012	4.9230-5.2321

Table 4.3.7: The experimental Vickers microhardness results at the plateau region and the theoretical microhardness values calculated using EPD, PSR, HK, and IIC models.

Samples	$(H_v)_{EPD}$ (GPa)	$(H_v)_{PSR}$ (GPa)	$(H_v)_{HK}$ (GPa)	$(H_v)_{IIC}$ GPa)	H_v (GPa)
x=0	5.1150	4.4691	3.5048	2.8247	2.4952-3.0763
x=0.05	5.1776	4.6174	3.7088	3.0136	2.7836-3.3666
x=0.1	5.7925	5.2294	4.1724	3.3813	3.2679-3.7591
x=0.2	6.0017	5.4890	4.4505	3.6731	3.5167-4.0357
x=0.3	7.6122	6.8612	5.4333	4.4552	4.0357-4.8676
x=0.4	8.1562	7.3619	5.8413	4.9012	4.9230-5.2321

4.3.4 Microhardness Analysis (Different Heat Treatment Conditions)

The Vickers microhardness values (H_v) of the heat-treated glass nanocomposite at 600^0 C for 1h, 3h, and 5h were measured at various test loads ranging from 0.049 N to 0.980 N. The microhardness values for each heat-treated (1h, 3h, and 5h) samples at different loads are presented in Table 4.3.8 and the variation of Hv with the applied load is illustrated in Figure 4.3.7a-c. Figure 4.3.7a-c displays the microhardness values increased with increasing applied load for all the heat-treated samples (x=0.0 to 0.4). This trend is consistent across all Fe concentrations, indicating a load-dependent hardness behavior. The indentation size also increased with the applied load, showing two distinct regions in the load-hardness curve: the low and the high load zones [161]. In the low load zone, the behaviour is load-dependent and

non-linear, while in the high load zone, the behavior is nearly linear and reaches a saturation point, referred to as the plateau region [145, 52-55].

The microhardness values of heat-treated glass samples increase with Fe content under a specific load. After 1 hour of heat treatment at a low load of 0.049 N, the Hv value rises from 1.3328 GPa for x = 0.0 to 2.2694 GPa for x = 0.4, as shown in Table 4.3.8. This represents a significant enhancement of approximately 70.27% in microhardness with the addition of Fe up to 0.4 concentration. Similarly, at a higher load of 0.980 N, the Hv value for x=0.0 is 3.7746 GPa, whereas, for x=0.4, it reaches 5.8082 GPa, marking an increase of about 53.87%.

At a low load of 0.049 N, the Hv values for x = 0.0 are 2.3204 GPa and 2.3541 GPa after 3 h and 5 h of heat treatment, respectively. For x = 0.4, these values increase significantly to 5.6128 GPa and 5.6548 GPa for the same heat-treatment hours. Similarly, at a higher load of 0.980 N, the Hv values for x = 0.0 are 4.5693 GPa and 4.5831 GPa after 3 h and 5 h of heat treatment, respectively, while for x = 0.4, the values rise to 10.4453 GPa and 10.5329 GPa for the corresponding heat-treatment hours. The increase in hardness with Fe concentration suggests that Fe plays a crucial role in enhancing the mechanical properties of the glass nanocomposites.

For 1h heat treatment, the glass matrix of Fe undoped system was indicated to the nature which was identified as crystalline in nature but in the irregular shape of crystals and shows poor reinforcement from the crystalline phases [194]. Non-appearance of Fe may hinder the process of nucleation of crystals. So, the structure is commanded by a low mechanically strong amorphous phase. After 3h heat treatment, a significant rise in hardness was observed which reported the birth of first crystalline phases like $Cd_2V_2O_7$ and $Zn_3V_2O_8$ [194-198]. This phase offers limited reinforcement by making better the distribution of load under indentation. In a 5h time duration, the microstructure shows improved crystallinity and its resistance towards deformation is improved.

Low Fe Concentrations (x = 0.05, 0.1, and 0.2) improved hardness, as shown in Table 4.3.8, after 1h heat treatment. This was because of the development of nanophases like $FeVO_4$ [199-201]. This phase which is scattered within the matrix, enhances mechanical properties due to the distribution of stress effectively. Following 3 h of heat treatment, extended heat treatment facilitates the growth of Fe-based nanocrystals, significantly improving in hardness. After five hours of heat treatment, the microstructure exhibited a homogeneous distribution of nanocrystalline phases such as $FeVO_4$, $Zn_3V_2O_8$, and $Cd_2V_2O_7$ [194-201]. It was seen that in

the matrix, crystalline content was integrated well, reducing structural defects as well as enhancing mechanical integrity as a whole [48, 161].

At high Fe concentrations (x = 0.3 and 0.4) in heat-treated glass composites, Figure 4.3.7 and Table 4.3.8 reveal minimal differences in hardness values between these samples under both low and high-loading conditions. The results indicate that maximum hardness is achieved after 3h and 5h heat treatment, with only slight variations observed between the samples.

The higher Fe concentration promoted rapid nucleation of $FeVO_4$, $Zn_3V_2O_8$, and $Cd_2V_2O_7$ phases [194-201]. This increase was attributed to the formation of interlocking crystalline networks and the development of fine Fe-based nanocrystals. The microstructure became more rigid and resistant to deformation due to the synergistic effects of multiple crystalline phases. Prolonged heat treatment led to further crystallite growth and the development of a predominantly polycrystalline structure [161]. While the overall hardness remained high, minor phase segregation and coarsening in the high Fe concentration samples limited any further significant improvement [48].

The load-dependent microhardness values show that as the load increases, the indentation size also increases. This is evident from the larger diagonal lengths (d) of the indents at higher loads. The Vickers microhardness curves for all heat treatment samples (1h, 3h, and 5h) display two regions. In the low load zone (AB), there is a significant increase in microhardness values, suggesting that fresh dislocations are being nucleated at the indented zone in the samples. This behaviour is indicative of the RISE, where hardness increases with increasing load [48, 161]. In the high load zone (BC), the microhardness values approach a plateau, indicating that the material has reached its maximum resistance to deformation under the applied loads [53, 134, 136-137]. For example, during 3h heat treatment condition, the plateau region for x=0.0 occurs at approximately 4.2109-4.5693 GPa, while for x=0.4, it is between 9.9597-10.4453 GPa. This behaviour suggests that the material exhibits stable and consistent hardness properties at higher loads, which is crucial for applications requiring high load-bearing capacity [48].

Table: 4.3.8 The calculated Vickers microhardness (H_V) values pertaining for the prepared glass nanocomposites xFe – (1-x) ($0.3V_2O_5$ – $0.2MoO_3$ – 0.4CdO – 0.1ZnO) with different values of x at various heat treatment (HT) hours (1h, 3h and 5h) along with as prepared condition.

Samples	P (N)	Hv (GPa)	H_v for 1hHT (GPa)	Plateau Region For 1h HT	H_v for 3h HT (GPa)	Plateau Region For 3h HT	H_v for 5h HT(GPa)	Plateau Region For 5h HT
x= 0	0.049	1.0032	1.3328	3.2624-3.7746	2.3204	4.2109-4.5693	2.3541	4.1994-4.5831
	0.098	1.3063	1.8782		2.9587		3.0046	
	0.245	1.9167	2.6738		3.7303		3.7849	
	0.49	2.4952	3.2624		4.2109		4.1994	
	0.98	3.0763	3.7746		4.5693		4.5831	
x= 0.05	0.049	1.1353	1.5277	3.5189-4.054	2.0166	4.59-4.9436	2.5258	4.6228-5.0139
	0.098	1.7927	2.1817		3.1239		3.6178	
	0.245	2.3061	2.8322		3.9935		3.9897	
	0.49	2.7836	3.5189		4.59		4.6228	
	0.98	3.3666	4.054		4.9436		5.0139	
x= 0.1	0.049	1.3459	1.6832	4.4874-4.8446	2.2551	5.477-5.6918	3.1241	6.1344-6.3188
	0.098	1.8771	2.55		3.7705		4.8874	
	0.245	2.6746	3.5732		4.7534		5.3367	
	0.49	3.2679	4.4874		5.477		6.1344	
	0.98	3.7591	4.8446		5.6918		6.3188	
x= 0.2	0.049	1.5046	1.8425	4.7131-5.2879	3.6011	6.432-6.6436	3.6665	6.5416-6.7823
	0.098	2.15397	2.9214		5.2421		5.3141	
	0.245	2.8345	3.9015		5.8777		5.9999	
	0.49	3.5167	4.7131		6.432		6.5416	
	0.98	4.0357	5.2879		6.6436		6.7823	
x= 0.3	0.049	1.671	2.3241	5.7917-5.6791	5.4225	10.2147-10.2965	5.1794	10.0016-10.2579
	0.098	2.5422	4.3044		8.4107		7.9097	
	0.245	3.5694	4.8421		8.7703		8.881	
	0.49	4.0357	5.7917		10.2147		10.0016	
	0.98	4.8676	5.6791		10.2965		10.2579	
x= 0.4	0.049	1.7336	2.2694	5.7687-5.8082	5.6128	9.9597-10.4453	5.6548	10.0226-10.5329
	0.098	2.8919	4.0033		8.0944		8.3032	
	0.245	3.898	4.8571		8.9559		9.0829	
	0.49	4.923	5.7687		9.9597		10.0226	
	0.98	5.2321	5.8082		10.4453		10.5329	

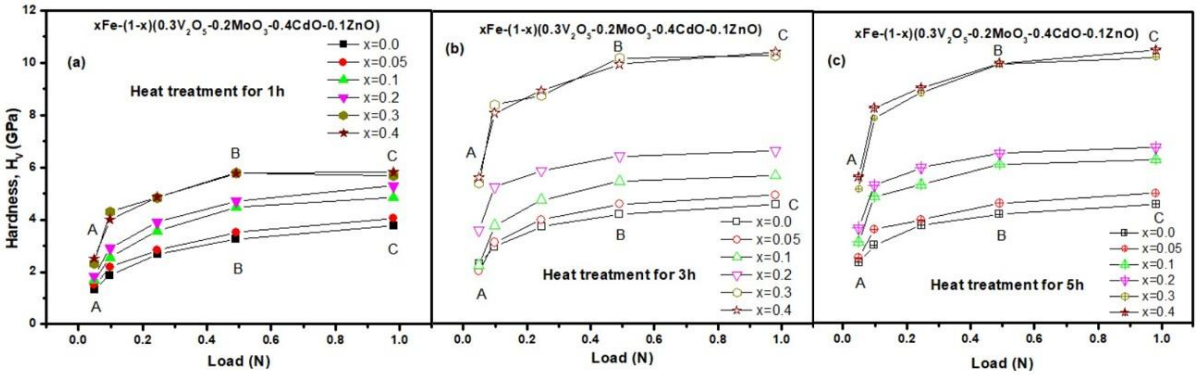

Fig. 4.3.7: The variations of H_v with various loads for the prepared system xFe – (1-x) ($0.3V_2O_5$ – $0.2MoO_3$ – 0.4CdO – 0.1ZnO) with different values of x for (a) 1h, (b) 3h and (c) 5h heat treatment condition.

The elastic modulus (E) values for each heat treatment sample (1h, 3h, and 5h) at different loads are presented in Table 4.3.9. The glass nanocomposites' elastic modulus (E) values were calculated using the Vickers hardness values [134-137]. The data shows that the elastic modulus increases with both the applied load and the Fe concentration in the samples. Forx=0.0 at a load of 0.049 N, the elastic modulus is 109.24095 GPa, whereas, for x=0.4 at the same load, it is 186.01 GPa after 1 h heat treatment, indicating an increase of about 72.27%. At a higher load of 0.980 N, the elastic modulus for x=0.0 is 375.65 GPa, while for x=0.4, it is 863.31 GPa after 5 h heat treatment condition, showing an enhancement of approximately 129.82 %. The data shows that the elastic modulus increases with both the applied load and the Fe concentration in the heat treatment samples [161].

Table 4.3.10 presents the yield strength (Y) values for each heat-treated sample (1h, 3h, and 5h HT) at various loads. These yield strength values were calculated from the Vickers hardness values [134-137]. The results show a trend similar to that of the elastic modulus. The yield strength increases with higher Fe content and applied load, reflecting the enhanced ability of the material to withstand permanent deformation. At a load of 0.049 N, the yield strength for x=0.0 is 0.44 GPa, whereas, for x=0.4, it is 0.77 GPa, after 1 h heat treatment condition showing an increase of about 70.27 %. At a load of 0.980 N, the yield strength for x=0.0 is 1.53 GPa, and for x=0.4, it is 3.51 GPa, after a 5 h heat treatment condition reflecting an enhancement of approximately 129.82 %. The rise in yield strength with increasing Fe

concentration indicates that Fe doping notably enhances the material's resistance to yielding and permanent deformation, making it crucial for structural applications [48, 161].

The shear modulus (G) values for each heat treatment sample (1h, 3h, and 5h) at different loads are presented in Table 4.3.11. The shear modulus values were derived from the Vickers hardness values, and the results indicate a similar trend to that observed for the elastic modulus [134-137]. The shear modulus increases with higher Fe content and applied load, reflecting the enhanced ability of the material to withstand permanent deformation. At a load of 0.049 N, the shear modulus for x=0.0 is 8.82649 GPa, whereas for x=0.4, it is 15.02914 GPa, after 1 h heat treatment condition showing an increase of about 70.27 %. At a load of 0.980 N, the shear modulus for x=0.0 is 30.35166 GPa, and for x=0.4, it is 69.75430 GPa, after a 5 h heat treatment condition reflecting an enhancement of approximately 129.82 %.

XRD analysis (Details in section 4.1.5 of chapter 4) reveals the presence of crystalline phases such as $FeVO_4$, and $Cd_2V_2O_7$ in the samples. These phases contribute to the enhanced hardness, elastic modulus, yield strength, and shear modulus of the materials. The formation of $FeVO_4$ and $Cd_2V_2O_7$ phases contribute to the enhanced hardness, elastic modulus, yield strength, and shear modulus of the materials. XRD analysis reveals the presence of crystalline phases, and observed improvements in hardness and other mechanical properties.

Table: 4.3.9 The calculated elastic modulus (E) values for xFe – (1-x) ($0.3V_2O_5$ – $0.2MoO_3$ – 0.4CdO – 0.1ZnO) system at different heat treatment (HT) condition along with as prepared condition.

Samples	P (N)	ElasticModulus (E) in GPa			
		As Prepared	1hr HT	3hr HT	5hr HT
x= 0	0.049	82.22699	109.24095	190.18811	192.95028
	0.098	107.07000	153.94385	242.50541	246.26753
	0.245	157.10130	219.15401	305.74844	310.22365
	0.49	204.51736	267.39772	345.14010	344.19752
	0.98	252.14791	309.37943	374.51582	375.64692
x= 0.05	0.049	93.055359	125.21564	165.28759	207.02341
	0.098	146.94393	178.81977	256.04578	296.52755
	0.245	189.02384	232.13702	327.32124	327.00978
	0.49	228.15372	288.42136	376.21247	378.90087
	0.98	275.94360	332.28003	405.19476	410.95679
x= 0.1	0.049	110.31542	137.96096	184.83589	256.06217
	0.098	153.85837	209.00693	309.04338	400.58841
	0.245	219.22324	292.87198	389.60530	437.41461
	0.49	267.85102	367.80301	448.91409	502.79689
	0.98	308.11334	397.08037	466.51985	517.91096
x= 0.2	0.049	123.32916	151.01775	295.15876	300.51917
	0.098	176.54698	239.44817	429.66086	435.56224
	0.245	232.32657	319.78060	481.75686	491.77280
	0.49	288.24476	386.30217	527.18923	536.17243
	0.98	330.78395	433.41479	544.53271	555.90105
x= 0.3	0.049	136.96127	190.49137	444.44708	424.52175
	0.098	208.37304	352.80369	689.37041	648.30670
	0.245	292.56515	396.87546	718.84448	727.91784
	0.49	366.56713	474.70800	837.23256	819.76614
	0.98	398.97308	465.47891	843.93718	840.77339
x= 0.4	0.049	142.09520	186.00797	460.04473	463.48720
	0.098	237.03434	328.12448	663.44535	680.55933
	0.245	319.49864	398.10492	734.05691	744.46627
	0.49	403.51040	472.82284	816.33187	821.48738
	0.98	428.84122	476.06040	856.13335	863.31335

Table: 4.3.10 The calculated yield strength (Y) values for xFe – (1-x) $(0.3V_2O_5 – 0.2MoO_3 – 0.4CdO – 0.1ZnO)$ system at different heat treatment (HT) conditions along with as prepared condition.

Samples	P (N)	Yield Strength (Y) in GPa			
		As Prepared	1hr HT	3hr HT	5hr HT
x= 0	0.049	0.33440	0.44427	0.77347	0.78470
	0.098	0.43543	0.62607	0.98623	1.00153
	0.245	0.63890	0.89127	1.24343	1.26163
	0.49	0.83174	1.08747	1.40363	1.39980
	0.98	1.02544	1.25820	1.52310	1.52770
x= 0.05	0.049	0.37844	0.50923	0.67220	0.84193
	0.098	0.59759	0.72723	1.04130	1.20593
	0.245	0.76873	0.94407	1.33117	1.32990
	0.49	0.92786	1.17297	1.53000	1.54093
	0.98	1.12222	1.35133	1.64787	1.67130
x= 0.1	0.049	0.44863	0.56107	0.75170	1.04137
	0.098	0.62571	0.85000	1.25683	1.62913
	0.245	0.89154	1.19107	1.58447	1.77890
	0.49	1.08931	1.49580	1.82567	2.04480
	0.98	1.25305	1.61487	1.89727	2.10627
x= 0.2	0.049	0.50156	0.61417	1.20037	1.22217
	0.098	0.71799	0.97380	1.74737	1.77137
	0.245	0.94483	1.30050	1.95923	1.99997
	0.49	1.17224	1.57103	2.14400	2.18053
	0.98	1.34524	1.76263	2.21453	2.26077
x= 0.3	0.049	0.55700	0.77470	1.80750	1.72647
	0.098	0.84742	1.43480	2.80357	2.63657
	0.245	1.18981	1.61403	2.92343	2.96033
	0.49	1.49077	1.93057	3.40490	3.33387
	0.98	1.62256	1.89303	3.43217	3.41930
x= 0.4	0.049	0.57788	0.75647	1.87093	1.88493
	0.098	0.96398	1.33443	2.69813	2.76773
	0.245	1.29935	1.61903	2.98530	3.02763
	0.49	1.64101	1.92290	3.31990	3.34087
	0.98	1.74403	1.93607	3.48177	3.51097

Table: 4.3.11 The calculated shear modulus (G) values for xFe – (1-x) $(0.3V_2O_5 – 0.2MoO_3 – 0.4CdO – 0.1ZnO)$systems at different heat treatment (HT) condition along with as prepared condition.

Samples	P (N)	Shear Modulus (G) in GPa			
		As Prepared	1hr HT	3hr HT	5hr HT
x= 0	0.049	6.643807	8.82649	15.36689	15.59007
	0.098	8.651081	12.43841	19.59404	19.89801
	0.245	12.69353	17.70728	24.70397	25.06556
	0.49	16.52467	21.60530	27.88675	27.81060
	0.98	20.37314	24.99735	30.26026	30.35166
x= 0.05	0.049	7.518721	10.11722	13.35497	16.72715
	0.098	11.87283	14.44834	20.68808	23.95894
	0.245	15.27282	18.75629	26.44702	26.42185
	0.49	18.43445	23.30397	30.39735	30.61457
	0.98	22.29579	26.84768	32.73907	33.20464
x= 0.1	0.049	8.913306	11.14702	14.93444	20.68940
	0.098	12.4315	16.88742	24.97020	32.36689
	0.245	17.71288	23.66358	31.47947	35.34238
	0.49	21.64192	29.71788	36.27152	40.62517
	0.98	24.89505	32.08344	37.69404	41.84636
x= 0.2	0.049	9.964794	12.20199	23.84834	24.28146
	0.098	14.26471	19.34702	34.71589	35.19272
	0.245	18.77161	25.83775	38.92517	39.73444
	0.49	23.2897	31.21258	42.59603	43.32185
	0.98	26.7268	35.01921	43.99735	44.91589
x= 0.3	0.049	11.06625	15.39139	35.91060	34.30066
	0.098	16.8362	28.50596	55.70000	52.38212
	0.245	23.63879	32.06689	58.08146	58.81457
	0.49	29.61802	38.35563	67.64702	66.23576
	0.98	32.23637	37.60993	68.18874	67.93311
x= 0.4	0.049	11.48106	15.02914	37.17086	37.44901
	0.098	19.15199	26.51192	53.60530	54.98808
	0.245	25.81497	32.16623	59.31060	60.15166
	0.49	32.60298	38.20331	65.95828	66.37483
	0.98	34.64967	38.46490	69.17417	69.75430

4.3.5 Analysis of Theoretical Models of Microhardness at different heat treatment condition

Theoretical models were established to investigate the ISE and the reverse ISE (RISE) behaviours of materials [48-50]. These models are also crucial for explaining the structural and mechanical behavior of glass nanocomposites under different loading conditions.

From the microhardness result, maximum hardness values were estimated from the present glass nanocomposite samples for higher Fe concentrations (x=0.3 and 0.4). For higher concentrations of Fe (x=0.3 and 0.4), the graphs (Fig. 4.3.7 a-c) of microhardness variation under different loads (1h, 3h, and 5h) clearly indicate that there is no significant difference in microhardness values between the 3h and 5 heat treatment duration. Samples x=0.3, as well as x=0.4 sample, can be selected for further studies of the ISE behaviours of the samples.

In the present study, the following models were used to investigate the ISE phenomenon in Vickers microhardness values of the present glassy samples (x= 0.4) subjected to different heat treatment conditions (1h, 3h, and 5h).

4.3.5.1 Meyer's law

Mayer's law is already discussed in section 2.11.4.1 of chapter 2 and section 4.3.3.1 of chapter 4. The ln P vs ln d plot has been prepared to investigate the indentation size effect of the present glassy system (x=0.4) shown in Fig. 4.3.2. Table 4.3.2 shows that the value of n exceeds during as prepared condition as well as different heat treatment condition (1h, 3h, and 5h HT). Due to these values of n, for all conditions, glassy nanocomposite-prepared samples (x=0.4) have been considered to follow RISE behavior [46, 48, 146, 150].

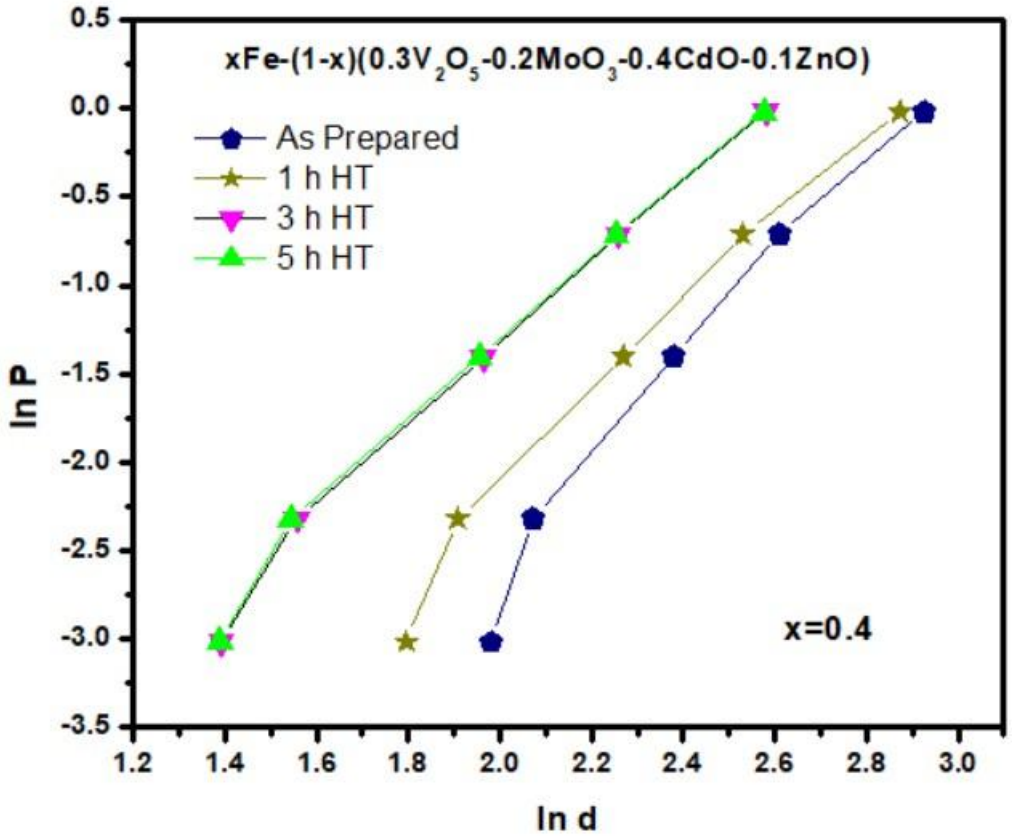

Fig. 4.3.8: The changes of ln P with ln d for the prepared system xFe – (1-x) ($0.3V_2O_5$ – $0.2MoO_3$ – 0.4CdO – 0.1ZnO) where x= 0.4, along with different heat treatment (HT) condition using Meyer's law.

Table 4.3.12: Experimental fitting parameters data according to Meyer's law for the prepared system xFe – (1-x) ($0.3V_2O_5$ – $0.2MoO_3$ – 0.4CdO – 0.1ZnO) where x= 0.4 along with various heat treatment (HT).

Samples (x=0.4)	Mayer index (n)	lnA (GPa)
As Prepared	3.08173	-8.81079
1h HT	2.68499	-7.60446
3h HT	2.44903	-6.27024
5h HT	2.43881	-6.23526

4.3.5.2 Elastic/plastic deformation approach

In this present study, the EPD approach has been used for clarifying the ISE and RISE behaviors in glass nanocomposite sample (x=0.4) during as prepared condition as well as different heat treatment conditions (1h, 3h, and 5h HT) [142, 151]. The relationship between $P^{1/2}$ and dp was analyzed (Figure 4.3.9), and the constants were derived from the best-fit straight lines in the $P^{1/2}$ versus d_p plot, as summarised in Table 4.3.13. The values of elastic deformation (d_e) were found to range from -0.228 to -0.090 μm, indicating a negative nature and thereby confirming the RISE behavior of the nano glassy composite (x=0.4) [142, 151]. The negative values of d_e are critical because they highlight the material's tendency to exhibit increased hardness with increasing load, contrary to the typical ISE behavior where hardness decreases with increased load [142].

The microhardness values derived from this model (Table 4.3.13) show significant deviations from the experimentally observed Vickers microhardness values. For instance, the EPD model predicts a microhardness of 8.1562 GPa for as prepared condition, whereas after the different heat treatment conditions of 1h, 3h, and 5h, Vickers microhardness ranges from 8.7725, 12.6215, and 12.6582 respectively.

Furthermore, the EPD model's ability to explain the RISE behavior is linked to the negative elastic deformation values. This behavior contrasts with typical ISE behavior observed in other materials, where positive elastic deformation values indicate a decrease in hardness with increasing load [48, 142, 151]. The negative values suggest that the present glass nanocomposites sample for higher Fe concentration (x=0.4) exhibit unique deformation mechanisms, possibly due to the specific nature of Fe doping and its effect on the glass matrix [161].

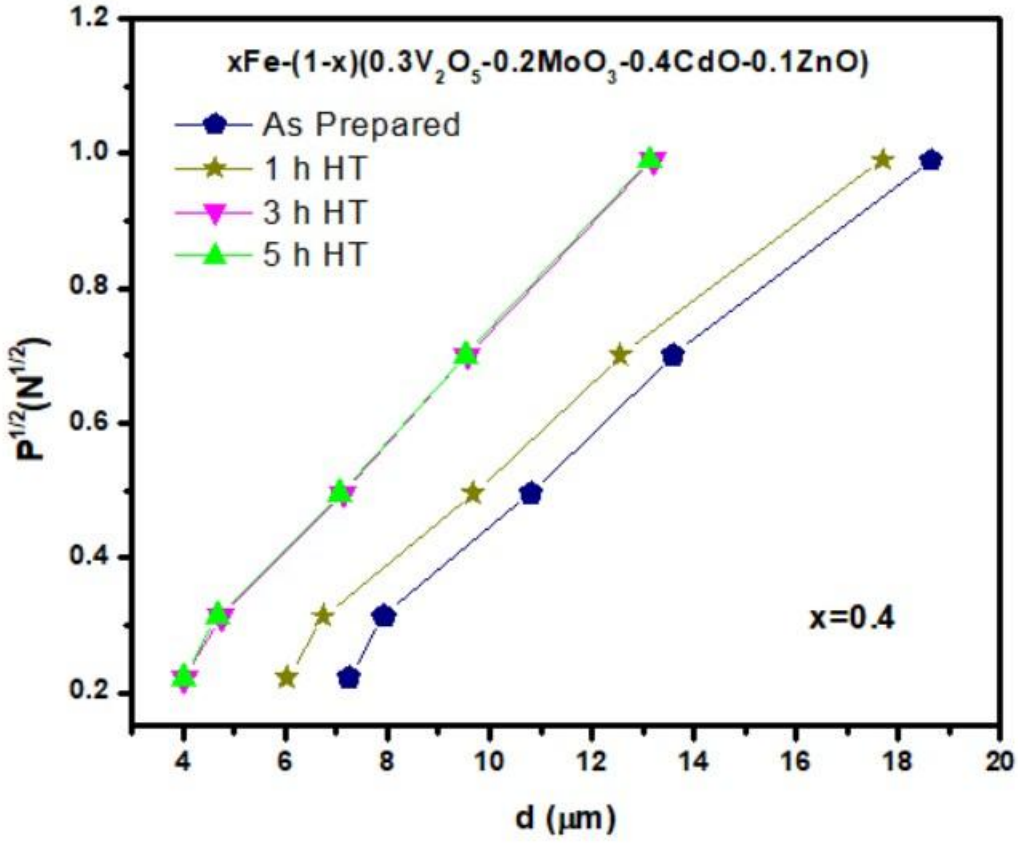

Fig. 4.3.9: Graphs of $P^{1/2}$ over d for the prepared system xFe – (1-x) ($0.3V_2O_5$ – $0.2MoO_3$ – 0.4CdO – 0.1ZnO) where x= 0.4, along with various heat treatment (HT) condition using EPD Model.

Table 4.3.13: Experimental fitting parameters data according to the EPD model for the prepared system xFe – (1-x) ($0.3V_2O_5$ – $0.2MoO_3$ – 0.4CdO – 0.1ZnO) for x= 0.4 along with various heat treatment (HT) condition.

Samples (x=0.4)	$A_2^{1/2}x10^3(N/\mu m^2)$	d_e (µm)	H_{EPD} (GPa)
As Prepared	66.32	-0.228	8.1562
1h HT	68.78	-0.138	8.7725
3h HT	82.5	-0.093	12.6215
5h HT	82.62	-0.090	12.6582

4.3.5.3 Proportional sample resistance model

The PSR model is a key tool for analyzing both load-dependent and load-independent microhardness in materials, especially within nanocomposite glass systems [150, 152-154].

The experimental fitting parameters (A and B, derived from Eq. 2.8 of Chapter 2) from the PSR model, tabulated in Table 4.3.14, highlight significant observations. The negative values of A for x=0.4 sample during as prepared condition as well as after different heat treatment conditions (1h, 3h, and 5h HT) confirm the RISE behaviour, indicating that microhardness increases with increasing load [152, 155].

The calculated load-independent Vickers microhardness values for the PSR model (H_{vPSR}) using Eq. 2.9 of Chapter 2 has been summarised in Table 4.3.14, which are significantly higher than the actual measured Vickers microhardness values (H_v) at the saturation zone. For instance, the x=0.4 sample after 1h heat treatment condition has a $(H_v)_{PSR}$ of 7.3619 GPa compared to an actual H_v range of 4.923-5.2321 GPa. Similarly, the 5h heat treatment sample exhibits a $(H_v)_{PSR}$ of 12.3317 GPa, whereas the actual H_v ranges from 10.0226-10.5329 GPa. This significant disparity indicates that although the PSR model offers a theoretical basis for understanding hardness, it may not adequately reflect the intricate load-dependent behavior observed in experimental studies [153-154].

The PSR model's dependence on intrinsic structural factors and indenter orientation significantly influences the measured hardness values. The negative A values, indicative of RISE behavior, imply that the prepared glass nanocomposites predominantly experience plastic deformation with limited elastic recovery [51, 135]. This behavior aligns with the observed microstructural changes resulting from different heat treatment conditions.

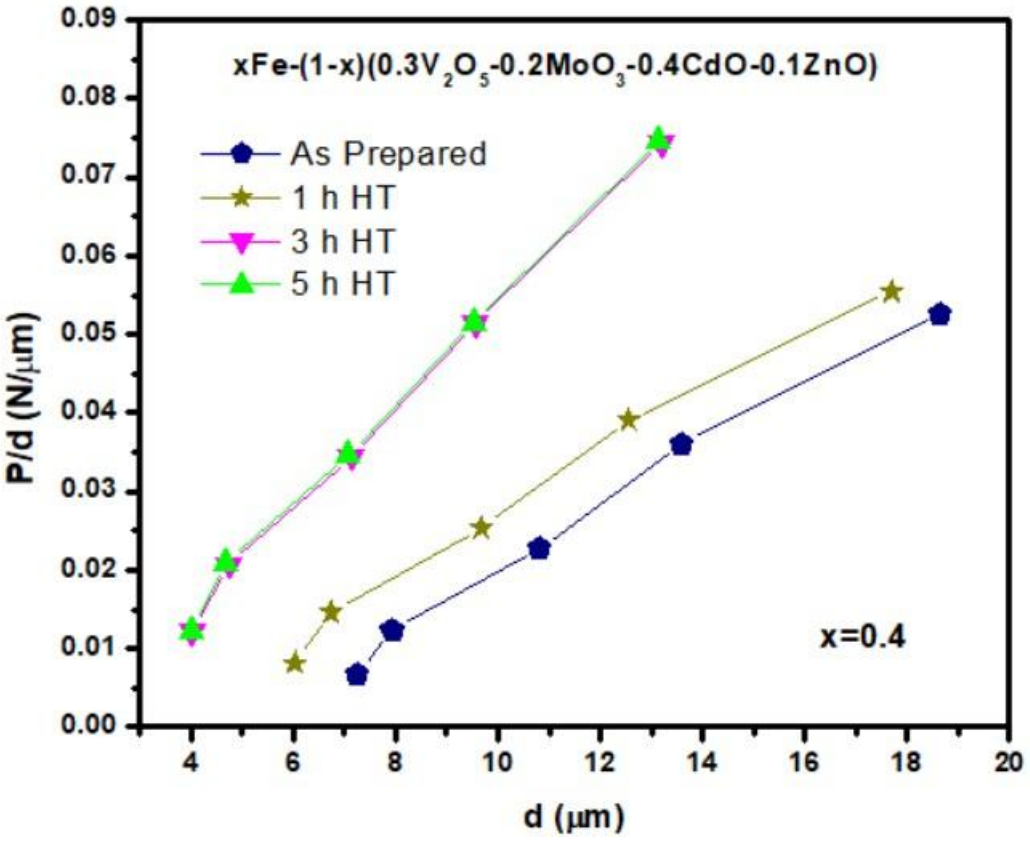

Fig. 4.3.10: Graph of P/d versus d for the prepared system xFe – (1-x) ($0.3V_2O_5$ – $0.2MoO_3$ – 0.4CdO – 0.1ZnO) where x= 0.4, along with various heat treatment (HT) condition using PSR model.

Table 4.3.14: Experimental fitting parameters data according to PSR model for the prepared system xFe – (1-x) ($0.3V_2O_5$ – $0.2MoO_3$ – 0.4CdO – 0.1ZnO) where x= 0.4 along with various heat treatment (HT) condition.

Samples (x=0.4)	$Ax10^{-3}$ (N/μm)	$Bx10^{-4}$ ($N/\mu m^2$)	H_{PSR} (GPa)
As Prepared	-20.11	39.7	7.3619
1h HT	-13.45	39.8	7.3805
3h HT	-12.6	66.2	12.2761
5h HT	-12.3	66.5	12.3317

4.3.5.4 Hays Kendall approach

The HK model is the most important approach to understanding the mechanical behavior and load-independent microhardness parameters of materials [145]. This model

accounts for both plastic and elastic deformation when materials are subjected to a minimum test load. Fig. 4.3.11 showed the plots of the applied loads (P) versus the square of the diagonal length (d^2) for the prepared sample x= 0.4, along with various heat treatment (HT) conditions using the HK model. The plot helps in determining the values of A_3 and W from the best-fitted straight line. A_3 and W have already been discussed in Eq. 2.10 of Chapter 2. The negative values of W observed in Table 4.3.15 indicate that the effective load applied is slightly more than the actual applied load, suggesting that plastic deformation starts at a lower load than initially expected [145].

The load-independent Vickers microhardness values $(H_v)_{HK}$ are determined using Eq. 2.12 in the section of Chapter 2. These values are summarised in Table 4.3.15. exhibit a significant increase after higher heat treatment duration. The HK model highlights the significant role of heat treatment in enhancing the material's hardness and structural integrity, contributing to its improved load-bearing capacity [48].

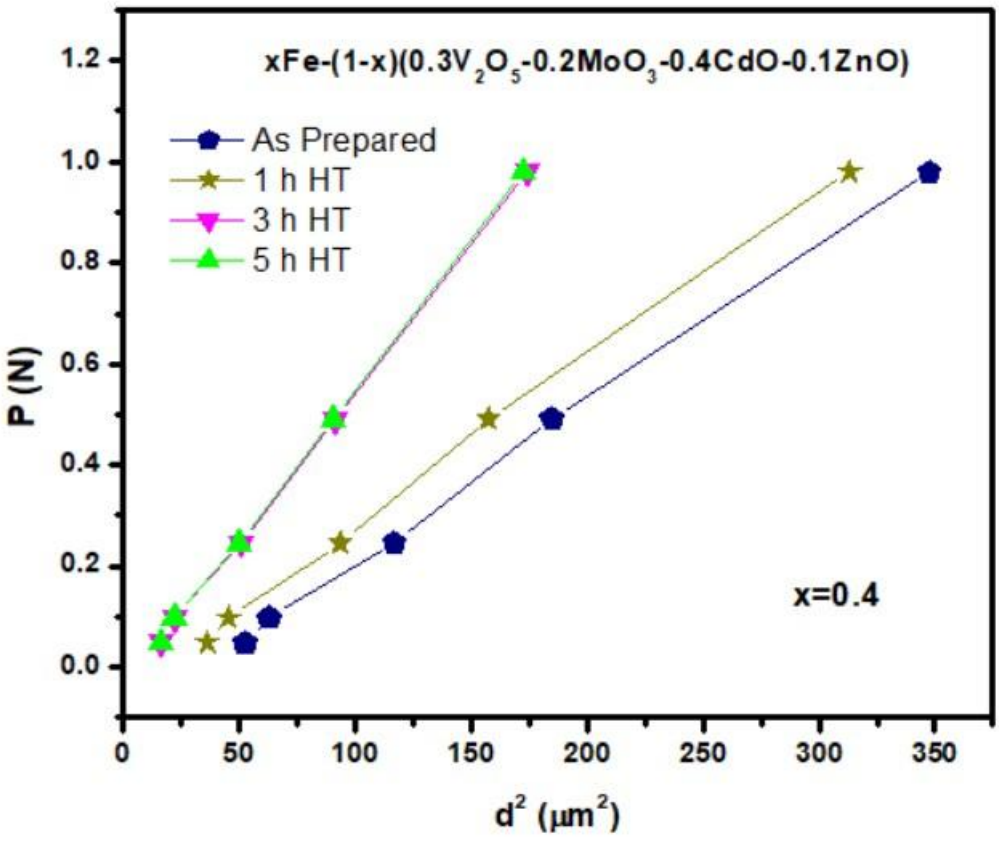

Fig. 4.3.11: Plots of P versus d^2 for the prepared system xFe – (1-x) ($0.3V_2O_5$ – $0.2MoO_3$ – 0.4CdO – 0.1ZnO) where x= 0.4, along with various heat treatment (HT) condition using HK model.

Table 4.3.15: Experimental fitting parameters data according to HK model for the prepared system xFe – (1-x) ($0.3V_2O_5 – 0.2MoO_3 – 0.4CdO – 0.1ZnO$) where x= 0.4 along with various heat treatment (HT) condition.

Samples (x=0.4)	$A_3 \times 10^{-3}$ ($N/\mu m^2$)	W_{HK} (N)	H_{HK} (GPa)
As Prepared	3.15	-0.108	5.8413
1h HT	3.35	-0.060	6.2122
3h HT	5.87	-0.044	10.8853
5h HT	5.91	-0.042	10.9595

4.3.5.5 Indentation-induced cracking model

The IIC model developed by Li and Bradt, provides a comprehensive framework to analyse the mechanical properties of materials, particularly those exhibiting RISE behaviour [155, 156-159].

K and m are constants that are independent of load, as explained in Eq. 2.14 of Chapter 2. The values of the constants evaluated from Fig. 4.3.12 of plots of Variation of $\ln H_v$with $\ln(P^{5/3}/d^3)$. Since m < 0.6 for x= 0.4 along with various heat treatment (HT) conditions. It is confirmed that the glass nanocomposite sample (x=0.4) exhibits RISE behavior. This behaviour indicates that as the applied load decreases, the hardness increases, a characteristic typically associated with significant plastic deformation before fracture [156-158]. The increase in K correlates well with the observed microhardness values (H_v), indicating that the IIC model effectively describes the hardness behaviour of these materials.

To validate the IIC model, it is essential to compare the microhardness values from various models (EPD, PSR, HK, and IIC) with the experimental Vickers microhardness (H_v) in the plateau region. The experimental Vickers microhardness results at the plateau region of the prepared system for x= 0.4 and the theoretical microhardness valuescalculated using EPD, PSR, HK, and IIC models along with various heat treatment (HT) conditions have been estimated in Table 4.3.17.

The IIC model values (H_{VIIC}) closely match the experimental Vickers microhardness (H_V), indicating its robustness in capturing the mechanical properties of the Fe-doped glass nanocomposite sample of x=0.4. The slight variations between the experimental and theoretical values suggest that while the IIC model is effective, it might still require some adjustments for perfect alignment with experimental data. As the heat treatment hour increases, both the experimental and theoretical hardness values show an upward trend. This indicates that higher

heat treatment strengthens the glass matrix, enhancing its resistance to deformation. The trend is compatible across all models, affirming the positive impact of heat treatment on the mechanical properties.

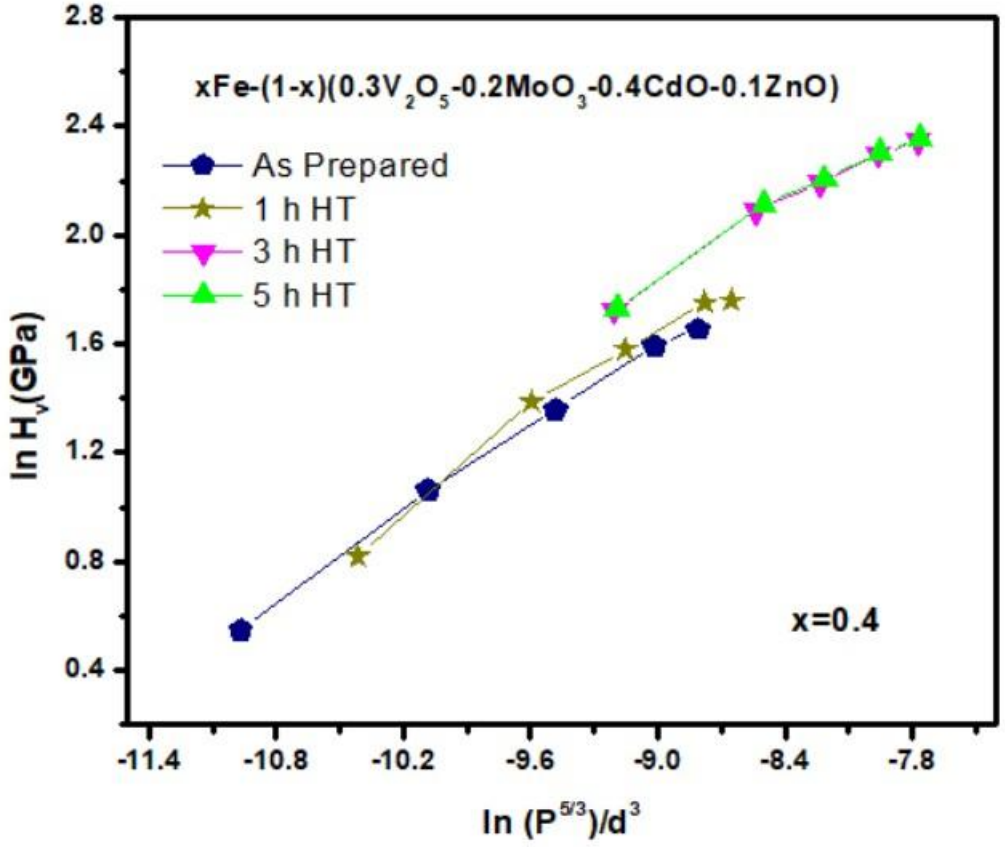

Fig. 4.3.12: Plots of Variation of $\ln H_v$ with $\ln(P^{5/3}/d^3)$, for xFe – (1-x) $(0.3V_2O_5 – 0.2MoO_3 – 0.4CdO – 0.1ZnO)$ prepared system where x= 0.4, along with various heat treatment (HT) condition using IIC model.

Table 4.3.16: Experimental fitting parameters data according to the IIC model for xFe – (1-x) $(0.3V_2O_5 – 0.2MoO_3 – 0.4CdO – 0.1ZnO)$prepared system where x= 0.4, along with various heat treatment (HT) condition.

Samples (x=0.4)	**m**	**lnK ($N^{(3-5m)/3}/\mu m^{(2-3m)}$**	**$(H_v)_{IIC}$ (GPa)**
As Prepared	0.516	6.242	4.9012
1h HT	0.518	6.294	5.7368
3h HT	0.521	6.441	9.9180
5h HT	0.523	6.449	9.9779

Table 4.3.17: The experimental Vickers microhardness results at the plateau region of the prepared system xFe – (1-x) $(0.3V_2O_5 – 0.2MoO_3 – 0.4CdO – 0.1ZnO)$ where x= 0.4 and the theoretical microhardness values calculated using EPD, PSR, HK, and IIC models along with various heat treatment (HT) condition.

Samples (x=0.4)	$(H_v)_{EPD}$ GPa)	$(H_v)_{PSR}$ (GPa)	$(H_v)_{HK}$ (GPa)	$(H_v)_{IIC}$ GPa)	H_v(GPa)
As Prepared	8.1562	7.3619	5.8413	4.9012	4.923-5.2321
1h HT	8.7725	7.3805	6.2122	5.7368	5.7687-5.8082
3h HT	12.6215	12.2761	10.8853	9.9180	9.9597-10.4453
5h HT	12.6582	12.3317	10.9595	9.9779	10.0226-10.5329

4.3.6 Conclusion

Microhardness and other mechanical properties of xFe – (1-x) $(0.3V_2O_5 – 0.2MoO_3 – 0.4CdO – 0.1ZnO)$ where x= 0.0, 0.05, 0.1, 0.2, 0.3 and 0.4 along with various heat treatment (HT) condition were estimated applying the Vickers indenters. These results can be summarised as follows:

- Microhardness values are increased with increasing applied load for all prepared glassy samples at room temperature and during heat treatment at 600^oC for 1h, 3h, and 5h. At low load conditions, the microhardness values are increased rapidly, and at high load, they increase gradually. Variation of microhardness of all samples also increased with increasing Fe content in the samples. The Vickers hardness values show a substantial increase from 4.1994-4.5831GPa for x=0.0 to 10.0226-10.5329 GPa for x=0.4, at 5h heat treatment condition, indicating higher mechanical strength and resistance to deformation. The higher Fe concentration promoted rapid nucleation of $FeVO_4$, $Zn_3V_2O_8$, and $Cd_2V_2O_7$ phases. This increase was attributed to interlocking crystalline network formation. The microstructure became more rigid and resistant to deformation due to the synergistic effects of multiple crystalline phases. Prolonged heat treatment led to further crystallite growth and the development of a predominantly polycrystalline structure. While the overall hardness remained high, minor phase segregation and coarsening in the high Fe concentration samples limited any further significant improvement.
- The elastic modulus (E), yield strength (Y), and shear modulus (G) were measured and observed to increase with increasing Fe content in the glassy samples reaching their

maximum values for x=0.4 sample. Additionally, these properties (E, Y, and G) were found highest after 3h and 5h heat treatments, both low and high loading conditions.

- Investigated values of Vickers micro-hardness were analyzed using different theoretical approaches including Meyer's law, EPD model, EPD model, HK approach, and IIC model. All samples exhibited RISE behavior, which is also supported by these models. Among these, the IIC model was found to be the only successful model for describing the applied load with indentation data across all prepared samples. Additionally, the Vickers micro-hardness values of the sample with higher Fe concentration (x=0.4) after a 5h heat treatment were analyzed using the same theoretical models. Once again, all samples showed RISE behavior, which was supported by these models. The IIC model is the only effective model to describe the applied load and indentation data for the x=0.4 sample at the 5h heat treatment condition.

CHAPTER–5

Conclusions & Future Scopes

Contents

Chapter-5

5.1 Conclusions

In the present investigation, a glass nanocomposite system with composition xFe – (1-x) ($0.3V_2O_5$ – $0.2MoO_3$ – 0.4CdO – 0.1ZnO) where x= 0.0, 0.05, 0.1, 0.2, 0.3 and 0.4 have been successfully developed through melt quenching method and the influence of Fe concentration. The structural behaviour of the present glassy system has been characterized by different techniques like FT-IR, DSC, XRD, FE-SEM. The electrical and mechanical properties of the system have been studied. Some major conclusions of the present investigation are summarized below.

- **Physical and microstructural Characterization**

- The density in the present study increases as Fe concentration increases, while V_2O_5 modifies the glass network and increases its compactness. Changes in density and molecular weight determine molar volume changes. In addition to an increase in molecular weight and density, the molar volume increases with an increase in Fe (x) content.

- FTIR analysis reveals that the higher Fe concentrations should result in lower energy requirements to vibrate the Zn-O and V-O bands. This result leads us to infer that the present glass system with a higher Fe content is unstable due to acoustic phonon vibrations. This conclusion is supported by XRD analysis results that show an increase in the average dislocation density and a decrease in structure stability with increasing Fe content.

- In DSC analysis, glass transition temperature (Tg) has been evaluated and correlated with the different Fe concentrations. The gradual increase in T_g with Fe content reflects the interplay between compositional changes and the structural rearrangements offering valuable insights into the thermal behavior of the glass nanocomposites.

- Different crystal phases have been developed, which were identified through XRD analysis. The crystal phases of zinc vanadium oxide (ZnV_2O_6), $Zn_2V_2O_7$, and $Zn_3V_2O_8$ are observed as major phases in all prepared samples as well as heat-treated samples (x=0.4). The peak intensity of $Zn_3V_2O_8$ is higher in the x=0.4 sample than in other samples. Characteristic peaks of cadmium vanadium oxide ($Cd_2V_2O_7$) and vanadium

molybdenum oxide (V_2MoO_8) appear in all prepared samples. The Debye–Scherrer equation has been used to estimate the average crystallite sizes, microstrain, and also dislocation density has been estimated. The heat-treated sample with x=0.4 shows an increase in the intensity of peaks corresponding to iron vanadium oxide ($FeVO_4$) under various heat treatment durations (1 h, 3 h, and 5 h). Additionally, crystal phases of zinc vanadium oxide ($Zn_3V_2O_8$) are observed in the same sample (x=0.4) after 5 h of heat treatment, with their intensity being higher compared to the untreated sample (x=0.4).

- FE-SEM has been used to examine the morphologies of the glass samples (x=0.0, 0.05, 0.1, 0.2, 0.3, and 0.4) along with various heat treatment conditions (1h, 3h, and 5h). The plate-like crystals have been observed in the microstructure in the Fe undoped sample (x=0.0). The plate-like crystals disperse throughout the glass matrix. The micrographs show a reduction in particle size as the composition changes from x=0.0 to x=0.4 under the same heat treatment duration of 5 h. Furthermore, the size, shape, and variation of particles within the microstructure decrease consistently from the x=0.0 sample to the x=0.4 sample under identical heat treatment conditions. For the x=0.4 sample, the variation in crystal sizes and the overall distribution of crystals remains relatively uniform across different heat treatment durations (1 h, 3 h, and 5 h).

- **Electrical Properties**

- Fe undoped (x=0.0) as well as Fe doped (x= 0.05, 0.1, 0.2, 0.3 and 0.4) nano glassy system xFe – (1-x) ($0.3V_2O_5 – 0.2MoO_3 – 0.4CdO – 0.1ZnO$) have been investigated the electrical properties which were prepared through melt quenched method. FTIR reports indicate that to make a vibration in the Mo-O and Zn-O bands, minimal energy is required so that an acoustic phonon contribution is induced when the Fe content increases. The larger the acoustic vibration, the more unstable the current system, which contains more Fe. It has been revealed that the DC conductivity of the present glassy system increases with temperature. XRD result shows that on the evolvement of different nano phases, structural modification should emerge. This limited lattice distortion results from the structural arrangement in the current system when Fe concentration is adjoined. When the present system is steadily increased with Fe, this type of environment charges a conversion of conduction technique from large to small hoping polaron.

- Both DC and AC conductivity have been increased as Fe is doped, which also shows a similar nature. The modified CBH model has been deployed to state the nature of frequency exponent (S) corresponds to temperature (T) in the system and the prevalent conduction method is anticipated in the present system.

- It has also been found that the activation energy for DC conductivity (σ_{dc}), as well as hopping frequency (ω_H), are almost the same for all prepared samples (x=0.0, 0.05, 0.1, 0.2, 0.3, and 0.4) of the present glassy system.

- AC conductivity scaling phenomena have indicated that the common relaxation mechanism of charge carriers/ polarons is temperature-independent but strongly dependent on the composition or structure of the presently glassy system.

- **Mechanical Properties**

Microhardness and other mechanical properties of xFe – (1-x) ($0.3V_2O_5 – 0.2MoO_3 – 0.4CdO – 0.1ZnO$) where x= 0.0, 0.05, 0.1, 0.2, 0.3 and 0.4 along with various heat treatment (HT) condition were measured applying the Vickers indenters. These results can be outlined as follows:

- Microhardness values are increased with increasing applied load for all prepared glassy samples at room temperature and during heat treatment at 600^{o}C for 1h, 3h, and 5h. At low load conditions, the values of microhardness are increased rapidly, and at high load, increase gradually. Variation of microhardness of all samples also increased with increasing Fe content in the samples. The Vickers hardness values show a substantial increase from 4.1994-4.5831GPa for x = 0.0 to 10.0226-10.5329 GPa for x = 0.4, at 5h heat treatment condition, indicating higher mechanical strength and resistance to deformation. The higher Fe concentration promoted rapid nucleation of $FeVO_4$, $Zn_3V_2O_8$, and $Cd_2V_2O_7$ phases. This increase was attributed to the formation of interlocking crystalline networks and the development of fine Fe-based nanocrystals. The microstructure became more rigid and resistant to deformation due to the synergistic effects of multiple crystalline phases. Prolonged heat treatment led to further crystallite growth and the development of a predominantly polycrystalline structure. While the overall hardness remained high, minor phase segregation and coarsening in the high Fe concentration samples limited any further significant improvement.

- The elastic modulus (E), yield strength (Y), and shear modulus (G) were measured and observed to increase with increasing Fe content in the glassy samples reaching their maximum values for x=0.4 sample. Additionally, these properties (E, Y, and G) were found to be highest after 3h and 5h heat treatments, both low and high loading conditions.

- Investigated values of Vickers micro-hardness were analysed using different theoretical approaches including Meyer's law, EPD model, EPD model, HK approach, and IIC model. All samples exhibited RISE behaviour, which is also supported by these models. Among these, the IIC model was found to be the only successful model for describing the applied load with indentation data across all prepared samples. Additionally, the Vickers micro-hardness values of the sample with higher Fe concentration (x=0.4) after a 5h heat treatment were analysed using the same theoretical models. Once again, all samples showed RISE behaviour, which was supported by these models. The IIC model proved to be the only effective model to describe the applied load and indentation data for the x=0.4 sample at the 5h heat treatment condition.

5.2 Possible Applications

Glassy nanocomposite materials differ significantly from conventional composites or standard glass. Owing to their unique properties, these materials have garnered considerable attention across various fields. Adding modifiers such as ZnO, CdO, etc. to a glass matrix aims to improve properties like micro-hardness, crystallite size, electrical conductivity, and permeability. The primary goal of these glassy nanocomposites is to achieve a beneficial combination of properties. Some potential applications of glass nanocomposite materials are outlined. The prepared glassy composites are suitable for a broad range of electronic applications, including photovoltaic solar cells, gas sensors, light-emitting diodes, photodetectors, temperature sensors, transparent diodes, photoresistors, laser diodes, electrochromic windows, high strength fibers, and sensors. The exceptionally high micro-hardness of these materials enables the measurement of shear modulus and yield stress while also facilitating the study of their structural behavior. These properties make them valuable for applications requiring materials with high strength and hardness.

5.3 Future Scopes

The theoretical and experimental understanding of ionic and semiconducting glassy nanocomposites remains at a preliminary stage, indicating that the development of these materials and the discovery of new applications are still limited. The present study includes the development of Fe-doped $V_2O_5 \cdot MoO_3 \cdot CdO \cdot ZnO$ based glass nanocomposites through melt quenching method and their structural, electrical, and mechanical properties through experimental and numerical analysis. Several research aspects related to this topic emerge naturally from the conclusions of the present work. Suggestions for future research in this area are outlined below:

- The optical properties of the synthesized glass nanocomposites will be extensively studied to explore their potential applications in optoelectronic and photovoltaic devices.
- A systematic study of the dielectric behavior of glass nanocomposites needs to be conducted, as it may open up opportunities for their use in a wide range of applications.
- The magnetic properties of the synthesized glass nanocomposites will be investigated to explore their potential applications in the magnetic field.
- The potential applications of these semiconducting glass nanocomposites in both industrial and academic settings will be explored.

References

[1]. Mott, N. F. (1968). Conduction in glasses containing transition metal ions. *Journal of Non-Crystalline Solids*, 1(1), 1–17.

[2]. Austin, I. G., & Mott, N. F. (1969). Polarons in crystalline and non-crystalline materials. *Advances in Physics*, 18(71), 41–102.

[3]. Mogus-Milankovic, A., Pavic, L., Srilatha, K., Rao, C. S., Srikumar, T., Gandhi, Y., & Veeraiah, N. (2012). Electrical, dielectric and spectroscopic studies on MnO doped LiI–AgI–B_2O_3 glasses. *Journal of Applied Physics*, 111(1), 013714–013725.

[4]. Masai, H., Matsumoto, S., Ueda, Y., & Koreeda, A. (2016). Correlation between valence state of tin and elastic modulus of Sn-doped Li_2O–B_2O_3–SiO_2 glasses. *Journal of Applied Physics*, 119(18), 185104–185108.

[5]. Denton, E. P., Rawson, B., & Stanworth, J. E. (1954).

[6]. Mott, N. F. (1967). Electrons in disordered structures. *Advances in Physics*, 16(61), 49–144.

[7]. Ghosh, A. (1988). Memory switching in bismuth-vanadate glasses. *Journal of Applied Physics*, 64(5), 2652–2655.

[8]. Livage, J., Jollivet, J. P., & Tronc, E. (1990). Electronic properties of mixed valence oxide gels. *Journal of Non-Crystalline Solids*, 121(1-3), 35–39.

[9]. Sakuri, Y., & Yamaki, J. (1985). V_2O_5-P_2O_5 glasses as cathode for lithium secondary battery. *Journal of the Electrochemical Society*, 132(3), 512–513.

[10]. Peng, B., Fan, Z., Qui, X., Jaing, L., Ford, H. D., & Huang, W. (2005). A novel transparent vanadate glass for use in fiber optics. *Advanced Materials*, 17(7), 857–859.

[11]. Ashwajeet, J. S., Sankarappa, T., Ramanna, R., Sujatha, T., & Awasthi, A. M. (2015). Glass transition temperature and conductivity in Li_2O and Na2O doped borophosphate glasses. *AIP Conference Proceedings*, 1675, 020017-5.

[12]. Xu, G., Li, M., Dong, J., Wang, F., Liao, Q., Liu, L., & Zhang, J. (2024). Effect of substituting Na_2O with B_2O_3 on the crystallization and properties of MgO–Al_2O_3–SiO_2 transparent glass-ceramics. *Ceramics International*, 50(8), 2670–2679.

[13]. Liu, X., Zhou, J., Zhou, S., Yue, Y., & Qiu, J. (2018). Transparent glass-ceramics functionalized by dispersed crystals. *Progress in Materials Science*, 97, 38–96.

[14]. Hazra, S., & Ghosh, A. (1997). AC conductivity of unconventional bismuth cuprate glass. *Journal of Physics: Condensed Matter*, 9(17), 3981–3986.

[15]. Hazra, S., & Ghosh, A. (1998). Electrical relaxation mechanism in unconventional bismuth cuprate glasses. *Journal of Applied Physics*, 84(2), 987–992.

[16]. Ghosh, A. (1989). Temperature-dependent thermoelectric power of semiconducting bismuth-vanadate glass. *Journal of Applied Physics*, 65(1), 227.

[17]. Ghosh, A. (1989). Transport properties of iron-bismuthate glassy semiconductors. *Journal of Applied Physics*, 66(5), 2425.

[18]. Parmar, R., Kundu, R. S., Punia, R., Aghamkar, P., & Kishore, N. (2013). Effect of Fe_2O_3 on the physical and structural properties of bismuth silicate glasses. *AIP Conference Proceedings*, 1536, 653–654.

[19]. Aquino-Meneses, L., Lozada-Morales, R., Lopez-Calzada, G., Jiménez-Sandoval, S., Zayas, M. E., Zelaya-Angel, O., M. Becerril, M., Rodriguez, J. C., Mora, E. S., Serrano, L. E. (2015). Composition dependence of the crystalline-to-amorphous phase transformation of vanadate compounds in the CdO–V2O5 binary system. *Journal of Non-Crystalline Solids*, 408, 26–31.

[20]. El-Desoky, M. M. (2002). DC conductivity and hopping mechanism in V_2O_5–B_2O_3–BaO glasses. *Physica Status Solidi (a)*, 195(2), 422–428.

[21]. Ghosh, A., & Chaudhuri, B. K. (1986). DC conductivity of V_2O_5-Bi2O3 glasses. *Journal of Non-Crystalline Solids*, 83(1–2), 151–161.

[22]. Kundu, R., Roy, D., & Bhattacharya, S. (2015). Electrical transport of mixed-phased glassy nanocomposites. *Transactions of the Indian Ceramic Society*, 74(1), 35–40.

[23]. Sindhu, S., Sanghi, S., Agarwal, A., Seth, V. P., & Kishore, N. (2006). Structural, optical, physical, and electrical properties of $V_2O_5{\cdot}SrO{\cdot}B_2O_3$ glasses. *Spectrochimica Acta Part A: Molecular and Biomolecular Spectroscopy*, 64(1), 196–204.

[24]. Laila, S., Supardan, S. N., & Yahya, A. K. (2013). Effect of ZnO addition and concurrent reduction of V2O5 on network formation and elastic properties of lead vanadate (55 − x)V_2O_5–45PbO–(x)ZnO glass system. *Journal of Non-Crystalline Solids*, 367, 14–22.

[25]. Mary, N., Rebours, M., Castel, E., Vaishnav, S., Deng, W., Bell, A. M. T., ... & Bingham, P. A. (2018). Enhanced thermal stability of high-bismuth borate glasses by addition of iron. *Journal of Non-Crystalline Solids*, 500, 149–157.

[26]. El-Desoky, M. M., & Abo-Naf, S. M. (2004). Properties and structure of semiconducting sodium iron germanoborate glasses. *Journal of Materials Science: Materials in Electronics*, 15(8), 425–433.

[27]. El-Desoky, M. M., & Kashif, I. (2002). Electrical conductivity in mixed calcium and barium iron phosphate glasses. *Physica Status Solidi (a)*, 194(1), 89–105.

[28]. El-Desoky, M. M. (2003). Small polaron transport in V2O5–NiO–TeO_2 glasses. *Journal of Materials Science: Materials in Electronics*, 14(4), 215–221.

[29]. Al-Shahrani, A., Al-Hajry, A., & El-Desoky, M. M. (2003). Non-adiabatic small polaron hopping conduction in sodium borate tungstate glasses. *Physica Status Solidi (a)*, 200(2), 378–387.

[30]. Chung, C. H., & Mackenzie, J. D. (1980). Electrical properties of binary semiconducting oxide glasses containing 55 mole % V_2O_5. *Journal of Non-Crystalline Solids*, 42(2), 357–370.

[31]. Mansingh, A., Tandon, R. P., & Valid, J. K. (1980). AC conductivity of tungsten phosphate glasses. *Physical Review B*, 21(10), 4829–4839.

[32]. Murawski, L. (1984). AC conductivity in binary V_2O_5-P_2O_5 glasses. *Philosophical Magazine B*, 50(1), 69–74.

[33]. Sen, S., & Ghosh, A. (1999). Multiphonon-assisted hopping in strontium vanadate semiconducting glasses. *Journal of Physics: Condensed Matter*, 11(6), 1529–1536.

[34]. Filipic, C., Mogus-Milankovic, A., Pavic, L., Srilatha, K., Veeraiah, N., & Levstik, A. (2012). Polaronic behavior of MnO doped LiI-AgI-B_2O_3 glass. *Journal of Applied Physics*, 112(7), 073705.

[35]. Jung, W. H. (1998). Magnetic and transport properties of $Ce_2/3TiO_2$. *Journal of Physics: Condensed Matter*, 10(38), 8553–8558.

[36]. Bar, A. K., Bhattacharya, K., Kundu, R., Roy, D., & Bhattacharya, S. (2016). Electrical relaxation and grain boundary effect in CdI_2 doped glass-nanocomposites. *Journal of Non-Crystalline Solids*, 452, 169–175.

[37]. Mogus-Milankovic, A., Santic, B., Day, D. E., & Ray, C. S. (2001). Electrical conductivity in mixed-alkali iron phosphate glasses. *Journal of Non-Crystalline Solids*, 283(1–3), 119–128.

[38]. Mogus-Milankovic, A., Licina, V., Reis, S. T., & Day, D. E. (2007). Electronic relaxation in zinc iron phosphate glasses. *Journal of Non-Crystalline Solids*, 353(26–27), 2659–2666.

[39]. Reis, S. T., Mogus-Milankovic, A., Licina, V., Yang, J. B., Karabulut, M., Day, D. E., & Brow, R. K. (2007). Iron redox equilibrium, structure, and properties of zinc iron phosphate glasses. *Journal of Non-Crystalline Solids*, 353(2), 151–158.

[40]. Santic, B., Mogus-Milankovic, A., & Day, D. E. (2001). The DC electrical conductivity of iron phosphate glasses. *Journal of Non-Crystalline Solids*, 296(1–2), 65–73.

[41]. Bhattacharya, S., & Ghosh, A. (2005). Transport properties of AgI doped silver molybdate superionic glass-nanocomposites. *Journal of Physics: Condensed Matter*, 17(36), 5655–5662.

[42]. Ghosh, A. (1990). Transport properties of vanadium germanate glassy semiconductors. *Physical Review B,* 42(9), 5665–5676.

[43]. Murugavel, S., & Upadhyay, M. (2011). AC conduction in amorphous semiconductors. *Journal of the Indian Institute of Science*, 91(2), 303–318.

[44]. Pollak, M., & Pike, G. E. (1972). AC conductivity of glasses. *Physical Review Letters*, 28(25), 1449–1451.

[45]. Elliott, S. R. (1978). Temperature dependence of AC conductivity of chalcogenide glasses. *Philosophical Magazine B*, 37(5), 533–560.

[46]. Gong, J., Wu, J., & Guan, Z. (1999). Examination of the indentation size effect in low-load Vickers Hardness Testing of Ceramics. *Journal of the European Ceramic Society*, 19(15), 2625–2631.

[47]. Giannakopoulos, A. E., Larsson, P. L., & Vestergaard, R. (1994). Analysis of Vickers indentation. *International Journal of Solids and Structures*, 31(19), 2679–2708.

[48]. Sangwal, K. (2000). On the reverse indentation size effect and microhardness measurement of solids. *Materials Chemistry and Physics*, 63(2), 145–152.

[49]. Wredenberg, F., & Larson, P. L. (2009). Scratch testing of metals and polymers: Experiments and numerics. *Wear*, 266(1–2), 76–83.

[50]. Dogruer, M., Gorur, O., Karaboga, F., Yildirim, G., Terzioglu, C., (2013) Zr diffusion coefficient and activation energy calculations based on EDXRF measurement and evaluation of mechanical characteristics of $YBa_2Cu_3O_7$-x bulk superconducting ceramics diffused with Zr nanoparticles. *Powder Technology*, 246, 553–560.

[51]. Ozturk, O., Asikuzun, E., Tasci, A. T., Gokcen, T., Ada, H., Koralay, H., & Cavdar, S. (2018). Comparison of Vickers microhardness of undoped and Ru-doped BSCCO glass ceramic materials. *Journal of Materials Science: Materials in Electronics, 29*, 3957–3966.

[52]. Askari-Paykani, M., Nili-Ahmadabadi, M., & Seiffodini, A. (2014). On the subsurface deformation of two different Fe-based bulk metallic glasses indented by Vickers micro hardness. *Intermetallics, 46*, 118–125.

[53]. Tian, C., Ruan, J., Zhao, X., Han, J., & Liu, C. (2024). Infrared transparent CaO–Ta2O5–Al2O3 glass-ceramics with high microhardness: Crystallization behavior and microstructure development. *Ceramics International, 50*(7), 10465–10475.

[54]. Kasimuthumaniyan, S., Reddy, A. A., Krishnana, N. M. A., & Gosvami, N. N. (2020). Understanding the role of post-indentation recovery on the hardness of glasses: Case of silica, borate, and borosilicate glasses. *Journal of Non-Crystalline Solids, 534*, 119955.

[55]. Rouxel, T. (2015). Driving force for indentation cracking in glass: Composition, pressure, and temperature dependence. *Philosophical Transactions of the Royal Society A: Mathematical, Physical and Engineering Sciences, 373*, 1–26.

[56]. Khoeini, M., Kolahi, A., & Hesaraki, S. (2022). Mechanical properties, bioactivity, and cell behavior of barium-containing calcium-phospho-alumino-borosilicate glass. *Ceramics International, 48*, 7643–7651.

[57]. Ediger, M. D., & Harrowell, P. (2012). J. *Chemical Physics, 137*, 080901.

[58]. Gibbs, P. (2007). Is glass liquid or solid, *Glass Worldwide, 11*, 14-18.

[59]. Bragg, W. (2002). The Glassy State. In *Structural Chemistry of Glasses* (pp. 13-76). Elsevier Science Ltd.

[60]. Zallen, R. (2008). *The physics of amorphous solids*. John Wiley & Sons.

[61]. Cusack, N. E., & Stein, D. L. (1988). The physics of structurally disordered matter: an introduction.

[62]. Elliott, S. R. (1984). *Physics of amorphous materials*. Longman Group Ltd.

[63]. Scholze, H. (2012). *Glass: nature, structure, and properties*. Springer Science & Business Media.

[64]. Shelby, J. E. (2020). *Introduction to glass science and technology*. Royal society of chemistry.

[65]. Varshneya, A. K. (1994). *Fundamentals of inorganic glasses*. Academic Press.

[66]. Min'ko, N. I., & Nartsev, V. M. (2008). Nanotechnology in glass materials, *Glass and Ceramics*, 65(5), 148-153.

[67]. Dan, A., Satpati, B., Satyam, P. V., & Chakravorty, D. (2003). Diodelike behavior in glass–metal nanocomposite, *Journal of applied physics*, 93(8), 4794-4800.

[68]. Fleming, L. A., Wackerow, S., Hourd, A. C., Gillespie, W. A., Seifert, G., & Abdolvand, A. (2012), Diffractive optical element embedded in silver-doped nanocomposite glass, *Optics Express*, 20(20), 22579-22584.

[69]. W. G. Drost, H. Hofmeister and A. Berger, (2005) Proceedings 33rd Topical Meeting on Liquid Crystals, Deutsche Flüssigkristall-Gesellschaft, Frankfurt, Germany P2-1-P2-4.

[70]. Stepanov, A. L. (2016). Nonlinear optical properties of metal nanoparticles in silicate glass. In Glass Nanocomposites (pp. 165-179). William Andrew Publishing.

[71]. Stalmashonak, A., Abdolvand, A., & Seifert, G. (2011). Metal-glass nanocomposite for optical storage of information. *Applied Physics Letters*, 99(20).

[72]. Thomas, S., Nair, S. K., Jamal, E. M. A., Al-Harthi, S. H., Varma, M. R., & Anantharaman, M. R. (2008). Size-dependent surface plasmon resonance in silver silica nanocomposites. *Nanotechnology*, 19(7), 075710.

[73]. Khan, I., Saeed, K., & Khan, I. (2019). Nanoparticles: Properties, applications and toxicities, *Arabian journal of chemistry*, 12(7), 908-931.

[74]. Karmakar, B. (2016). Fundamentals of glass and glass nanocomposites. In Glass nanocomposites (pp. 3-53). William Andrew Publishing.

[75]. Wong, J., & Angell, C. A. (1976). *Glass structure by spectroscopy*.

[76]. Marcel Dekker. Mizuno, F., Hayashi, A., Tadanaga, K., & Tatsumisago, M. (2005). Adv. Mat., *17*, 918.

[77]. Brinker, C. J., & Scherer, G. W. (1990). *Sol-gel science: The physics and chemistry of sol-gel processing*. Academic Press.

[78]. Dimitriev, Y., Yordanov, S., & Lakov, L. (2001). *J. Non-Cryst. Solids, 293-295*, 410.

[79]. Venkateswarlu, M., Narasimha Reddy, K., Rambabu, B., & Satyanarayana, N. (2000). *Solid State Ionics, 127*, 177.

[80]. Bach, H. (1970). Application of ion sputtering in preparing glasses and their surface layers for electron microscope investigations. *Journal of Non-Crystalline Solids*, *3*(1), 1–32.

[81]. Williams, P. (1979). The sputtering process and sputtered ion emission. *Surface Science*, *90*(2), 588–634.

[82]. Huber, C. A., Huber, T. E., Sadoqi, M., Lubin, J. A., Manalis, S., & Prater, C. B. (1994). *Science, 263*, 800.

[83]. Ojha, S., Roy, M., Chamuah, A., Bhattacharya, K., & Bhattacharya, S. (2020). Transport phenomena of Cu–S–Te chalcogenide nanocomposites: Frequency response and AC conductivity. *Phys. Chem. Chem. Phys., 22*, 24600.

[84]. Hassanien, A. S., & Akl, A. A. (2015). Estimation of some physical characteristics of chalcogenide bulk Cd50S50 − xSex glassy systems. *J. Non-Cryst. Solids*, *428*, 112–120.

[85]. Li, B., Qing, Z., Li, Y., Li, H., & Zhang, S. (2016). Effect of CaO content on structure and properties of low temperature co-fired glass–ceramic in the Li_2O–Al_2O_3–SiO_2 system. *J. Mater. Sci. Mater Electron*, *27*, 2455.

[86]. Arvind, A., Kumar, R., Deo, M. N., Shrikhande, V. K., & Kothiyal, G. P. (2009). Preparation, structural and thermo-mechanical properties of lithium aluminum silicate glass–ceramics. *Ceram. Int.*, *35*, 1661–1666.

[87]. Subhashini, H. D., Shashikala, N. K., & Udayashankar, N. K. (2020). Influence of Fe3+ ions on optical, structural, thermal, and mechanical properties of Li_2O–Na_2O–K_2O–ZnO–B_2O_3 based glass system. *Ceram. Int.*, *46*(4), 5213–5222.

[88]. Mhareb, M. H. A., Hashim, S., Ghoshal, S. K., Alajerami, Y. S. M., Saleh, M. A., Dawaud, R. S., Razak, N. A. B., & Azizan, S. A. B. (2014). Impact of Nd3+ ions on physical and optical properties of Lithium Magnesium Borate glass. *Opt. Mater.*, *37*, 391–397.

[89]. Mosset, A., Lecante, P., Galy, J., & Livage, J. (1982). Structural analysis of amorphous V2O5 by large-angle X-ray scattering. *Philosophical Magazine B*, *46*(2), 137-149.

[90]. Nabavi, M., Sanchez, C., & Livage, J. (1991). Structure and properties of amorphous V_2O_5. *Philosophical Magazine B*, *63*(4), 941-953.

[91]. Takeda, S., Kawakita, Y., Inui, M., Maruyama, K., Tamaki, S., Sugiyama, K., & Aseda, Y. (1996). J. Non-Cryst. Solids, *205*, 151.

[92]. Jain, D., Sudarsan, V., Vatsa, R. K., & Pillai, C. G. S. (2009). J. Lumin., *129*, 439–443.

[93]. Eskizeybek, V., Avci, A., & Chhowalla, M. (2011). Cryst. Res. Technol., *46*, 1093–1100.

[94]. Sayer, M., & Mansingh, A. (1972). Phys. Rev. B, *6*, 4629–4643.

[95]. Khattak, G. D., Tabet, N., & Wenger, L. E. (2005). Structural properties of glasses in the series $(SrO)x(V_2O_5)1-x$, $(SrO)0.5-y(B_2O_3)y(V_2O_5)0.5$, and $(SrO)0.2(B_2O_3)z(V_2O_5)0.8-z$. *Phys. Rev. B, 72*, 104203-1–104203-6.

[96]. Saddeek, Y. B. (2009). Synthesis and properties of MoO_3-V_2O_5-PbO glasses. *Philos. Mag., 89*, 2305–2320.

[97]. Limaye, M. V., Singh, S. B., Das, R., Poddar, P., & Kulkarni, S. K. (2011). Room temperature ferromagnetism in undoped and Fe doped ZnO nanorods: Microwave-assisted synthesis. *J. Solid State Chem.*, *184*(2), 391–400.

[98]. Kaviyarasu, K., Manikandan, E., Paulraj, P., Mohamed, S. B., & Kennedy, J. (2014). One dimensional well-aligned CdO nanocrystal by solvothermal method. *J. Alloys Compd.*, *593*, 67–70.

[99]. Das, A. S., Roy, M., Kar, T., Rath, S., & Bhattacharya, S. (2017). Investigations of microstructure and DC conductivity of V_2O_5-Nd_2O_3 glass nanocomposites. *Chem. Select*, *2*, 11273–11280.

[100]. Bhattacharya, S., Das, A. S., Roy, M., & Roy, D. (2017). Frequency and temperature dependent conductivity spectra of mixed transition metal oxide doped semiconducting glassy system. *J. Non-Cryst. Solids*, *478*, 58–64.

[101]. Biswas, D., Ningthemcha, R. K. N., Das, A. S., & Singh, L. S. (2019). Structural characterization and electrical conductivity analysis of MoO_3–SeO_2–ZnO semiconducting glass nanocomposites. *J. Non-Cryst. Solids*, *515*, 21–33.

[102]. Murawski, L., Chung, C. H., & Mackenzie, J. D. (1979). Electrical properties of semiconducting oxide glasses. *Journal of non-crystalline solids*, *32*(1-3), 91-104.

[103]. El-Desoky, M. M., Tahoon, K., & Hassaan, M. Y. (2001). Conductivity and dielectric behaviour of iron sodium phosphate glasses. *Materials chemistry and physics*, *69*(1-3), 180-185.

[104]. Day, D. E. (1999). DC conductivity and polarisation in iron phosphate glasses. *Physics and chemistry of glasses*, *40*(2), 69-74.

[105]. Moguš-Milanković, A., & Day, D. E. (1993). Thermally stimulated polarization and dc conduction in iron phosphate glasses. *Journal of non-crystalline solids*, *162*(3), 275-286.

[106]. Mott, N. F. (1969). Conduction in non-crystalline materials: III. Localized states in a pseudogap and near extremities of conduction and valence bands. *Philosophical Magazine*, *19*(160), 835-852.

[107]. Nasu, H., & Soga, N. (1982). Temperature dependence of electrical conduction of sodium-iron phosphate glasses. *Journal of non-crystalline solids*, *53*(1-2), 123-134.

[108]. Mohammadigharehbagh, R., Pat, S., Akkurt, N., & Korkmaz, S. (2021). Physica B: Physics of Condensed Matter, *609*, 412921.

[109]. Neupane, G. R., Kaphle, A., Hari, P. (2019). Microwave-assisted Fe-doped ZnO nanoparticles for enhancement of silicon solar cell efficiency. *Sol. Energy Mater. Sol. Cell*, *201*, 110073.

[110]. Sahai, A., Kumar, Y., Agarwal, V., Olive-Méndez, S. F., Goswami, N. (2014). Doping concentration driven morphological evolution of Fe doped ZnO nanostructures. *J. Appl. Phys.*, *116*(16), 164315.

[111]. Somacescu, S., Dinescu, A., & Osiceanu, P. (2012). Nanostructured Fe doped ZnO: TiO 2 for gas sensors applications. In *CAS 2012 (International Semiconductor Conference)* (Vol. 2, pp. 337–340). IEEE.

[112]. Xu, H., Wu, C., Xiahou, Z., Jung, R., Li, Y., Liu, C. (2017). Improved resistance switching stability in Fe-doped ZnO thin films through pulsed magnetic field annealing. *Nanoscale research letters*, *12*(1), 176.

[113]. Muneer, M. B. A., Kadhum, A. A. H., Mohamad, A. B., Takriff, M. S., & Sopian, K. (2013). Visible light photocatalytic activity of Fe3+-doped ZnO nanoparticles prepared via sol–gel technique. *Chemosphere*, *91*, 1604–1611.

[114]. Karmakar, D., Mandal, S. K., Kadam, R. M., Paulose, P. L., Rajarajan, A. K., Nath, T. K., Das, A. K., Dasgupta, I., & Das, G. P. (2007). *J. Phys. Rev. B*, *75*.

[115]. Inamdar, D. Y., Pathak, A. K., Dubenko, I., Ali, N., & Mahamuni, S. (2011). Room temperature ferromagnetism and photoluminescence of Fe doped ZnO nanocrystals. *J. Phys. Chem. C*, *115*(48), 23671–23676.

[116]. Moguš-Milankovic, A., Šantic, A., Ličina, V., & Day, D. E. (2005). *Journal of Non-Crystalline Solids*, *351*, 3235–3245.

[117]. Machida, N., & Eckert, H. (1998). *Solid State Ionics*, *107*, 255.

[118]. Kuwata, N., Saito, T., Tatsumisago, M., Minami, T., & Kawamura, J. (2004). Solid State Ionics, *175*, 679.

[119]. Broitman, E. (2017). Indentation hardness measurements at macro-, micro-, and nanoscale: A critical overview. *Tribol. Lett.*, *65*, 23 (1-18).

[120]. Qian, D. D., Zhang, L., & Zhang, Y. (2018). Impact of thermal shock cycles on mechanical properties and microstructure of lithium disilicate dental glass-ceramic. *Ceram. Int.*, *44*, 1589–1593.

[121]. Gui, H., Li, C., & Lin, C. (2019). Glass forming, crystallization, and physical properties of MgO-Al_2O_3-SiO_2-B_2O_3 glass ceramics modified by ZnO replacing MgO. *J. Eur. Ceram. Soc.*, *39*, 1397–1410.

[122]. Sengupta, A., Halder, P., Ali, M. S., Ghosh, C. K., & Bhattacharya, S. (2022). Li_2O-ZnO-MoO_3-SeO_2 glass-nanocomposites and their crystalline counterparts: microstructure, electrical transport mechanism and first principle DFT analysis. *Physica Scripta*, *97*(8), 085804.

[123]. Hallmann, L., Ulmer, P., & Kern, M. (2018). Effect of microstructure on the mechanical properties of lithium disilicate glass-ceramics. *Journal of the mechanical behavior of biomedical materials*, *82*, 355-370.

[124]. Li, D., Guo, J. W., Wang, X. S., Zhang, S. F., & He, L. (2016). Effects of crystal size on the mechanical properties of a lithium disilicate glass-ceramic. *Materials Science and Engineering: A*, *669*, 332-339.

[125]. Huang, X., Zheng, X., Zhao, G., Zhong, B., Zhang, X., & Wen, G. (2014). Microstructure and mechanical properties of zirconia-toughened lithium disilicate glass–ceramic composites. *Materials Chemistry and Physics*, *143*(2), 845-852.

[126]. Wen, G., Zheng, X., & Song, L. (2007). Effects of P_2O_5 and sintering temperature on microstructure and mechanical properties of lithium disilicate glass-ceramics. *Acta materialia*, *55*(10), 3583-3591.

[127]. Peitl, O., Zanotto, E. D., Serbena, F. C., & Hench, L. L. (2012). Compositional and microstructural design of highly bioactive P_2O_5–Na_2O–CaO–SiO_2 glass-ceramics. *Acta biomaterialia*, *8*(1), 321-332.

[128]. Serbena, F. C., Soares, V. O., Peitl, O., Pinto, H., Muccillo, R., & Zanotto, E. D. (2011). Internal residual stresses in sintered and commercial low expansion Li_2O–

Al_2O_3–SiO_2 glass–ceramics. *Journal of the American Ceramic Society*, *94*(4), 1206-1214.

[129]. Monmaturapoj, N., Lawita, P., & Thepsuwan, W. (2013). Characterisation and properties of lithium disilicate glass ceramics in the SiO_2-Li_2O-K_2O-Al_2O_3 system for dental applications. *Advances in Materials Science and Engineering*, *2013*(1), 763838.

[130]. Stookey, S. D. (1959). Catalyzed crystallization of glass in theory and practice. *Industrial & Engineering Chemistry*, *51*(7), 805-808.

[131]. McNally, R. N., & Beall, G. H. (1979). Crystallization of fusion cast ceramics and glass-ceramics. *Journal of materials science*, *14*, 2596-2604.

[132]. Freiman, S. W., & Hench, L. L. (1972). Effect of crystallization on the mechanical properties of Li_2O-SiO_2 glass-ceramics. *Journal of the American Ceramic Society*, *55*(2), 86-90.

[133]. Grau, P., Berg, G., Meinhard, H., & Mosch, S. (1998). Strain rate dependence of the hardness of glass and Meyer's law. *Journal of the American Ceramic Society*, *81*(6), 1557–1564.

[134]. Ozturk, O., Asikuzun, E., Kaya, S., Yildirim, G., Turkoz, M., & Kilic, A. (2014). Improvement of the nature of indentation size effect of Bi-2212 superconducting matrix by doped Nd inclusion and theoretical modeling of new matrix. *Journal of Superconductivity and Novel Magnetism, 27,* 1403–1412.

[135]. Asikuzun, E., Ozturk, O., Cetinkara, H. A., Yildirim, G., Varilci, A., Yılmazlar, M., & Terzioglu, C. (2012). Vickers hardness measurements and some physical properties of Pr2O3 doped Bi-2212 superconductors. *Journal of Materials Science: Materials in Electronics, 23,* 1001–1010.

[136]. Oliver, W. C., & Pharr, G. M. (1992). An improved technique for determining hardness and elastic modulus using load and displacement sensing indentation experiments. *Journal of Materials Research, 7,* 1564–1583.

[137]. Tabor, D. (1951). The hardness and strength of metals. *Journal of the Institute of Metals, 79,* 1–18.

[138]. Koralay, H. A. L. U. K., Arslan, A. Y. T. E. N., Cavdar, S., Ozturk, O., Asikuzun, E., Gunen, A., & Tasci, A. T. (2013). Structural and mechanical characterization of

Bi 1.75 Pb 0.25 $Sr_2Ca_2Cu_3-$ xSnxO 10+ y superconductor ceramics using Vickers microhardness test. *Journal of Materials Science: Materials in Electronics*, *24*, 4270-4278.

[139]. Kölemen, U., Uzun, O., Yılmazlar, M., Güçlü, N., & Yanmaz, E. K. R. E. M. (2006). Hardness and microstructural analysis of Bi1. 6Pb0. $4Sr_2Ca_2-$ xSmxCu_3Oy polycrystalline superconductors. *Journal of alloys and compounds*, *415*(1-2), 300-306.

[140]. Cavdar, S., Deniz, E., Koralay, H., Ozturk, O., Erdem, M., & Gunen, A. (2012). The effect of PbSe addition on the mechanical properties of Bi-2212 superconductors. *Journal of Superconductivity and Novel Magnetism*, *25*, 2297–2307.

[141]. Sun, J., Francis, L. F., & Gerberich, W. W. (2005). Mechanical properties of polymer-ceramic nanocomposite coatings by depth-sensing indentation. *Polymer Engineering and Science*, *45*, 207–216.

[142]. Bull, S. J., Page, T. F., & Yoffe, E. H. (1989). An explanation of the indentation size effect in ceramics. *Philosophical Magazine Letters*, *59*, 281–288.

[143]. Upit, G. P., & Varchenya, S. A. (1966). Microhardness of alkali halide crystals. *Physica Status Solidi*, *17*, 831–835.

[144]. Ma, Q., & Clarke, D. R. (1995). Size dependent hardness of silver single crystals. *Journal of Materials Research*, *10*, 853–863.

[145]. Hays, C., & Kendall, E. G. (1973). An analysis of Knoop microhardness. *Metallography*, *6*, 275–282.

[146]. Mott, B. W. (1956). *Micro-indentation hardness testing*. Butterworths.

[147]. Zhang, D., & Li, D. Y. (2023). A further look at the nano/micro-indentation method for measuring and ranking Young's modulus and hardness of materials. *Physica Scripta*, *98*, 095936 (1–9).

[148]. Alao, A. R., & Bujang, M. H. D. (2021). Load effect on the mechanical behaviour of zirconia-reinforced lithium silicate glass ceramics. *Ceramics International*, *47*, 1353–1363.

[149]. Turkoza, M. B., Zalaoglu, Y., Turgay, T., Ozturk, O., Akkurte, B., & Yildirim, G. (2019). Evaluation of key mechanical design properties and mechanical characteristic features of advanced Bi-2212 ceramic materials with homovalent Bi/Ga partial replacement: Combination of experimental and theoretical approaches. *Ceramics International*, *45*, 21183–21192.

[150]. Ling, H. C., & Yan, M. F. (1988). Microhardness measurements on dopant-modified superconducting YBa2Cu3O7 ceramics. *Journal of Applied Physics, 64*, 1307–1311.

[151]. Celik, S., Ozturk, O., Coşkun, E., Sarıhan, M., Asikuzun, E., Ozturk, K., & Terzioglu, C. (2013). Analysis of indentation size effect (ISE) behavior in low-load Vickers microhardness testing of (Sm123)1–x(Nd123)x superconductor system. *Journal of Materials Science: Materials in Electronics, 24*, 2218–2227.

[152]. Bernhardt, E. O. (1941). About the microhardness of the solid substances in the border area of the kick similarity set. *International Journal of Materials Research, 33*, 135.

[153]. Ghosh, S., & Ghosh, A. (2007). Relaxation in mixed alkali fluoride glasses. *Journal of Non-Crystalline Solids, 353*, 1287–1290.

[154]. Ghosh, S., & Ghosh, A. (2005). Ion dynamics and mixed mobile ion effect in fluoride glasses. *Journal of Applied Physics, 97*, 123525.

[155]. Li, H., & Bradt, R. C. (1993). The microhardness indentation load/size effect in rutile and cassiterite single crystals. *Journal of Materials Science, 28*, 917–926.

[156]. Nix, W. D., & Gao, H. (1998). Indentation size effects in crystalline materials: A law for strain gradient plasticity. *Journal of the Mechanics and Physics of Solids, 46*, 411–425.

[157]. Awad, R., Abou-Aly, A. I., Kamal, M., & Anas, M. (2011). Mechanical properties of (Cu0.5Tl0.5)-1223 substituted by Pr. *Journal of Superconductivity and Novel Magnetism, 24*, 1947–1956.

[158]. Tosun, M., Ataoglu, S., Arda, L., Ozturk, O., Asikuzun, E., Akcan, D., & Cakiroglu, O. (2014). Structural and mechanical properties of ZnMgO nanoparticles. *Materials Science and Engineering A, 590*, 416–422.

[159]. Li, H., & Bradt, R. C. (1996). The effect of indentation-induced cracking on the apparent microhardness. *Journal of Materials Science, 31*, 1065–1070.

[160]. Sher, A., Chen, A. B., & Spicer, W. E. (1985). Dislocation energies and hardness of semiconductors. *Applied Physics Letters, 46*, 54–56.

[161]. Bhattacharya, S., Kundu, R., Bhattacharya, K., Poddar, A., & Roy, D. (2019). Micromechanical hardness study and the effect of reverse indentation size on heat-treated silver doped zinc-molybdate glass nanocomposites. *Journal of Alloys and Compounds, 770*, 136–142.

[162]. Chanshetti, U. B., Shelke, V. A., Jadav, S. M., Shankarwar, S. G., Chondhekar, T. K., Shankarwar, A. G., Sudarsan, V., & Jogad, M. S. (2011). Density and molar volume studies of phosphate glasses. *Physics, Chemistry and Technology, 9*, 29.

[163]. Elliott, S. R. (1987). A.C. conduction in amorphous chalcogenide and pnictide semiconductors. *Advances in Physics, 36*, 135–217.

[164]. Almond, D. P., Duncan, G. K., & West, A. R. (1983). The determination of hopping rates and carrier concentrations in ionic conductors by a new analysis of ac conductivity. *Solid State Ionics, 8*, 159–164.

[165]. AbdelAziz, T. D., EzzElDin, F. M., ElBatal, H. A., & Abdelghany, A. M. (2014). Optical and FT infrared spectral studies of vanadium ions in cadmium borate glass and effects of gamma irradiation. *Spectrochimica Acta Part A: Molecular and Biomolecular Spectroscopy, 131*, 497–501.

[166]. Al-Shamiri, H. A., & Eid, A. S. (2012). Optical and ultrasonic properties of chromium oxide in sodium zinc phosphate glass. *Photonics and Optoelectronics*, 1(1), 1-8.

[167]. Gersappe, D. (2002). Molecular mechanisms of failure in polymer nanocomposites. *Physical review letters*, 89(5), 058301.

[168]. Jordan, J., Jacob, K. I., Tannenbaum, R., Sharaf, M. A., & Jasiuk, I. (2005). Experimental trends in polymer nanocomposites—a review. *Materials science and engineering: A*, 393(1-2), 1-11.

[169]. Vollenberg, P. H. T., & Heikens, D. (1989). Particle size dependence of the Young's modulus of filled polymers: 1. Preliminary experiments. *Polymer*, 30(9), 1656-1662.

[170]. Chan, C. M., Wu, J., Li, J. X., & Cheung, Y. K. (2002). Polypropylene/calcium carbonate nanocomposites. *polymer*, 43(10), 2981-2992.

[171]. Ivascu, C., Gabor, A. T., Cozar, O., Daraban, L., & Ardelean, I. (2010). FT-IR, Raman and thermoluminescence investigation of P2O5–BaO–Li2O glass system. *Journal of Molecular Structure, 993*, 249–253.

[172]. Ahmed, E. M., El-Ghamaz, N. A., & Edres, A. M. (2018). Thermal kinetics and theoretical third order nonlinear optical susceptibility of some $As_2O_3.V_2O_5.FeO$ glasses. *Physica Status Solidi A, 215*, 1800299.

[173]. Atta, A. A., Ahmed, E. M., Al Hasni, B., Wahb, H. H., Alkathiri, A. A. (2023). Mössbauer spectroscopy and other structural properties of some $V_2O_5{\cdot}SrO{\cdot}FeO$ glasses. *Materials Research Innovations*, *27*, 20–28.

[174]. Abdel-Wahab, F., Mostafa, A. G., Belal, A. E., & El-Agwany, E. M. (2005). Mössbauer spectroscopy and electrical transport properties of iron-doped sodium lead borate glasses. *Materials Chemistry and Physics, 93*, 243–250.

[175]. Ahmed, E. M. (2013). Threshold switching in V_2O_5-ZnO-SrO-FeO glasses. *Current Applied Physics, 13*, 408–414.

[176]. Al-syadi, A. M., El-Desoky, M. M., & Al-Assiri, M. S. (2013). Impedance spectroscopy of V_2O_5–Bi_2O_3–BaTiO3 glass–ceramics. *Solid state sciences*, 26, 72-82.

[177]. Nowiński, J. L., Łasińska, A., Czajkowska, A., Garbarczyk, J. E., Wasiucionek, M., & Żukowska, G. Z. (2008). Electrical properties of silver vanadate amorphous superionic conductors prepared via a mechanosynthesis route. *Solid State Ionics*, 179(1-6), 206-212.

[178]. Hayakawa, S., Yoko, T., & Sakka, S. (1994). Structural studies on alkaline earth vanadate glasses (Part 1) IR Spectroscopic Study. *Journal of the Ceramic Society of Japan*, 102(1186), 522-529.

[179]. Yuvaraj, S., Selvan, R. K., Kumar, V. B., Perelshtein, I., Gedanken, A., Isakkimuthu, S., et al. (2014). *Ultrasonics Sonochemistry, 21*, 599–605.

[180]. Andreetti, G. D., Calestani, G., & Montenero, A. (1984). Refinement of the crystal structure of ZnV_2O_6. *Crystal Research and Technology, 168*(1-4), 53–58.

[181]. Hayakawa, S., Yoko, T., & Sakka, S. (1995). IR and NMR structural studies on lead vanadate glasses. *Journal of Non-Crystalline Solids, 183*, 73–84.

[182]. Gopal, R., & Calvo, C. (1973). Crystal structure of α-$Zn_2V_2O_7$. *Canadian Journal of Chemistry*, 51(7), 1004-1009.

[183]. Pedregosa, J. C., Baran, E. J., & Aymonino, P. J. (1974). Kristallchemisches Verhalten und IR-Spektren einiger Divanadate des Thortveitit-Typs und verwandter Strukturen. *Zeitschrift für anorganische und allgemeine Chemie*, 404(3), 308-320.

[184]. Baran, E. J., Botto, I. L., Pedregosa, J. C., & Aymonino, P. J. (1978). The vibrational spectrum of Sr2V2O7 and the vibrational properties of the divanadate ion. *Monatshefte für Chemie/Chemical Monthly*, 109, 41-51.

[185]. Poddar, A., Das, S., Roy, M., Bhattacharya, K., & Bhattacharya, S. (2022). Transport properties of CdI2-doped silver ion conducting system: validation with first-principle DFT estimations. *Ionics*, 28(5), 2285-2292.

[186]. Seguin, L., Figlarz, M., Cavagnat, R., & Lassègues, J. C. (1995). Infrared and Raman spectra of MoO3 molybdenum trioxides and MoO3· xH2O molybdenum trioxide hydrates. *Spectrochimica Acta Part A: Molecular and Biomolecular Spectroscopy*, 51(8), 1323-1344.

[187]. Beattie, I. R., & Gilson, T. R. (1969). Oxide phonon spectra. *Journal of the Chemical Society A: Inorganic*, Physical, Theoretical, 2322-2327.

[188]. Lehnen, T., Valldor, M., Niznansky, D., & Mathur, S. (2014). Hydrothermally grown porous FeVO4 nanorods and their integration as active material in gas-sensing devices. *Journal of Materials Chemistry A*, *2*(6), 1862–1868.

[189]. Prakash, V. A., & Rajadurai, A. (2016). Mechanical, thermal and dielectric characterization of iron oxide particles dispersed glass fiber epoxy resin hybrid composite. *Digest J Nanomater Biostruct*, 11(2), 373-80.

[190]. Chernova, N. A., Roppolo, M., Dillon, A. C., & Whittingham, M. S. (2009). Layered vanadium and molybdenum oxides: batteries and electrochromics. *Journal of Materials Chemistry*, 19(17), 2526-2552.

[191]. Biswas, D., Singh, Y. B., Das, A. S., Mondal, R., Roy, D., Adhikari, S., & Singh, L. S. (2019). Investigation of microstructure and temperature and frequency

dependent dielectric relaxation of Molybdenum-zinc-selenite glass nanocomposite systems. *Materials Research Express*, 6(11), 115205.

[192]. Ghosh, J., Sengupta, A., Halder, P., Ojha, S., Panda, G. K., & Bhattacharya, S. (2022). Single polaron hopping in Fe doped glassy semiconductors: Structure–electrical transport relationship. *Journal of Applied Physics, 132*(20), 205108.

[193]. Poddar, A., Das, S., Roy, M., Bhattacharya, K., & Bhattacharya, S. (2022). Transport properties of CdI2-doped silver ion conducting system: Validation with first-principle DFT estimations. *Ionics, 28*, 2285–2292.

[194]. Reddy, S., Swamy, B. K., Chandra, U., Sherigara, B. S., & Jayadevappa, H. (2010). Synthesis of CdO nanoparticles and their modified carbon paste electrode for determination of dopamine and ascorbic acid by using cyclic voltammetry technique. *International Journal of Electrochemical Science*, 5(1), 10-17.

[195]. Al-Tememee, N. A., Saeed, N. M., Al-Dujayli, S. M., & Chiad, B. T. (2012). The effect of zn concentration on the optical properties of Cd10–xZnxS films for solar cells applications. *Advances in Materials Physics and Chemistry*, 2(2), 69.

[196]. Kumar, P., Joshi, R., Gaur, A., Kumar, L., & Asokan, K. (2015). Impact of sintering temperature on structural, optical and ferroelectric properties of V-doped ZnO. *Materials Research Express*, 2(4), 045901.

[197]. Mondal, C., Ganguly, M., Sinha, A. K., Pal, J., Sahoo, R., & Pal, T. (2013). Robust cubooctahedron $Zn_3V_2O_8$ in gram quantity: a material for photocatalytic dye degradation in water. *Cryst. Eng. Comm*, 15(34), 6745-6751.

[198]. LakshmanaNaik, R., Narsaiah, T. B., Justin, P., Dhanalakshmi, M., Kumar, A. N., Somashekar, M. N., Sharanakumar, T. M., Ravikumar, C. R., & Murthy, H. A. (2024). Enhanced performance of hydrothermally synthesized zinc vanadium oxide nanoparticles for supercapacitor and photocatalytic applications. *Journal of the Indian Chemical Society*, 101(10), 101247.

[199]. Guskos, N., Zolnierkiewicz, G., Pilarska, M., Typek, J., Blonska-Tabero, A., & Aidinis, C. (2017). Magnetic Study of Phases in $FeVO_4$-$Co_3V_2O_8$ System. *Acta Physica Polonica A*, 132(1), 24-30.

[200]. Sivaselvan, S. (2024). $FeVO_4$ nanoparticles: Powering synergistic hetero-Fenton photodegradation of methyl violet and enabling green chemical synthesis. Indian Journal of Chemistry (IJC), 63(11), 1112-1120.

[201]. Khabbaz, S. H., Bagheri, A., & Mousavi-Kamazani, M. (2025). Synthesis, characterization, and application of $MnFe_2O_4$/$FeVO_4$/modified zeolite nanocomposite as an effective photocatalyst for methylene blue degradation and benzothiophene desulfurization. *Heliyon*, 11, e41294.

[202]. Patterson, A. L. (1939). The Scherrer formula for X-ray particle size determination. *Physical review*, 56(10), 978

[203]. Kunert, J., Drochner, A., Ott, J., Vogel, H., & Fueß, H. (2004). Synthesis of Mo/V mixed oxide catalysts via crystallisation and spray drying—a novel approach for controlled preparation of acrolein to acrylic acid catalysts. *Applied Catalysis A: General*, 269(1-2), 53-61.

[204]. Ghosh, J., Ali, M. S., & Bhattacharya, S. (2024). Dielectric Relaxation and AC Conductivity of Fe-Doped Glassy Semiconductors: Role of Fe Doping on Relaxation Time. *ECS Journal of Solid State Science and Technology*, 13(3), 033001.

[205]. Carcia, P. F., & McCarron Iii, E. M. (1987). Synthesis and properties of thin film polymorphs of molybdenum trioxide. *Thin Solid Films*, 155(1), 53-63.

[206]. Ghosh, A. (1990). Electrical transport properties of molybdenum tellurite glassy semiconductors. *Philosophical Magazine B*, 61(1), 87-96.

[207]. Das, A. S., Biswas, D., Roy, M., Roy, D., & Bhattacharya, S. (2019). Effect of V_2O_5 concentration on the structural and optical properties and DC electrical conductivity of ternary semiconducting glassy nanocomposites. *Journal of Physics and Chemistry of Solids*, 124, 44-53.